

**COMPUTATIONAL MODELLING STUDIES OF ZrNb-X (X = Co, Sn) ALLOYS**

By

**MAGOJA MARTINUS MALEBATI**

DISSERTATION

Submitted in fulfilment of the requirements for the degree of

**MASTER OF SCIENCE**

In

**PHYSICS**

In the

**FACULTY OF SCIENCE AND AGRICULTURE**

**(School of Physical and Mineral Sciences)**

at the

**UNIVERSITY OF LIMPOPO**

**SUPERVISOR:** Prof. H.R. Chauke

**CO-SUPERVISOR:** Prof. P.E. Ngoepe

**2021**

## ABSTRACT

The *ab initio* density functional theory and molecular dynamics approach have been used to study the properties of Zr-based systems. In particular Zr-Nb, Zr-Nb-X (X = Co and Sn). We have calculated the structural, elastic, mechanical properties and temperature dependence particularly to determine their stabilities. These alloys are important for a wide range of technological applications, primarily in the nuclear and chemical industries due to their good irradiation stability, wear and corrosion resistance, high mechanical strength and superior neutron economy.

The virtual crystal approximation was used to introduce small amounts of either Co or Sn contents on Zr-Nb system. The main idea is to advance high-temperature applications of Zr-Nb system through ternary alloying. Calculations were carried out using the *ab initio* DFT employing the plane-wave pseudopotential method as implemented within the CASTEP code. The influence of partial substitution for Nb concentration with either Co or Sn concentrations was investigated on the Zr-Nb-X systems of various concentrations. The resulting equilibrium lattice parameters, heats of formation, elastic properties, and the density of states were evaluated to mimic their structural, thermodynamic and mechanical stability trends.

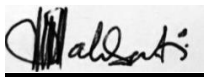
The lattice parameters of binary systems  $Zr_{99}Nb_{1.0}$ ,  $Zr_{98.8}Nb_{1.2}$ ,  $Zr_{98.1}Nb_{1.9}$ ,  $Zr_{97.5}Nb_{2.5}$ ,  $Zr_{97}Nb_3$ ,  $Zr_{78}Nb_{22}$ ,  $Zr_{78}Nb_{22}$  and  $Zr_{50}Nb_{50}$  gave better agreement with available experimental data to within 5 %, while those for ternary systems have shown a decrease with the introduction of the third element i.e. Co or Sn. The heats of formation were negative (stable) at smaller concentrations of  $\leq 1$  at. % Co. Moreover, the correlation of electronic stability using the DOS and the  $\Delta H_f$  calculations has indicated that the systems are thermodynamically stable within  $\leq 1$

at. % Co for ( $Zr_{99}Nb_{1-x}Co_x$ ,  $Zr_{98.8}Nb_{1.2-x}Co_x$ ,  $Zr_{98.1}Nb_{1.9}Co_x$ ,  $Zr_{97.5}Nb_{1.5-x}Co_x$ ,  $Zr_{97}Nb_{3-x}Co_x$  and  $Zr_{78}Nb_{22-x}Co_x$ ) systems. It was found that the increase in Co concentration enhances the thermodynamic, elastic and mechanical stability of the systems and they are found to be stable at small concentrations of about 1 at. % Co.

Furthermore, the temperature dependence was carried out using Dmol<sup>3</sup>. In particular, the canonical ensemble (NVT) calculations were carried out at different temperatures and we observed their structural behaviour with regard to the binding energy and elastic properties at any given temperature up to 2400 K. We compare the temperature dependence of Zr,  $Zr_{50}Nb_{50}$ ,  $Zr_{78}Nb_{22}$ ,  $Zr_{78}Nb_{21}Co_1$ ,  $Zr_{78}Nb_{20}Co_2$ ,  $Zr_{78}Nb_{19}Co_3$ ,  $Zr_{50}Nb_{49}Sn_1$ ,  $Zr_{50}Nb_{48}Sn_2$  and  $Zr_{50}Nb_{47}Sn_3$  systems. In the case of binary system, the  $Zr_{78}Nb_{22}$  was more promising, showing lower binding energy of -6.87eV/atom. It was shown that ternary additions with small atomic percentages of Co and Sn have a significant impact on Zr-Nb alloy. Particularly, their elastic properties showed a possible enhancement on the strength and ductility at high-temperature. This was observed for 1 at. % since it satisfied the requirements for ductility and strength as specified in literature. The Co and Sn addition on the  $Zr_{78}Nb_{22}$  system is more promising for high-temperature applications, with Sn being more preferable.

## DECLARATION

I declare that the dissertation hereby submitted to the University of Limpopo, for the degree of Master of Science has not previously been submitted by me for a degree at this or any other university; that it is my work in design and in execution, and that all material contained herein has been duly acknowledged

A handwritten signature in black ink, appearing to read 'Malebati MM', is written over a light grey rectangular background.

**MALEBATI MM (MR)**

**Date : 16 September 2020**

## **DEDICATION**

I dedicate my dissertation work to my family (the list is endless) and many friends. A special feeling of gratitude to my loving parents, Lazarus and Salome Malebati whose words of encouragement and push for tenacity always ring in my ears.

## **ACKNOWLEDGEMENTS**

Many thanks to Prof P. E. Ngoepe for a wonderful opportunity to do computational modelling studies at the Materials Modelling Centre (MMC), this has convincingly conveyed a spirit of adventure in me about research. I would also like to express the deepest gratitude and appreciation to my supervisor Prof H. R. Chauke who has the attitude and substance of a genius. Without his help, I would have never made it possible in as far as this dissertation work is possible. Also, many thanks to MMC and Centre for High Performance Computing (CHPC) for computational resources, not forgetting the National Research Foundation (NRF) and Titanium Centre of Competence (TiCoC) for funding and MMC members (students and staff members) for their inputs and support throughout. Lastly, University of Limpopo for allowing me to register MSc at their institution.

## Table of Contents

<b>CHAPTER 1</b> .....	1
<b>1. Introduction</b> .....	1
<b>1.1. Background</b> .....	1
<b>1.2. Aim</b> .....	4
<b>1.3. Objectives</b> .....	4
<b>1.4. Rationale</b> .....	5
<b>1.5. Outline of the dissertation</b> .....	7
<b>CHAPTER 2</b> .....	9
<b>2. Literature Review</b> .....	9
<b>2.1. Zirconium alloys</b> .....	9
<b>2.2. Zr-Nb alloys</b> .....	11
<b>2.3. Phase diagram</b> .....	12
<b>2.4. Zr-Co alloy</b> .....	14
<b>2.5. Zr-Nb-X alloys</b> .....	14
<b>CHAPTER 3</b> .....	16
<b>3. Theoretical Techniques</b> .....	16
<b>3.1. Density functional theory</b> .....	16
<b>3.2. Local density approximation</b> .....	22
<b>3.3. Generalized gradient approximation</b> .....	22
<b>3.4. Plane-wave pseudopotential method</b> .....	23
<b>3.5. Energy cutoff and k-point sampling</b> .....	28

3.6. Computational codes .....	30
3.6.1.1. Virtual crystal approximation .....	32
3.6.2. Molecular dynamics .....	33
3.7. Implementation of codes.....	35
3.7.1. CASTEP approach .....	35
3.7.2 DMol3 approach.....	36
3.7.3. Flow chart on computational approach.....	36
<b>CHAPTER 4.....</b>	<b>38</b>
<b>4. Structural properties and heats of formation .....</b>	<b>38</b>
4.1. VCA model.....	38
4.2. Convergence test.....	39
4.3. Geometry optimization .....	42
4.4. Effect of Co addition on binary Zr-Nb systems .....	45
4.4.1. Co addition on $Zr_{99}Nb_{1.0}$ alloy .....	46
4.4.2. Co addition on $Zr_{98.8}Nb_{1.2}$ alloy .....	47
4.4.3. Co addition on $Zr_{98.1}Nb_{1.9}$ alloy .....	49
4.4.4. Co addition on $Zr_{97.5}Nb_{2.5}$ alloy .....	49
4.4.5. Effect of Co addition on $Zr_{97}Nb_3$ alloy .....	50
4.4.6. Effect of Co addition on $Zr_{78}Nb_{22}$ alloy.....	51
4.4.7. Overview of the investigated systems.....	53
<b>CHAPTER 5.....</b>	<b>55</b>



<b>5. Mechanical and Electronic Properties</b> .....	55
<b>5.1. Overview of elastic properties</b> .....	55
<b>5.2. Elastic properties</b> .....	55
<b>5.3. Mechanical stability</b> .....	56
<b>5.3.1. <math>Zr_{99}Nb_{1-x}Co_x</math></b> .....	58
<b>5.3.2. <math>Zr_{98.8}Nb_{1.2-x}Co_x</math></b> .....	59
<b>5.3.3. <math>Zr_{98.1}Nb_{1.9-x}Co_x</math></b> .....	60
<b>5.3.4. <math>Zr_{97.5}Nb_{2.5-x}Co_x</math></b> .....	61
<b>5.3.5. <math>Zr_{97}Nb_{3-x}Co_x</math></b> .....	63
<b>5.3.6. <math>Zr_{78}Nb_{22-x}Co_x</math></b> .....	64
<b>5.3.7. Overview of the elastic properties</b> .....	66
<b>5.4. Overview of the density of states</b> .....	70
<b>5.5. The density of states for Zr-Nb and Zr-Nb-Co alloy</b> .....	70
<b>Chapter 6</b> .....	74
<b>6. Molecular dynamics</b> .....	74
<b>6.1. Binding energy</b> .....	74
<b>6.2. Density of states</b> .....	81
<b>6.3. Elastic properties</b> .....	83
<b>6.4. Bulk over shear modulus (Pugh's ratio)</b> .....	88
<b>6.5. Young's Modulus</b> .....	89
<b>6.6. Poisson's ratio</b> .....	91

<b>Chapter 7</b> .....	94
<b>7.1. Summary and Conclusion</b> .....	94
<b>7.2. RECOMMENDATIONS AND FUTURE WORK</b> .....	97
<b>REFERENCES</b> .....	98

## LIST OF FIGURES

Figure 2.1. The binary phase diagram of the Zr-Nb [34].....	14
Figure 3.1. A schematic representation of the relationship between all-electron and pseudopotentials and wave-functions [87]. The radius at which all-electron and pseudopotentials and wavefunctions match is designated $r_c$ . ....	28
Figure 3.2. Flow chart showing computational approach used in the study. ....	37
Figure 4.1. The (A) $\alpha$ -Zr and (B) $\beta$ -Nb structures. ....	38
Figure 4.2. A schematic representation of a VCA model showing step-wise construction of the (B) binary and (C) ternary systems with the alloying elements (Nb and X) doped on Zr sublattice. ....	39
Figure 4.3. The graph of total energy against cutoff energy for (A) Zr, (B) Nb, (C) Zr-Nb and (D) $Zr_{78}Nb_{22}$ alloys. ....	40
Figure 4.4. Displays the graphs of final energy against the k-points for (A) $\alpha$ -Zr, (B) Nb, (C) $Zr_{50}Nb_{50}$ and (D) $Zr_{78}Nb_{22}$ systems respectively.....	41
Figure 4.5. Heats of formation for the Zr-Nb system at numerous at. % Co addition for (A) $Zr_{99}Nb_{1-x}Co_x$ , (B) $Zr_{98.8}Nb_{1.2-x}Co_x$ , (C) $Zr_{98.1}Nb_{1.9-x}Co_x$ , (D) $Zr_{97.5}Nb_{2.5-x}Co_x$ , (E) $Zr_{97}Nb_{3-x}Co_x$ and (F) $Zr_{78}Nb_{22-x}Co_x$ systems. The figures are used to estimate thermodynamically stable systems graphically by extrapolating linearly with the x-axis and the y-axis.....	54
Figure 5.1. The elastic constants against alloying element content (% Co) in A and B/G against alloying element content (% Co) in B for the $Zr_{99}Nb_{1-x}Co_x$ system.....	59
Figure 5.2. The elastic constants against alloying element content (% Co) in A and B/G against alloying element content (% Co) in B for the $Zr_{98.8}Nb_{1.2-x}Co_x$ system....	60
Figure 5.3. The elastic constants against alloying element content (% Co) in A and B/G against alloying element content (% Co) in B for the $Zr_{98.1}Nb_{1.9-x}Co_x$ system....	61

Figure 5.4. The elastic constants against alloying element content (% Co) in A and B/G against alloying element content (% Co) in B for $Zr_{97.5}Nb_{2.5-x}Co_x$ system.....	62
Figure 5.5. The elastic constants against alloying element content (% Co) in A and B/G against alloying element content (% Co) in B for the $Zr_{97.5}Nb_{2.5-x}Co_x$ system....	64
Figure 5.6. The elastic constants against alloying element content (% Co) in A and B/G against alloying element content (% Co) in B for the $Zr_{78}Nb_{22-x}Co_x$ system. ....	65
Figure 5.7. Elastic constants versus atomic percentage cobalt in the A) $Zr_{99}Nb_{1-x}Co_x$ , (B) $Zr_{98.8}Nb_{1.2-x}Co_x$ , (C) $Zr_{98.1}Nb_{1.9-x}Co_x$ , (D) $Zr_{97.5}Nb_{2.5-x}Co_x$ , (E) $Zr_{97}Nb_{3-x}Co_x$ and (F) $Zr_{78}Nb_{22-x}Co_x$ systems at various concentrations. ....	68
Figure 5.8. Ration of bulk and shear modulus against percentage cobalt in the competing phases of A) $Zr_{99}Nb_{1-x}Co_x$ , (B) $Zr_{98.8}Nb_{1.2-x}Co_x$ , (C) $Zr_{98.1}Nb_{1.9-x}Co_x$ , (D) $Zr_{97.5}Nb_{2.5-x}Co_x$ , (E) $Zr_{97}Nb_{3-x}Co_x$ and (F) $Zr_{78}Nb_{22-x}Co_x$ systems. The dotted line indicates the $B/G = 1.75$ reference as a visual guide. A B/G ratio greater or less than 1.75 is indicative of ductility or brittleness respectively.....	69
Figure 5.9. Comparison of the total density of states (tDOS) for the (A) $Zr_{99}Nb_{1-x}Co_x$ , (B) $Zr_{98.8}Nb_{1.2-x}Co_x$ , (C) $Zr_{98.1}Nb_{1.9-x}Co_x$ , (D) $Zr_{97.5}Nb_{2.5-x}Co_x$ , (E) $Zr_{97}Nb_{3-x}Co_x$ and (F) $Zr_{78}Nb_{22-x}Co_x$ systems. The fermi energy is taken as the energy zero ( $E-E_f = 0$ ).....	73
Figure 6.1. Binding energy against the composition of $Zr_{78}Nb_{22-x}X_x$ and $Zr_{50}Nb_{50-x}X_x$ ( $x = Co, Sn$ ) at 0K.....	77
Figure 6.2. Binding energy against temperature for $\alpha$ -Zr, $Zr_{78}Nb_{22}$ , $Zr_{50}Nb_{50}$ systems and ternary solid solutions of $Zr_{78}Nb_{22-x}Sn_x$ , $Zr_{50}Nb_{50-x}Sn_x$ , $Zr_{78}Nb_{22-x}Co_x$ and $Zr_{50}Nb_{50-x}Co_x$ alloy systems.....	79
Figure 6.3. Comparison of the DOS for the $Zr_{78}Nb_{22-x}X_x$ and $Zr_{50}Nb_{50-x}X_x$ systems. The Fermi energy is taken as the energy zero ( $E-E_f = 0$ ).....	82

Figure 6.4. Elastic constants for (A)  $\alpha$ -Zr, (B)  $Zr_{50}Nb_{50}$ , (C)  $Zr_{50}Nb_{49}Sn_1$ , (D)  $Zr_{50}Nb_{48}Sn_2$ , (E)  $Zr_{50}Nb_{47}Sn_3$ , (F)  $Zr_{50}Nb_{49}Co_1$ , (G)  $Zr_{50}Nb_{48}Co_2$  and (H)  $Zr_{50}Nb_{47}Co_3$  systems versus temperature to investigate their mechanical stability. .... 84

Figure 6.5. Elastic constants of (A)  $\alpha$ -Zr, (B)  $Zr_{78}Nb_{22}$ , (C)  $Zr_{78}Nb_{21}Sn_1$ , (D)  $Zr_{78}Nb_{20}Sn_2$ , (E)  $Zr_{78}Nb_{19}Sn_3$ , (F)  $Zr_{78}Nb_{21}Co_1$ , (G)  $Zr_{78}Nb_{20}Co_2$  and (H)  $Zr_{78}Nb_{19}Co_3$  systems versus temperature to investigate their mechanical stability at increasing temperature..... 87

Figure 6.6. The B/G ratio against temperature for Zr-Nb-X systems in the left column (A, C)  $Zr_{50}Nb_{50-x}Co_x$  and  $Zr_{78}Nb_{22-x}Co_x$  while right column (B, D)  $Zr_{50}Nb_{50-x}Sn_x$  and  $Zr_{78}Nb_{22-x}Sn_x$ . The dotted line represents  $B/G = 1.75$ ..... 88

Figure 6.7. Displaying Young's modulus versus temperature for  $Zr_{50}Nb_{50-x}Co_x$  and  $Zr_{78}Nb_{22-x}Co_x$  systems (A, C) while (B, D) displays for  $Zr_{50}Nb_{50-x}Sn_x$  and  $Zr_{78}Nb_{22-x}Sn_x$  systems respectively. .... 91

Figure 6.8. Indicative Poisson's ratio against temperature for  $Zr_{50}Nb_{50-x}Co_x$  and  $Zr_{78}Nb_{22-x}Co_x$  systems (A, C) while (B, D) displays for  $Zr_{50}Nb_{50-x}Sn_x$  and  $Zr_{78}Nb_{22-x}Sn_x$  systems respectively. .... 93

## LIST OF TABLES

Table 4.1. Show the equilibrium lattice parameters and volume for $\alpha$ -Zr, Nb, $Zr_{50}Nb_{50}$ and $Zr_{78}Nb_{22}$ structures.....	43
Table 4.2. Tabulated results showing the lattice parameters, volume and heat of formation for $Zr_{99}Nb_{1.0}$ , $Zr_{98.8}Nb_{1.2}$ , $Zr_{98.1}Nb_{1.9}$ , $Zr_{97.5}Nb_{2.5}$ , $Zr_{97}Nb_3$ , $Zr_{78}Nb_{22}$ , $Zr_{78}Nb_{22}$ and $Zr_{50}Nb_{50}$ systems. ....	45
Table 4.3. Structure, lattice constants and heats of formation for $Zr_{99}Nb_{1.0}$ system..	47
Table 4.4. Structural parameter and heats of formation for $Zr_{98.8}Nb_{1.2-x}Co_x$ system (effect of Co addition).....	48
Table 4.5. Structure, lattice parameter and heats of formation for $Zr_{98.1}Nb_{1.9-x}Co_x$ system (effect of Co addition).....	49
Table 4.6. Structural parameter and heats of formation for $Zr_{97.5}Nb_{2.0-x}Co_x$ systems (effect of ternary Co addition).....	50
Table 4.7. Structure, lattice parameter and heats of formation for $Zr_{97}Nb_{2.5-x}Co_x$ systems (the effect of Co addition).....	51
Table 4.8. Structure, lattice parameter and heats of formation for $Zr_{78}Nb_{22-x}Co_x$ (effect of Co addition).....	52
Table 5.1. Lattice parameters and the elastic constants for the $Zr_{99}Nb_{1.0-x}Co_x$ system. ....	59
Table 5.2. Lattice parameters and the elastic constants for the $Zr_{98.8}Nb_{1.2-x}Co_x$ system.....	60
Table 5.3. Lattice parameters and the elastic constants for the $Zr_{98.1}Nb_{1.9-x}Co_x$ system.....	61
Table 5.4. Lattice parameters and the elastic constants for $Zr_{97.5}Nb_{2.5-x}Co_x$ system. ....	63

Table 5.5. Lattice parameters and the elastic constants for the $Zr_{97}Nb_{3-x}Co_x$ system. .....	64
Table 5.6. Lattice parameters and elastic constants for the $Zr_{78}Nb_{22-x}Co_x$ system (effect of Co addition). .....	65
Table 6.1 Showing the binding energy [Eb] of Co and Sn addition at 0K for $Zr_{78}Nb_{22-x}X_x$ and $Zr_{50}Nb_{50-x}X_x$ systems. The result of the binary system is also shown for reference. ....	76

# CHAPTER 1

## 1. Introduction

In this chapter, we give a summary of theoretical and experimental findings regarding the Zr, Nb, binary Zr-Nb and Zr-Nb-X ternary alloys, where X represents some transition metals of interest. A brief background information on the properties of these systems is also highlighted to give insight towards the structural predictions and the analysis of the stability of both binary and ternary systems. In the last section of this chapter, the objectives and motivations of the current study are given. Finally, the outline of the dissertation is also specified.

### 1.1. Background

Zirconium is a commercially available refractory metal with excellent corrosion resistance, good mechanical properties and very low thermal neutron cross-section [1]. It has attracted a lot of attention recently due to its distinctive properties that make it suitable for extensive applications in nuclear power, chemical industries [2] and power engineering [3]. Zr is extensively used in various types of fission reactors both light and heavy water types for different applications. More importantly, Zr is used as a principal cladding material due to its good irradiation stability, high mechanical strength, superior neutron economy and corrosion resistance [4].

The presence of hydrogen, oxygen and nitrogen in high concentrations against Zr during nuclear operation produces a variety of undesirable chemical and mechanical consequences [5]. Alloying Zr with a variety of other elements such as Sn, Fe, Cr, Ni, O and Nb counteract those undesired effects. These alloying elements were found to



improve resistance to creep, yield strength, corrosion, oxidation, and reduces the irradiation growth [6, 7].

Zirconium and Zr alloys are used for the main mechanical components of the nuclear fuel assemblies such as control rods, fuel rods and in-core instrumentation [8]. However, Zr suffers failure in working conditions being that the oxidation rate of the cladding and its hydrogen pick-up is high [9]. Alloys with a high percentage of Nb ( $x > 5$ ) have a high capacity for hydrogenation which mainly causes poor corrosion resistance. As a consequence, alloys with a small amount of Nb ( $x < 5$ ) are preferred for optimising their application in reactor metallurgy [10].

More advanced Zr-based alloys are being developed to sustain severe operating conditions such as the higher burn-up, increased operation temperature and high pH. This is due to the increasing demand for a meaningful source of energy and the increasing world population. It was found that its mixture with niobium ( $Zr_{100-x}Nb_x$ ) has good physical and thermodynamic applications, that is, it exhibits superelasticity, superconductivity properties and forms dielectric oxide layers [11]. Hence, most of these Zr alloys contain Nb as the major alloying element, which is recommended for developing new fuel cladding materials since it is an effective strengthening element [12].

The tendency to select Nb as the major alloying element in most Zr-based alloys is a common characteristic of the newly developed fuel cladding material. Theoretical findings on Zr-Nb alloys also revealed that the microstructural and corrosion test with a variety of cooling rates and Nb content in the alpha matrix plays an important role to enhance the corrosion resistance than the supersaturated Nb, the beta phase and

the precipitates [4]. Moreover, they showed good corrosion resistance when subjected to the annealing temperature [13].

Some of the Zr alloys that are mainly used in the nuclear industry include zirconium-tin (Zr-Sn) and zirconium-niobium (Zr-Nb) alloys of different competing compositions and they are susceptible to both hydrogen degradation and oxidation. Zr alloys with or without Sn, tend to exhibit irradiation growth that is significantly reduced compared with unalloyed Zr. The microstructures of Zr-Nb and Zr-Sn are found to be different but Nb is found to be effective in modifying the point defect properties. When Sn is in solution in the absence of Nb there is a propensity for high rates of accelerated growth which is associated with c-component loop formation [7].

Apart from binary Zr alloys, theoretical and experimental attempts have been performed to better the performance of nuclear reactors using ternary systems such as the Zr-Nb-Fe [14] and Zr-Nb-Sn (O) [15]. The addition of elements such as Fe, Cr and Ni is regarded as impurity alloying but the recent studies indicated that the absence of Nb in alpha-phase solid solution is highly responsible for the high rates of irradiation growth [7]. Some recently developed alloys such as Westinghouse's Zirlo™, sometimes include both Nb and Sn and some Fe with the minor quantities of other transition metals such as Cr and Ni [16, 17]. It has been suggested that alloying Zr with Co and Nb could improve the high-temperature applications and the resistance to creep, wear and corrosion [14].

According to previous studies, it has been reported that much progress has been made in the determination of phase stability of various systems using *ab initio* approach [18]. The study by Cottura et.al used the first-principles calculations relying on the density functional theory to investigate the thermodynamic properties of the

Zr-Nb system considering both hcp Zr-rich and bcc Nb-rich solid solutions. These were found to be simple unmixing systems and their solubility limits were comparable with other experimental findings [19].

Simulations on liquid structures of undercooled  $Zr_{90}Nb_{10}$ ,  $Zr_{70}Nb_{30}$  and  $Zr_{50}Nb_{50}$  alloys have also been studied using electrostatic levitation experiments. However, this technique was limited to describe the structure at high temperatures. Thus molecular dynamics simulation played a role in complementing the experimental data since it is capable to simulate high temperature properties [20]. The structure of liquid alloy was reported to have a significant influence on the thermodynamic properties. Furthermore, it was also reported that Zr-Nb-Sn and Zr-Fe-Cr showed potential for high-temperature corrosion applications [21].

## **1.2. Aim**

This work aims to investigate the structural, electronic and mechanical stabilities of Zr-Nb-X alloys using density functional theory and molecular dynamics approaches.

## **1.3. Objectives**

The objectives of the study are to:

- i. determine the structural, equilibrium lattice parameter and heats of formation of Zr-Nb and Zr-Nb-X systems
- ii. determine the thermodynamic and elastic stability of Zr-Nb and Zr-Nb-X systems
- iii. investigate the mechanical stability with regard to elastic properties and Pugh's ratio (B/G) at 0K and high temperature

- iv. investigate the partial substitution with Co and Sn on the Zr-Nb alloy at 0K
- v. determine the effect of Sn and Co addition in Zr-Nb alloy at varying temperatures.
- vi. determine the binding energy, the density of states, elastic properties, B/G ratio, Young's modulus and Poisson's ratio.

#### **1.4. Rationale**

Nuclear-based research has been devoted to Zr and its alloys to develop new systems with better properties such as creep and corrosion resistance [22]. A variety of different alloying elements (Fe, Sn, O, Ni, Nb and Cr) were found to improve the resistance to creep, corrosion and yield strength of Zr alloys [6]. The Zr-based alloys with improved properties are of importance in conditions such as higher burn-up, higher temperature and high pH applications.

The development of Zr-based alloys for future cladding of nuclear fuel rods and other nuclear assembly components has been previously reported [23]. Zircaloy-1 was the first Zr-based alloy to be developed and it contained 2.5 at. % Sn which is used to improve the yield strength and creep resistance of the metal [24]. It was then discovered that zircaloy-1 had unsatisfactory resistance to corrosion, which prompted the search for new alloy composition. An ingot of test alloy was found to exhibit remarkable corrosion properties and this test alloy had been accidentally contaminated with stainless steel, thereby containing small amounts of Fe, Cr and Ni [7]. This was followed by Zircaloy-2 and Zircaloy-4 with zircaloy-2 having small compositional variations whereas Zircaloy-4 most of the Ni is replaced with Fe to reduce the hydrogen pick-up fraction [25, 26]. In the quest for the development of Zircaloys, Zr containing Nb alloys were developed and used in other reactor designs

such as Canada Deuterium Uranium (CANDU), water-water energetic reactor (VVER) and Reaktor Bolshoy Moshchnosti Kanalniy (RMBK) [27].

According to literature Co has been suggested as an alloying element due to its limited use, it has also been used as the dominant structure in cobalt-based alloys and also used in alloys containing lesser amounts of Co for applications in thermal reactors [28]. The development of new Zr alloys with better mechanical properties, high corrosion resistance is necessary for optimal operation of the nuclear reactor at higher temperatures and the economic efficiency or gain. The element Sn improves the yield strength and the creep resistance of Zr metal [24].

The nuclear reactor suffers failure due to poor corrosion, cladding and high temperature resistance occurring on the in-core instrumentations, thus its performance will deteriorate depending on the material used. The current study will use ab initio methods based on electronic density functional theory (DFT) [29, 30] to investigate physical properties such as structural, electronic, elastic properties as well as energetic stabilities of Zr-Nb (Co, Sn) alloys. The choice of Co was based on its good physical properties though of limited use [28]. Furthermore, Co-based superalloys have been widely used due to their excellent mechanical properties such as corrosion resistance and thermal fatigue resistance at elevated temperatures (above 830 K). Sn has been reported to improve the yield strength [24] as cladding materials in a nuclear reactor. More importantly, these alloying elements have significant potentials to enhance the mechanical properties and corrosion resistance of the Zr-based system. This is critical for nuclear power generating technology, particularly as a cladding of fuel rods in nuclear reactors. Thus, structural and mechanical properties of the Zr-based alloys will be evaluated to check the impact of Co and Sn; and how can they enhance the strength of the material.

That is, we will predict the relative stability of competing phases at 0 K and at increased temperature. The study will employ the virtual crystal approximation (VCA) to vary the concentration of Co and Sn in the Zr-Nb-(X) alloy. The VCA approach [31] has the advantage of allowing small concentrations of additive elements on a single unit cell. Furthermore, the temperature dependence of the systems was performed using Dmol<sup>3</sup> code [32]. We will show that the addition of Nb at 22 at. % and 50 at. % has significance and gives better predictions with Zr. The addition of the third element Co or Sn enhances the Zr-Nb system at different concentrations.

### **1.5. Outline of the dissertation**

In chapter 1, we give a summary of theoretical and experimental findings regarding the Zr and Zr alloys; binary Zr-Nb as well as the ternary alloys of Zr-Nb-X (X either Co or Sn). The advantages of various alloying elements in nuclear and industrial applications are briefly discussed. The importance of zirconium alloys, their mechanical and thermodynamic properties were also noted. The motivation and objectives of the study are discussed. Lastly, the outline of the study is given.

In Chapter 2 we provide a detailed literature review on binary Zr-Nb and ternary alloys, and other related Zr-based systems.

In chapter 3 we discuss the theoretical techniques and methodology used to perform the calculations of the Zr, binary Zr-Nb and ternary Zr-Nb-Co and Zr-Nb-Sn systems. The density functional theory, local density approximation, generalized crystal approximation, virtual crystal approximation, projector augmented wave and plane-wave pseudopotential methods are summarised.

In Chapter 4 we present the DFT results achieved in this study. This includes the convergence of cutoff energy and k-points, geometry optimization, heats of formation

for all Zr, binary Zr-Nb and ternaries of Zr-Nb-Co and Zr-Nb-Sn systems. The equilibrium lattice constants are also discussed.

In Chapter 5 we discuss the mechanical properties and electronic properties of the different atomic cobalt and tin additions in the Zr-Nb-Co and Zr-Nb-Sn systems. Furthermore, we discuss the temperature dependence of these systems concerning their elastic constants, electronic DOS, binding energies and elastic constants.

In Chapter 6 we discuss the molecular dynamics results for both the binary and ternary systems. In particular the effect of either Co or Sn on ZrNb structure. Moreover, the discussion is based on the temperature dependence on analysis of binding energy, the density of states, elastic properties, B/G ratio, Young's modulus and Poisson's ratio.

Lastly, in Chapter 7 we give the summary and conclusion from the results obtained. Followed by an appendix.

## CHAPTER 2

### 2. Literature Review

#### 2.1. Zirconium alloys

Zirconium alloys are known to be of very special practical importance because they were regarded as promising materials for atomistic industry and nuclear engineering [10]. Zr alloys are structural materials with a wide range of technological applications, particularly in the nuclear and chemical industries [19]. The alloys were chosen for these primarily because they have a much lower neutron absorption per unit of strength than other commercially available structural materials such as Ni, Fe, Ti, Al, Mg and Be. Additionally, many Zr alloy systems have been studied for potential usage in nuclear systems, only a few of them are of commercial importance [1].

A nuclear reactor can be defined as a system that contains and controls sustained nuclear chain reactions. Any nuclear system, such as a nuclear reactor containing nuclear materials must be well analysed to determine their criticality to validate the proper safety conditions to avoid critical excursions [33]. Six types of nuclear reactors are designed to produce commercial electricity around the world namely basic gas-cooled reactor (Magnox), advanced gas-cooled reactor (AGR), pressurised water reactor (PWR), boiling water reactor (BWR), CANDU and RBMK.

The earliest reactor types are the Magnox and AGR, the Magnox reactor is a natural uranium metal (0.7% U235) magnesium alloy cladding, whereas the AGR is uranium dioxide enriched to 2.3% U235 stainless steel cladding CANDU is the pressurised heavy water reactor which is unenriched uranium dioxide (0.7% U235) zirconium alloy cladding and the PWR (pressurized water reactor) uses enriched (about 3.2%



U235) uranium dioxide as a fuel in zirconium alloy cans. The remaining two are the RBMK (boiling light water, graphite-moderated nuclear reactor) and BWR (boiling water reactor). BWR is uranium dioxide enriched to 2.4% U235 zirconium alloy cladding whereas RBMK is uranium dioxide enriched to 1.8% U235 zirconium alloy cladding [34].

To improve the resistance to creep, corrosion and yield strength a variety of different alloying elements has been explored like Sn, Sc, Sb, Fe and Cr. [35, 36]. There are many compositions of zirconium alloys that were used in nuclear technology. For example, Zircalloys are Zr alloys containing Sn, Fe, and Cr as alloying elements. The largest hydrogen uptake occurs in Zr-1.5%Sn-0.5%Fe, this composition is very similar to that of zircaloy this happens because or due to the lack of niobium [37].

The effect of alloying elements is extremely important, this refers to the stabilizers such as tin in zircaloy-4 which showed the highest strengthening effect with hydrogen because there is an interaction between dissolved tin and hydrogen [24]. Cold-work-stress-relieved (CWSR) zircaloy-4 (Zr-1.5%Sn-0.2%Fe-0.1%Cr) is used as a fuel cladding in Pressurized Water Reactors (PWR) and recrystallized zircaloy-2 (Zr-1.5%Sn-0.15%Fe-0.1%Cr-0.05%Ni) is used in boiling water reactors (BWR) [22]. In PHWR Zr-2.5%Nb is used as the pressure tube material for CANDU reactors [38]. Recent studies show that modern alloys such as Zircaloy-2 and M5 (Zr-1Nb-O) contain Nb, although this addition has been used in Russian and Canadian alloys [36]. Zirlo (Zr-1.0Nb-1.0Sn-0.1Fe) [39] is Nb modified zircaloy.

## 2.2. Zr-Nb alloys

Zr-Nb alloys are being developed to improve the economy of nuclear reactor plants. Most of the developing alloys are found to have higher Nb and lower Sn contents (in Zr-Sn alloys) to improve corrosion resistance [24]. The mixture of zirconium with niobium has shown to have desirable physical and thermodynamic applications [39]. Recently, the Nb-based binary solutions have been of much technological and academic interest as the alloys of this kind have good mechanical properties [40].

Since commercial alloys are based on the binary Zr-Nb system. The morphology of the  $\alpha$ -Zr and  $\beta$ -Zr ( $\beta$ -Nb) phases determines the Zr-Nb alloy 's behaviour upon thermomechanical treatment and the subsequent change in their properties (corrosion and hydride embrittlement) [41]. Moreover, the Zr-Nb alloy has desirable physical and thermodynamic applications, i.e. it exhibits superelasticity, superconductivity properties and forms dielectric oxide layers [42]. The recent developments of Zr-Nb alloys are recommended for nuclear fuel cladding material. The alloy also plays an important role in energy production by being the main material for the cladding of nuclear fuel in nuclear power plants [43].

It is shown experimentally that Zr-Nb alloys allow for a clear identification of the microstructure which corresponds at low temperature (below  $\approx 890$  K) to an  $\alpha$ -Zr matrix, with a hexagonal close-packed crystallographic structure, containing native  $\beta$ -niobium precipitates with a body-centered cubic structure, this is the case because of the low mobility of Nb in the  $\alpha$ -Zr matrix which means the alloy is not usually in its equilibrium state and the matrix is supersaturated in Nb [44, 45].

It was also noted that the Zr-Nb alloy cladding tubes have been used mostly for pressurized water reactors. The working environment is the combination of

temperature and reactive conditions such as irradiation, oxidation and hydrogen pick-up (i.e. during reactor operation). The absorption of hydrogen by zirconium parts of the core of reactors in operation is stimulated by the composition of the alloy, quality and method of the surface treatment of the parts. It has been reported that, if 5-20% of hydrogen diffuses into the zirconium alloy cladding, zirconium hydrides are being formed. When the concentration of hydrogen exceeds the solubility limit, it stands out as a fragile zirconium hydride, the zirconium alloy will become unreactive (inert) and the corrosion properties will be lost, consequently, hydrogen (hydrides) reduces ductility [24].

The role of Nb has been studied widely on the hydrogen embrittlement of advanced fuel cladding materials. The addition of Nb enhanced the resistance to hydride embrittlement, this can be experienced as the combined effects of Nb precipitates with higher hydrogen solubility and the solute Nb causing the retardation of recrystallization [24]. The effect of alloying elements is very important, there should be a better understanding of them and their studies. As an alloying element to Zr, Nb is employed because it serves as an effective strengthening element for Zr with low cytotoxicity and low magnetic susceptibility ( $2.2 \times 10 \text{ cm}^3 \text{ g}^{-1}$ ) which depends mostly on the composition and phase constitution [46], as such expert study and knowledge of phase diagram (physical properties) and thermodynamic properties is of major importance in many applications [47]

### **2.3. Phase diagram**

The binary Zr-Nb phase diagram [48] is shown in Figure 2.1. This provides knowledge of phases and compositions occurring at different temperatures. More importantly, it is to identify the associated phase, thermodynamic properties and

phase transformations that may occur [49]. This also gives an indication of possible compositions that can exist which may play an important role in the development of alloys for nuclear applications [36]. More importantly, the information on the phase diagrams also plays a crucial role in guiding the design of new material from component materials by taking compositions and temperatures into consideration.

There are three equilibrium phases observed namely, liquid,  $\alpha$ -phase (hcp) and  $\beta$ -phase (bcc) space group  $P6_3/mmc$  (Figure 2.1). It can be seen that the Zr solid phase begins to precipitate when the temperature of the system drops to 2023 K. The solid-liquid coexistence zone coincide as the temperature of the system decreases, and  $\beta$ (Zr, Nb) solid solution is formed at 1993 K. Note also that the  $\alpha$ -phase begins to precipitate when temperature further decreases to 923 K. The eutectoid (Equation 2.1) reaction occurs when the temperature is reduced to 893 K. Finally the  $\alpha$ -Zr and  $\beta$ -Nb phases are generated when the temperature is cooled to room temperature [50].

It can be seen that in the  $\beta$ -phase region, Zr and Nb can co-exist as solid solution. Zhao et. al. has constructed the Zr-Nb solid solutions models in the concentration range from 0 to 100 at. % using first principles DFT. Two different solid solution models, that is the ordered solid solution and disordered solid solution models were suggested [51]. This has given guidance to the current study to construct the binary compositions  $Zr_{78}Nb_{22}$  and  $Zr_{50}Nb_{50}$  for high temperature investigations.



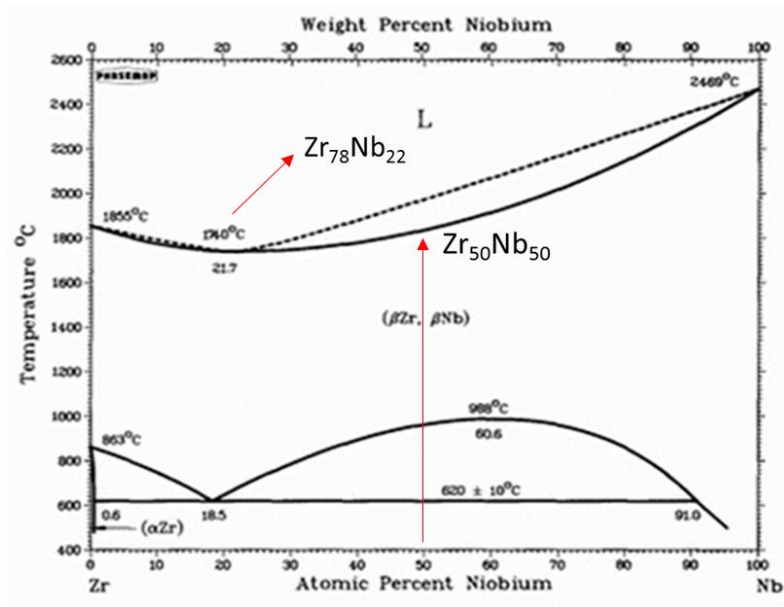


Figure 2.1. The binary phase diagram of the Zr-Nb [34].

## 2.4. Zr-Co alloy

It has been previously reported that the intermetallic compounds that absorb large quantities of hydrogen gas are of technological interest, provided the hydrogen is absorbed rapidly. Zr-Co with a ratio of 1:1 is reported to absorb the largest amount of hydrogen [52]. Zr-Co is mostly suitable for storage, recovery and separation of hydrogen isotopes [53]. A study by Kuentzler et.al, based on a Zr-Co system indicated that a Zr-rich concentration range of compounds is mostly superconductors and a Co-rich concentration range of compounds are magnetic [54]. There is currently no evidence on theoretical and experimental Zr-Nb-Co alloys.

## 2.5. Zr-Nb-X alloys

Many researchers have studied the effect of alloying elements on the structural properties of Zr alloys. For example, Gong et. al. have studied the effect of Yttrium on Zr-Nb alloys at 637 K and 10.3 MPa in pure steam [55]. The addition of Y in their

work was mainly to provide new insight into the effect of alloying elements on the corrosion behaviour of Zr alloys. Lian-Feng et al. have also studied the low cycle fatigue properties of hydrogenated welding sheets of Zr-Nb-Sn alloy. They studied the relationships between nominal stress and strain to investigate fatigue resistance [56]. It was reported that the presence of hydrides reduces fatigue resistance at room temperature. Toffolon-Masclat et al. have improved databases for binary systems such as Zr-Fe, Zr-Sn and Zr-Nb, as well as the ternary Zr-Fe-Cr, Zr-Fe-Ni and Zr-Nb-Fe systems [57].

The Zr-based alloys with Co addition find applications in the refractory high entropy alloys (HEAs). The structural stability and mechanical properties at both room and elevated temperatures have been investigated by Han et al. It was found that the phase stability at high temperature is strongly correlated to the superior mechanical properties at elevated temperature. Moreover, it was discovered that the  $\text{Nb}_{20}\text{Ni}_{20}\text{Ti}_{20}\text{Co}_{20}\text{Zr}_{20}$  HEA possesses excellent structural stability, and exhibits high yield strength from 293 K to 1073 K and large strain above 973 K, which makes it promising for application at high temperature [58].

In the current study, we investigate the effects of Co and Sn on the structural and mechanical properties of Zr-Nb alloy. Unfortunately, there is limited work that has been reported from both theoretical and experimental studies.

## CHAPTER 3

### 3. Theoretical Techniques

In this chapter, we summarize the various methodology that was used to study the properties of Zr-Nb-X systems. The study employed both density functional theory (DFT) and molecular dynamics (MD), which use the different platforms of commercial and academic software such as the plane-wave pseudopotential method Cambridge serial total energy package (CASTEP), forcefield-based method and DMol<sup>3</sup>. The plane-wave pseudopotential method is necessary since it performs the full geometry optimization, particularly the internal parameter relaxation. Physical properties of materials such as total energies, electronic structure, and geometry can be calculated using CASTEP [59] whereas, MD can be performed under various conditions such as constant temperature, energy, volume, and pressure using DMol<sup>3</sup> [60]. In the next section, we describe the quantum mechanical DFT method.

#### 3.1. Density functional theory

Density functional theory (DFT) [61] is a quantum mechanical method used for predicting the ground state energy of many-body (condensed matter) systems. Unlike the Hartree-Fock method [62], DFT calculation adds a step to each major phase of a Hartree-Fock calculation. This step is a numerical integration of the functional (or various derivatives of the functional). Thus in addition to the sources of numerical error in Hartree-Fock calculations (integral accuracy, SCF convergence, and CPHF convergence), the accuracy of DFT calculations also depends on several points used in the numerical integration [63]. Density functional theory was formulated by Hohenberg and Kohn [64] and Kohn and Sham [65] in the 1960s to provide the foundation for accurate calculations. Kohn Sham spin density functional

theory is now the most widely used method for electronic structure calculations in condensed matter physics and quantum chemistry. It provides some useful predictions for atoms, molecules, nanostructures, solids and solid surfaces [66]

In DFT, the total energy of a many-body system is described by the total electron density which is decomposed into one-electron density,

$$E = E[\rho(r)], \tag{3.1}$$

which are constructed from one-electron wavefunction where  $E$  is the total energy and  $\rho$  is the density.

The electron density is used as the fundamental tool for a quantum mechanical theory of matter which originated in the 1920s, by Thomas [67] and Fermi [68]. However, in the previous decades, it was rather the Hartree-Fock approach [69, 70], which was developed and applied to small molecular systems. Calculations on realistic solid-state systems were then out of reach. In 1951, Slater [71], used ideas from the electron gas to simplify the Hartree-Fock theory to a point where electronic structure calculations on solids became achievable. Slater's work, which led to the so-called  $X_\alpha$  method [72] has contributed greatly to the development of electronic structure calculations. In solid-state systems, molecules and atoms, the electron density is a scalar function defined at each point  $r$  in real space:

$$\rho = \rho(r). \tag{3.2}$$

The electron density and the total energy depend on the type and arrangements of the atomic nuclei. Therefore, one can write

$$E = E[\rho(r), \{R_\alpha\}]. \tag{3.3}$$



where the set  $\{R\alpha\}$  denotes the positions of all atoms  $\alpha$ . Equation (3.3) is used for understanding the atomic-scale of electronic, structural and dynamic properties of matter. The evaluation of an expression (3.3), will predict the equilibrium structure of solid, the reconstruction of surfaces and the equilibrium geometry of molecules adsorbed on surfaces. Furthermore, the derivative of the total energy (3.3) concerning the nuclear position of an atom gives the force acting on that atom. This enables the efficient search for stable structures and the study of dynamical processes such as diffusion or the reaction of molecules on surfaces.

In density functional theory, the total energy (3.1) is decomposed into three contributions, kinetic energy and Coulomb energy due to classical electrostatic interactions among all charged particles in the system and a term called the exchange-correlation energy that captures all many-body interactions,

$$E = T_0 + U + E_{xc}. \quad 3.4$$

The term  $U$  is the Coulomb energy. It is purely classical and contains the electrostatic energy arising from the Coulomb attraction between electrons and nuclei  $U_{en}$ , the repulsion between all electronic charges  $U_{ee}$  and the repulsion between nuclei  $U_{nn}$ , written as:

$$U = U_{en} + U_{ee} + U_{nn}, \quad 3.5$$

with

$$U_{en} = -e^2 \sum_{\alpha} z_{\alpha} \int \frac{\rho(r)}{|r-r_{\alpha}|} dr, \quad 3.6$$

$$U_{ee} = e^2 \iint \frac{\rho(r)-\rho(r)'}{|r-r'|} dr dr', \quad 3.7$$

and

$$U_{nn} = e^2 \sum_{\alpha\alpha'} \frac{Z_\alpha Z_{\alpha'}}{|R_\alpha - R_{\alpha'}|} \quad 3.8$$

where  $e$  is the elementary charge of a proton and  $Z_\alpha$  is the atomic number of atom  $\alpha$ . The summations extend over all atoms and the integration 's overall space. Once the electron density and the atomic numbers and positions of all atoms are known, expressions (3.6) to (3.8) can be evaluated by using the techniques of classical electrostatics.

The kinetic energy term,  $T_0$ , is more subtle. In density functional theory, the "real" electrons of a system are replaced by "effective" electrons with the same charge, mass and density distribution. However, effective electrons move as independent particles in an effective potential, whereas the motion of a "real" electron is correlated with those of all other electrons.  $T_0$  is the sum of the kinetic energies of all effective electrons moving as independent particles. Often, one does not explicitly make this distinction between real and effective electrons.

If each effective electron is described by a single-particle wave function,  $\psi_i$  then the kinetic energy of all effective electrons in the system is given by

$$T_0 = \sum n_i \int \Psi_i^*(r) \left[ \frac{-\hbar^2}{2m} \nabla^2 \right] \Psi_i(r) dr \quad 3.9$$

Expression (3.9) is the sum of the expectation values of one-particle kinetic energies;  $n_i$  denotes the number of electrons in state  $i$ . By construction, dynamical correlations between the electrons are excluded from  $T_0$ .

The third term of equation (3.4), called exchange-correlation energy,  $E_{xc}$ , includes all the remaining complicated electronic contributions to the total energy. The Hohenberg-Kohn-Sham theorem, which is a central part of DFT, states that the total

energy is at its minimum value for the ground-state density and that the total energy is stationary concerning first-order variations in the density, *i.e.*

$$\left. \frac{\partial E[\rho]}{\partial \rho} \right|_{\rho=\rho_0} = 0. \quad 3.10$$

In conjunction with the kinetic energy, we have introduced one-particle wavefunctions  $\psi_i(r)$ , which generate the electron density

$$\rho(r) = \sum_i n_i |\psi_i(r)|^2, \quad 3.11$$

where  $n_i$  denotes the occupation number of the eigenstate  $i$ , which is represented by the one-particle wave function  $\psi_i$ . By construction,  $\rho(r)$  in Eq. (3.11) we obtain the exact many-electron density.

The goal of the next step is the derivation of equations that can be used for practical density functional calculations. The variational condition (3.10) can be used to derive the conditions for the one-particle wavefunctions that lead to the ground state density.

Now, by substituting equation (3.11) in expression (3.10) and varies the total energy concerning each wave function, we obtain:

$$\left[ -\frac{\hbar^2}{2m} \nabla^2 + V_{eff}(r) \right] \psi_i(r) = \varepsilon_i \psi_i(r), \quad 3.12$$

with

$$V_{eff}(r) = V_c(r) + \mu_{xc}[\rho(r)]. \quad 3.13$$

Equation (3.12) and (3.13) are called the Kohn-Sham equations. The electron density ( $\rho$ ), which corresponds to these wavefunctions, is the ground state density which minimizes the total energy. As a consequence of the partitioning of the total energy (3.4), the Hamiltonian operator in the Kohn-Sham equations (3.12) contains

three terms, one for the kinetic energy, the second for the Coulomb potential and the third for the exchange-correlation potential.

The kinetic energy term is the standard second-order differential operator of one-particle Schrödinger equations and its construction does not require specific knowledge of a system. In contrast, the Coulomb potential operator,  $V_c(r)$  and the exchange-correlation potential operator,  $\mu_{xc}$  depend on the specific electron distribution in the system under consideration.

The Coulomb or electrostatic potential  $V_c(r)$  at point  $r$  is generated from the electric charges of all nuclei and electrons in the system. It can be evaluated directly in real space,

$$V_c(r) = -e^2 \sum_{\alpha} \frac{Z_{\alpha}}{|r-R_{\alpha}|} + e^2 \int \frac{\rho(r')}{|r-r'|} dr'. \quad 3.14$$

In condensed systems, it is more convenient to use Poisson's equation

$$\nabla^2 V_c(r) = -4\pi e^2 q(r), \quad 3.15$$

to calculate the electrostatic potential. Here,  $q(r)$  denotes both the electronic charge distribution  $\rho(r)$  and the positive point charges of the nuclei at positions  $R_{\alpha}$ .

The exchange-correlation potential is related to the exchange-correlation energy by

$$\mu_{xc}(r) = \frac{\partial E_{xc}[\rho(r)]}{\partial \rho(r)}. \quad 3.16$$

Equation (3.15) is formally exact in the sense that it does not contain any approximations to the complete many-body interactions.

Therefore, from the above discussions, the Kohn-Sham total energy functional can be expressed as

$$E = \frac{1}{2} \sum_{OCC} \varepsilon_i + U_{nn} - \frac{e^2}{2} \iint \frac{\rho(r)\rho(r')}{|r-r'|} drdr' + E_{xc}[\rho(r)] - \int \rho(r)\mu_{xc} dr. \quad 3.17$$

In practice however, the exchange-correlation energy (and thus the exchange-correlation potential) is not known and one has to make approximations which will be discussed in the following section.

### 3.2. Local density approximation

The Local density approximation (LDA) is the simplest approximation for non-magnetic systems assumes that the exchange-correlation energy is dependent only on the local electron density  $\rho(r)$  around each volume element [73]. LDA gives the correct sum rule for the exchange-correlation hole [74, 75]. The local density approximation is given by

$$E_{xc}[\rho] \approx \int \rho(r)\varepsilon_{xc}^0[\rho(r)]dr, \quad 3.18$$

where the exchange-correlation energy is taken from the known results of the many-electron interactions in an electron system of constant density. The LDA amounts to the following: at each point in a molecule or solid there exists a well-defined electron density. It is assumed that an electron at such a point experiences the same many-body response by the surrounding electrons as if the density of these surrounding electrons had the same value throughout the entire space as at the point of the reference electron.

### 3.3. Generalized gradient approximation

The generalized gradient approximation (GGA) improves the LDA definition by including the first derivatives of the electron density. Perdew [76], Becke [77],

Perdew and Wang [78] and Perdew, Burke and Ernzerhof [79] suggested gradient-corrected density functionals, which works as the remedy to the LDA as discussed in section 3.2. Gradient corrected density functionals have been studied extensively for molecular systems of the generalized gradient approximation (GGA), for example by Andzelm and Wimmer [80]. The exchange-correlation energy is approximated by the form:

$$E_{xc}^{GGA}[\rho \uparrow \rho \downarrow] = \int f(\rho \uparrow (r), \rho \downarrow (r), \nabla \rho \uparrow (r), \nabla \rho \downarrow (r)) \quad 3.19$$

that depends not only on the density at a particular coordinate  $r$  but also take into account the gradient of density at the same co-ordinate. This function has become popular in both quantum chemistry and condensed matter physics.

### 3.4. Plane-wave pseudopotential method

The pseudopotential is an effective potential constructed to replace the atomic all-electron potential (full-potential) such that core states are eliminated and the valence electrons are described by pseudo-wavefunctions with significantly fewer nodes. This allows the pseudo-wavefunctions to be described with far fewer Fourier modes, thus making plane-wave basis sets practical to use. In this approach usually, only the chemically active valence electrons are dealt with explicitly, while the core electrons are 'frozen', being considered together with the nuclei as rigid non-polarizable ion cores. It is possible to self-consistently update the pseudopotential with the chemical environment that it is embedded in, having the effect of relaxing the frozen core approximation, although this is rarely done [81, 82].

### 3.4.1. Plane-waves and pseudopotentials

Plane-waves and pseudopotentials are the hallmarks of the method and they form a very natural alliance. They are so fundamental that their strength and weakness deserve special attention. In the plane-wave pseudopotential method, the model system is constructed in 3D periodic supercell which allows Bloch's theorem to be applied to the electron wavefunctions:

$$\psi_{n,k}(r) = u_{n,k}(r)e^{(ik.r)}. \quad 3.20$$

The function  $u(r)$  has the periodicity of supercell. It can be of any suitable mathematical form and usually one chooses a series expansion in terms of a set of basis function. In PW pseudopotential, plane-waves are used for this expansion, so that each single-electron wavefunction  $\psi_{n,k}$  is written as

$$\psi_{n,k}(r) = \sum u_{n,k}(G)e^{i(k+G).r}. \quad 3.21$$

This  $u_{n,k}$  are the expansion coefficients. The wavevectors  $G$  are such that the plane-waves are commensurate with the supercell. Both the number of  $G$ -vectors in the sum and the number of  $k$ s considered should in principle be infinite. The exponential term is a plane-waves of wavevector  $k$  which must be commensurate with the entire system (i.e. not just the periodically-replicated cell). For an infinite system, there is an infinite number of  $k$  vectors, at each of which solutions for  $\psi_{n,k}$  exist. This simply reflects the fact that the number of electrons is infinite. However, a great simplification comes about when one realizes that the change in  $\psi_{n,k}$  with  $k$  becomes negligible for  $k$ -points that are close together. This means that one may calculate at a finite number of  $k$ -points. This is referred to as  $k$ -point sampling. The set of vectors  $\{G\}$ , on the other hand, should in principle be infinite to obtain an exact

representation of the wavefunction. This is never necessary because summing over a finite number of  $G$ 's will yield sufficient accuracy. Plane-waves basis set has many advantages:

- a) It is unbiased, so all space is treated the same
- b) It is complete
- c) There is a single convergence criterion
- d) Plane-waves are mathematically simple and their derivatives are products in  $k$ -space
- e) Plane-waves do not depend on atomic positions

and its disadvantage is that (i) the number of plane-waves needed is determined by the greatest curvature of the wavefunction and (ii) empty space has the same quality of representation and cost regions of interest. The advantages speak for themselves i.e. the first three mean that one can always ensure that the basis set is adequate for a calculation by increasing the number of plane-waves until the quantity of interest stops changing. In other words, the quality of the basis set depends on a single parameter, usually expressed as the energy of a free electron whose wavefunction has the same wavevector as the largest wavevector in the plane-wave basis,

$$E_c = \frac{\hbar^2(G+k)^2}{2m} . \quad 3.22$$

All plane-waves of 'energy' less than the cutoff energy  $E_c$  are used in the expansion. The mathematical simplicity of plane-waves means the method is easier to implement, crucially so for the calculation of ionic forces which adds little complexity or cost to the calculation. Equally important in this context is the originless nature of plane-waves. Their independence from atomic positions means that the forces do not depend on the basis set there are no 'Pulay' or 'wavefunction' forces [83]. Even



more important, new developments are easiest in plane-wave codes. An idea to calculate property is most rapidly realised in a plane-wave basis and even if other methods catch up in time, the plane-wave approach remains as the reference. From a computational point of view the first of the disadvantages appears to be very serious.

### **3.4.2. Pseudopotential approximation**

The rapid oscillations of the wavefunctions near to the nucleus, due to the very strong potential in the region and the orthogonality condition between different states, meaning that very large cutoff energy and hence basis set would be necessary. Fortunately, the study of Physics and Chemistry shows that the core electrons on different atoms are almost independent of the environment surrounding the atom and that only the valence electrons participate strongly in interactions between atoms. Thus, the core electron states may be assumed to be fixed and a pseudopotential may be constructed for each atomic species which takes into account the effects of the nucleus and core electrons [84, 85, 86].

The pseudopotential approximation allows the electronic wavefunctions to be expanded using a much smaller number of plane-wave basis states. It is well known that most physical properties of solids are dependent on the valence electrons to a much greater extent than on the core electrons. The pseudopotential approximation exploits this by removing the core electrons and replacing the strong ionic potential by a weaker pseudopotential that acts on a set of pseudo wavefunctions rather than the true valence wavefunctions. An ionic potential, valence wave function and corresponding pseudopotential and pseudo wave function are illustrated in Figure 3.1 [87]. The valence wavefunctions oscillate rapidly in the region occupied by the core

electrons due to the strong ionic potential in this region. These regions maintain the orthogonality between the core wavefunctions and the valence wavefunctions, which is required in Pauli's exclusion principle.

The pseudopotential is constructed in such a way that its scattering properties or phase shifts for the pseudo wavefunctions are identical to the scattering properties of the ion and the core electrons for the valence wavefunctions, but in such a way that the pseudo wavefunctions have no radial nodes in the core region. The phase shift produced by the ion core is different for each angular momentum component of the valence wave function and so the scattering from the pseudopotential must be angular momentum dependent.

The most general form for pseudopotential is

$$V_{NL} = \sum_{lm} |lm\rangle V_l \langle lm|, \quad 3.23$$

where  $\langle lm|$  are the spherical harmonics and  $V_l$  the pseudopotential for angular momentum  $l$ . Acting on the electronic wave function with this operator decomposes the wave function into the spherical harmonics, each of which is multiplied by the relevant pseudopotential  $V_l$ .

A pseudopotential that uses the same potential for all the angular momentum components of the wave function is called a local pseudopotential. Pseudopotential is a function only of the distance from the nucleus. It is possible to produce arbitrary, predetermined phase shifts for each angular momentum state with a local potential, but there are limits to the amount that the phase shifts can be adjusted for the different angular momentum states while maintaining the crucial smoothness and weakness of the pseudopotential. Without a smooth, weak pseudopotential it

becomes difficult to expand the wavefunctions using a reasonable number of plane-waves basis states.

In Figure 3.1, we see a comparison of a wavefunction in the Coulomb potential of the nucleus (blue) to the one in the pseudopotential (red). The real and the pseudowavefunction and potentials match above a certain cutoff radius  $r_c$ .

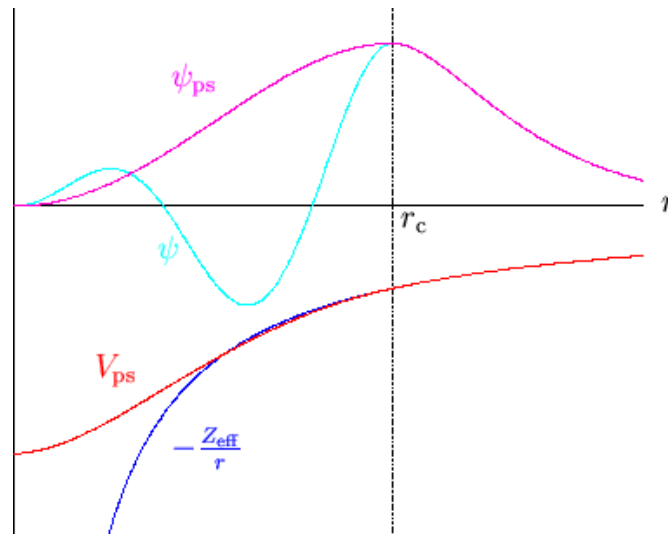


**Figure 3.1.** A schematic representation of the relationship between all-electron and pseudopotentials and wave-functions [87]. The radius at which all-electron and pseudopotentials and wavefunctions match is designated  $r_c$ .

### 3.5. Energy cutoff and $k$ -point sampling

Electronic states are allowed only at a set of  $k$ -points determined by the boundary conditions that apply to the bulk solid. The density of allowed  $k$ -points is proportional to the volume of the solid. The infinite numbers of electrons in the solid are accounted for by an infinite number of  $k$ -points and only a finite number of electronic states are occupied at each  $k$ -point [88].

The Bloch theorem changes the problem of calculating an infinite number of electronic wavefunctions to one of calculating a finite number of  $k$ -points [89]. The occupied states at each  $k$ -point contribute to the electronic potential in the bulk solid

so that in principle an infinite number of calculations are needed to compute this potential. However the electronic wavefunctions at  $k$ -points that are very close are identical. Hence it is possible to represent the electronic wavefunctions over a region of  $k$  space by the wavefunctions at the single  $k$ -point. In this case the electronic states at only a finite number of  $k$ -points are required to calculate the electronic potential and hence determine the total energy of the solid.

Methods have been devised for obtaining very accurate approximations to the electronic potential from a filled electronic band by calculating the electronic wavefunctions at special sets of  $k$ -points. The two most common methods are those of Chadi and Cohen [90] and Monkhorst and Pack [91]. Using these methods, the electronic potential and the total energy of an insulator can be obtained by calculating the electronic states at a very small number of  $k$ -points. A denser set of  $k$ -points is required to calculate the electronic potential and the total energy of a metallic system to define the Fermi surface precisely.

However, the computational cost of performing a very dense sampling of  $k$  space increases linearly with the number of  $k$ -points in the Brillouin zone (BZ). Density functional codes approximate these  $k$  space integrals with a finite sampling of  $k$ -points. Special  $k$ -points schemes have been developed to use the fewest possible  $k$ -points for a given accuracy, thereby reducing the computational cost. The most commonly used scheme is that of Monkhorst and Pack to generate efficient and accurate sets of special points in the BZ [91].

To compute accurately the properties of materials such as the total energy, force and stress we need to integrate over all the occupied electron states. The computational cost increased linearly with the number of  $k$ -points with the Brillouin zone. DFT

codes approximate these k-spacing integrals with a finite sampling of k-points, special k-points schemes have been developed to use the fewest possible k-points for a given accuracy, thereby reducing the computational cost. The number of k-points used depends entirely on the system as the treatment of metals, semiconductor and insulator are different.

Before any geometry optimization is important to calculate the energy cutoff for the system that will give accurate wave functions and total energy within the plane-wave pseudopotential. The importance of calculating energy cutoff and k-mesh is to get a good convergence of the total energy, however, the number of k-points depend on the system.

### **3.6. Computational codes**

The current study uses the plane-wave code CASTEP to investigate the properties of Zr-based alloys. CASTEP is a software package that uses density functional theory with a plane-waves basis set to calculate the electronic properties of solids from first principles. The other codes or platform used is the VCA and molecular dynamics DMol<sup>3</sup> code to deduce the thermodynamic properties.

#### **3.6.1. CASTEP code**

The CASTEP [92] program is a first principle quantum mechanical (*ab initio*) code for performing electronic structure calculations. Within the density functional formalism, it can be used to simulate a wide range of materials including crystalline solids, surfaces, molecules, liquids and amorphous materials; the properties of any material that can be thought of as an assembly of nuclei and electrons can be calculated with the only limitation being the finite speed and memory of the computers being used.

This approach to simulation is extremely ambitious given that the aim is to use no experimental data, but to rely purely on quantum mechanics.

CASTEP is a fully-featured first principles code and as such its capabilities are numerous. Aiming to calculate any physical property of the system from first principles, the basic quantity is the total energy from which many other quantities are derived. For example the derivative of total energy concerning atomic positions results in the forces and the derivative concerning cell parameters give stresses. These are then used to perform full geometry optimizations and possibly finite temperature molecular dynamics. Furthermore, symmetry and constraints (both internal and external to the cell) can be imposed in the calculations, either as defined by the user, or automatically using in-built symmetry detection.

The total-energy code used, CASTEP, performs a variational solution to the Kohn-Sham equations by using a density mixing scheme [58] to minimize the total energy and also conjugate gradients to relax the ions under the influence of the Hellmann-Feynman forces. CASTEP uses fast Fourier transforms (FFT) to provide an efficient way of transforming various entities (wavefunctions, potentials) from real to reciprocal space and back as well as to reduce the computational cost and memory requirement for operating with the Hamiltonian on the electronic wavefunctions, a plane-wave basis for the expansion of the wavefunctions. The convergence of this expansion is controlled by a single parameter, namely the highest frequency at which the series is terminated (conventionally defined as the highest kinetic energy of a plane-wave).

A summary of the methodology for electronic structure calculations as implemented in CASTEP is as follows: a set of one-electron Schrödinger (Kohn-Sham) equations

are solved using the plane-wave pseudopotential approach. The wavefunctions are expanded in a plane wave basis set defined by the use of periodic boundary conditions and Bloch's Theorem. The electron-ion potential is described employing *ab initio* pseudopotentials within both norm-conserving and ultrasoft formulations.

Direct energy minimisation schemes are used to obtain self-consistently the electronic wavefunctions and corresponding charge density. In particular the conjugate gradient and density mixing schemes are implemented. Also, the robust electron ensemble DFT approach can be used for systems with partial occupancies (in particular, metals).

#### **3.6.1.1. Virtual crystal approximation**

The application of first-principles electronic band structure methods to the study of disordered alloys and solid solutions requires some approximation for the treatment of the alloy disorder. Virtual crystal approximation (VCA) offers technically the simplest approach, allowing calculations on disordered systems to be carried out at the same cost as calculations for ordered structures. Virtual crystal approximation is one of the approaches for dealing with disorder in first-principles calculations [93].

Virtual crystal approximation is a much simpler and computationally less expensive approach where one studies a crystal with the primitive periodicity, but it ignores any possible short-range order and assumes that on each potentially disordered site there is a virtual atom which interpolates between the behaviour of the actual components. This approach neglects such effects as local distortions around atoms and cannot be expected to reproduce the finer details of the disordered structures very accurately. The VCA implementation in CASTEP is capable of correctly describing several mixture atoms.

The basic ideas of the workable VCA implementation for DFT methods, which is for the pseudopotential based techniques, were set out by Bellaiche and Vanderbilt [94].

The implementation of VCA with ultrasoft potentials can be expressed as:

$$V_{ext}(r, r') = \sum_I \sum_{\alpha} w_{\alpha}^I V_{ps}^{\alpha}(r - R_{I\alpha}, r' - R_{I\alpha}). \quad 3.29$$

The expression is used for the generation of the total external potential as the sum of the nonlocal potentials of each atomic species,  $\alpha$ , taken with the weights,  $w$ , of the component atoms in the mixture of Zr-Nb (Co, Sn). This technique has seen wide use in band structure calculations [95, 96, 97].

### 3.6.2. Molecular dynamics

Molecular dynamics involves the stepwise integration of Newton's equations from a given starting point. It is the most natural method of performing equilibrium statistical-mechanical calculations through a simulation. MD in total energy DFT schemes is implemented in essentially the same way as in conventional forcefield-based methods. The main difference is that the atomic forces are derived by solving DFT equations rather than from empirical potentials of interatomic interactions. Electrons are kept on the Born-Oppenheimer surface employing explicit electronic structure optimization after each MD step. A side effect of this is that the evaluation of force and energy from first principles is always the most computationally expensive part of ab initio MD. As a result, the efficiency of the MD step itself has no impact on the speed of the calculation. MD in DMol3 is based on the velocity Verlet algorithm for the integration of the equation of motion. The implemented algorithm performs the Yoshida-Suzuki multiple-step numerical integration of varying quality, depending on the choice of interpolation parameter [99, 100].



Integrating Newton's equations of motion allows you to explore the constant energy surface of a system. However, most natural phenomena occur under conditions where the system is exposed to external pressure and/or exchanges heat with the environment. Under these conditions, the total energy of the system is no longer conserved and extended forms of molecular dynamics are required.

Several methods are available for controlling temperature. Depending on which state variables that is the energy,  $E$ , enthalpy,  $H$  (that is,  $E + PV$ ), number of particles,  $N$ , pressure,  $P$ , stress,  $S$ , temperature,  $T$ , and volume,  $V$  - are kept fixed, different statistical ensembles can be generated. A variety of structural, energetic, and dynamic properties can then be calculated from the averages or the fluctuations of these quantities over the ensemble generated.

Both isothermal (where heat is exchanged with a temperature bath to maintain a constant thermodynamic temperature) and adiabatic (where no heat exchange occurs) ensembles are available: that is constant energy, constant volume (NVE) and constant temperature, constant volume (NVT).

### **3.6.3. DMol<sup>3</sup> code**

DMol<sup>3</sup> is a commercial and academic software package that uses DFT with a numerical radial function basis set to calculate the electronic properties of molecules, clusters, surfaces and crystalline solid materials from first principles. It can either use gas phase boundary conditions or 3d periodic boundary conditions for solids or simulations of lower-dimensional periodicity. It has also pioneered the use of the conductor-like screening model COSMO Solvation Model for quantum simulations of solvated molecules and recently of wetted surfaces. DMol3 permits geometry optimization and saddle point search with and without geometry constraints, as well

as the calculation of a variety of derived properties of the electronic configuration [98].

### **3.7. Implementation of codes**

In the current study, we used a plane wave pseudopotential method as implemented in CASTEP code [59] based on the density functional theory as discussed in Section 3.1. The other code used is DMol<sup>3</sup> which implements MD approach [98].

#### **3.7.1. CASTEP approach**

The electronic exchange-correlation potential was described within the generalized gradient approximation (GGA) as parameterized by Perdew, Burke and Enzerhof (PBE) [78]. Firstly, the convergence tests were performed to establish the appropriate cutoff energy and k-points parameters suitable to converge the Zr-Nb-X systems. The structure is considered converged when the difference between consecutive points is 0.01 eV. Thus, the plane wave pseudopotentials method with a cutoff of 400 eV was used to describe the interaction between electrons and ions. This was sufficient enough to converge the total energy of the system to within 1 meV difference. Interactions in the Brillouin zone were performed with special k-points of 18 x 18 x 10 mesh parameters in accordance with Monkhorst and Pack (1976) scheme. The SCF convergence of  $1.0e^{-8}$  eV was used for accurate convergence using Meth Fessel-Paxton smearing of  $\sigma = 0.2$  eV. A full geometry optimization calculation was performed to find the ground state at different compositions. Before the calculations of elastic constants, electronic structure, and mechanical, the structure was fully relaxed with respect to the volume, shape, and internal atomic positions until the atomic forces were less than 0.01 eV/Å for the unit cell. This is done to obtain the lowest energy (ground state) where the structure is in

its relaxed state or lowest energy. The equilibrium parameters correspond to the minimum energy or ground state structure. This structure is then used to predict all other properties including thermodynamics, elastic, mechanical and electronic.

In the case of ternary addition or alloying, virtual approximation (VCA) [94] was used to introduce a small amount of Co and Sn concentrations to form various compositions of  $Zr_{78}Nb_{22-x}X_x$  and  $Zr_{50}Nb_{50-x}X_x$  solid solutions. It was ascertained that the symmetry of the parent structure is maintained/kept to achieve consistent and reliable data.

### **3.7.2 DMol3 approach**

The DMol<sup>3</sup> [98] was used to calculate the temperature dependence of Zr-based alloys, using NVT ensemble. The temperature was kept constant for each single run up to 2600 K. The time step was set to 25.0 fs and the total simulation time of 250 ps for 10000 steps, then the corresponding binding energies were used to evaluate the dependence of Sn and Co additions. Furthermore, the elastic constants were calculated using the maximum strain amplitude of  $\pm 0.003$  with 4 steps for each strain. The application of strain on the lattice implies the lowering of symmetry from the crystal, therefore very accurate total-energy calculations are key, thus the equivalent number of k-points were used for  $Zr_{78}Nb_{22-x}X_x$  and  $Zr_{50}Nb_{50-x}X_x$  alloys.

### **3.7.3. Flow chart on computational approach**

Figure 3.2 summarises the steps taken using the computational codes and the properties that have been calculated. The description on the usage of the codes and computational criterion and parameters set are given in section 3.7.1 and 3.7.2.

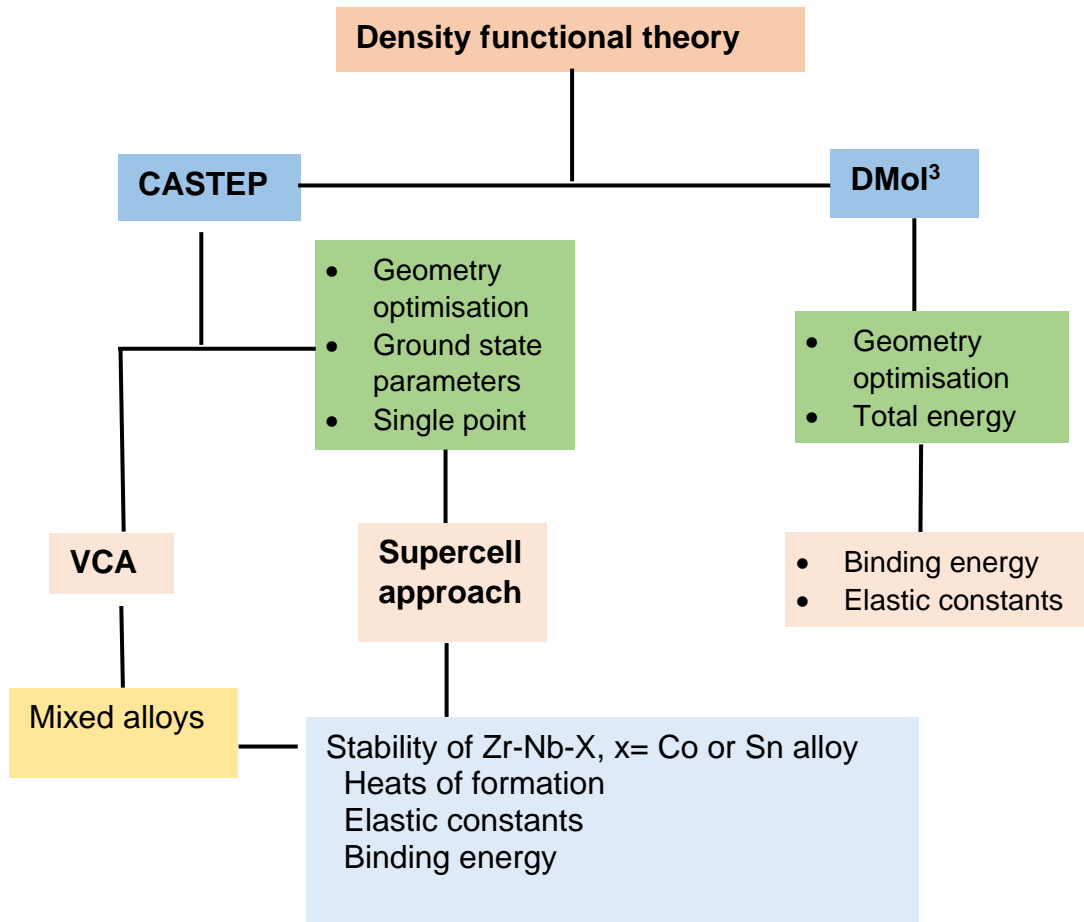


Figure 3.2. Flow chart showing computational approach used in the study.

## CHAPTER 4

### 4. Structural properties and heats of formation

In this chapter, we present and discuss the equilibrium lattice parameters, volume and heats of formation for Zr-Nb and Zr-Nb-Co systems. Firstly, we will discuss the pure Zr system, showing the convergence tests, cutoff energy and k-points. The geometry optimization calculations on pure Zr and Nb, binary Zr-Nb systems and ternary alloys will be discussed. The structural stability with respect to heats of formation will also be discussed, in particular for binary Zr-Nb systems and ternary Zr-Nb-Co systems. The choice of alloying addition is guided by literature (as described in Chapter 2).

#### 4.1. VCA model

The  $\alpha$ -Zr is a primitive hexagonal structure with a space group of P63/mmc, the lattice parameter of ( $a = 3.231 \text{ \AA}$  and  $c = 5.171 \text{ \AA}$ ) and cell volume of  $53.75 \text{ \AA}^3$ ; and Nb is a body-centered cubic structure with a space group of IM-3M; lattice parameter of ( $a = 3.008 \text{ \AA}$ ) and volume of  $35.96 \text{ \AA}^3$  [92] as shown in Figure 4.1. The structures were used to construct the various systems under study.

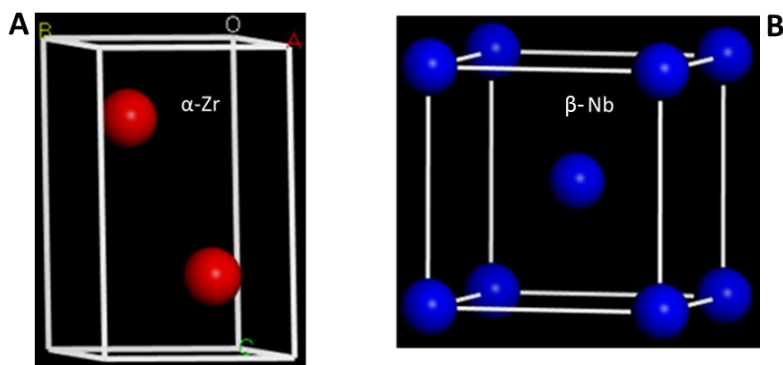
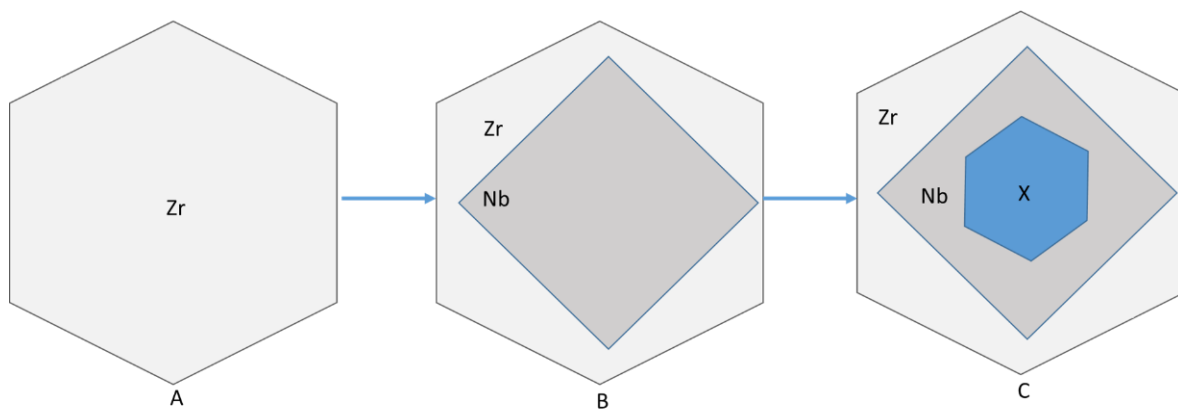


Figure 4.1. The (A)  $\alpha$ -Zr and (B)  $\beta$ -Nb structures.

The binary Zr-Nb and ternary Zr-Nb-X systems were constructed by the solute solution approach [101]. This approach is substitutional since the solute ( $\alpha$ -Zr) and solvent (Nb) atoms are distributed over a given crystal lattice, while in this case is hcp. The compositions were achieved by maintaining the symmetry of  $\alpha$ -Zr, with gradual additions of Nb to form compounds such as  $Zr_{78}Nb_{22}$ ,  $Zr_{97}Nb_3$ ,  $Zr_{97.5}Nb_{2.5}$ ,  $Zr_{98.1}Nb_{1.9}$ ,  $Zr_{98.8}Nb_{1.2}$  and  $Zr_{99}Nb_1$ . Figure 4.2 shows the schematic representation of forming these alloys, starting with Zr then the addition of Nb to form a binary system (Figure 4.2 B) and ternary systems with X elements (Figure 4.2 C).



**Figure 4.2. A schematic representation of a VCA model showing step-wise construction of the (B) binary and (C) ternary systems with the alloying elements (Nb and X) doped on Zr sublattice.**

#### 4.2. Convergence test

The importance of performing convergence tests of energy cutoff and k-point mesh is to achieve the accurate total energy and ground-state properties of a system. It is also important to note that the number of k-points depends on the system of interest, for example, metals require denser k-points than semiconductors. To achieve the desirable convergence, single point energy calculations were performed starting with a default parameter, which can be improved depending on the results obtained. At

each single point calculation, the total energy, volume and lattice parameter were recorded for analysis.

#### 4.2.1. The convergence of cutoff energy

The cutoff energy was determined from a series of single-point energy at a fixed default k-points. The default k-spacing as described by Monkhorst and Pack [91] has been used, taking into account that metallic systems require better sampling. Figure 4.3, shows the total energy against cutoff energy for  $\alpha$ -Zr,  $\alpha$ -Nb, and binary Zr-Nb and  $Zr_{78}Nb_{22}$  systems. It can be seen that the energy increases as the cutoff energy is increased. The plot reaches a constant slope, implying that the energy change is minimal. At this point, the structure has reached convergence with regard to the total energy and cutoff energy.

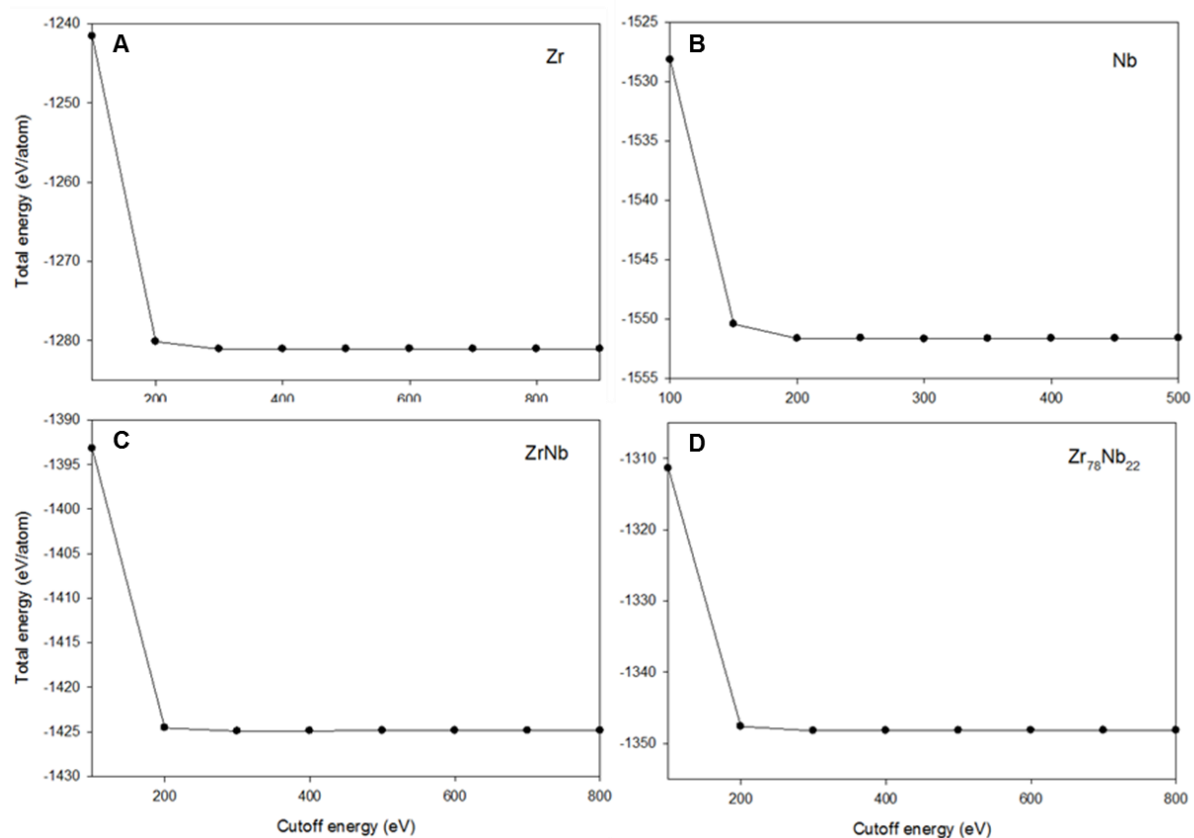


**Figure 4.3.** The graph of total energy against cutoff energy for (A) Zr, (B) Nb, (C) Zr-Nb and (D)  $Zr_{78}Nb_{22}$  alloys.

This trend is similar for Zr, Nb, Zr-Nb and  $Zr_{78}Nb_{22}$  systems. From a cutoff of 300 eV, the graph shows a zero slope and thus the energy cutoff of 400 eV was chosen for the Zr-based systems under investigation.

#### 4.2.2. Convergence of k-points

The total energy with regard to the k-points was performed to determine the appropriate number of k-point for Zr-based systems. This is done by varying the k-points setting at constant energy of 400 eV. Note that the total energy against the k-points is deemed converged when the difference between two consecutive points is less or equal to 1 meV per atom ( $\approx 1 \text{ meV/atom}$ ) [102]. This was also achieved with the idea that an increased k-point set reduces the finite basis set correction and makes cell relaxation more accurate at a fixed energy cutoff.

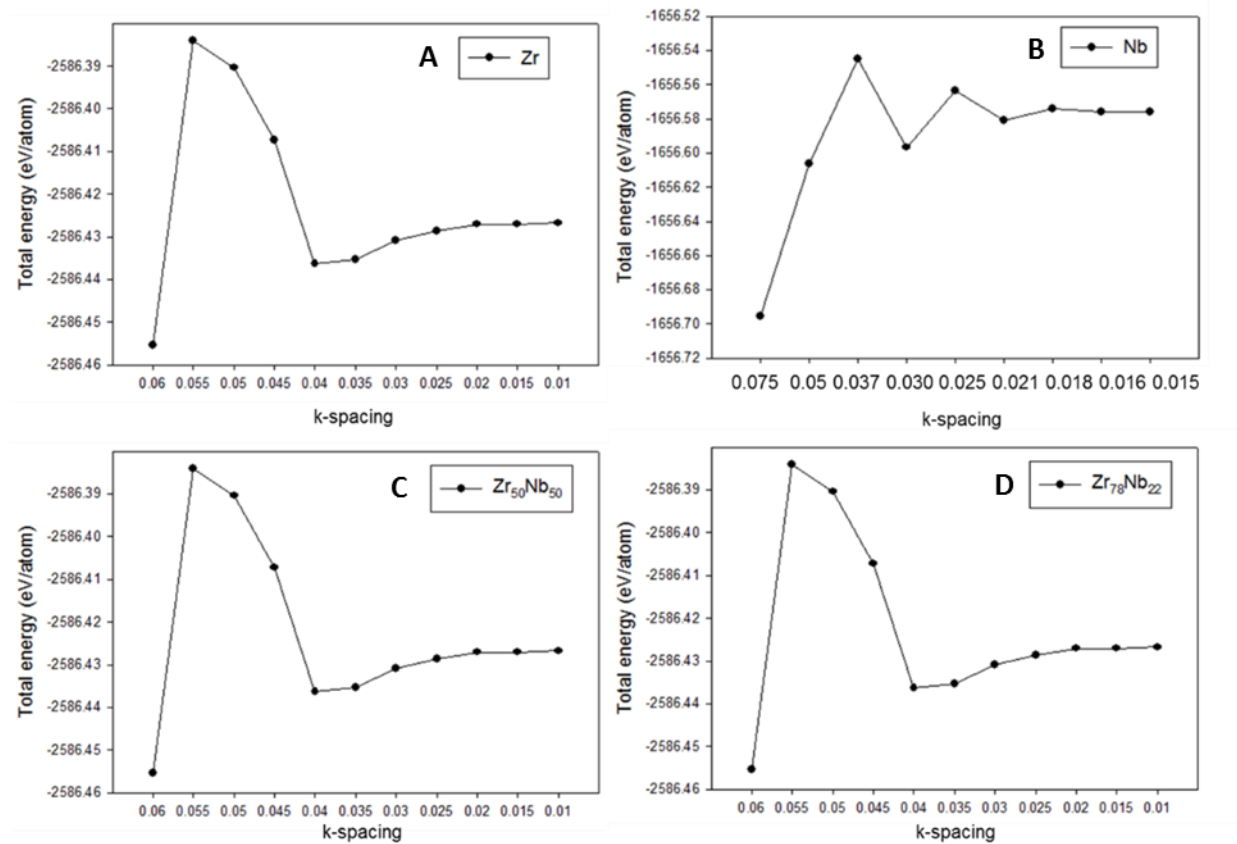


**Figure 4.4.** Displays the graphs of final energy against the k-points for (A)  $\alpha$ -Zr, (B) Nb, (C)  $Zr_{50}Nb_{50}$  and (D)  $Zr_{78}Nb_{22}$  systems respectively.



The total energy against the k-points spacing for determining the mesh parameters for the Nb and Zr-based systems is shown in Figure 4.4. For example, the pure systems Zr in A and Nb in B plots showed that at 12x12x6 (k-spacing of 0.03) and 12x12x12 (k-spacing of 0.025) k-points mesh parameters has already converged to within 1meV/atom energy difference, satisfying the criterion discussed above. We also observed that for the binary systems Zr-Nb and Zr<sub>78</sub>Nb<sub>22</sub> the convergence of k-points was achieved at 12x12x6 as shown in figure 4.3 C and D.

Thus, the convergence was achieved with special *k*-points of 18x18x10 for Zr, ZrNb and Zr<sub>78</sub>Nb<sub>22</sub> as shown in Figure 4.4 A, C and D, respectively whereas convergence of Nb structure was achieved with special *k*-points of 14x14x14 (Figure 4.4 B). These parameters will be used to determine the ground-state properties of Zr and Zr-based systems under study. An equivalent number of k-points will be used for other Zr-Nb and Zr-Nb-X based compositions in this work.

### **4.3. Geometry optimization**

Full geometry optimization calculations for  $\alpha$ -Zr structure and Zr-Nb alloys were performed in which all structural parameters (lattice constants and internal coordinate) were relaxed within the CASTEP code [92] allowing cell shape and volume to change. The geometry optimization was performed within the GGA-PBE using the energy cutoff of 400 eV and k-points as discussed above for Zr, Nb, ZrNb and Zr<sub>78</sub>Nb<sub>22</sub> systems. That is, a special k-points mesh of 14x14x14 for Nb and 18x18x10 for  $\alpha$ -Zr, binaries of Zr-Nb and Zr<sub>78</sub>Nb<sub>22</sub> and also for the ternary alloys were used to perform the calculations. Moreover, these parameters were used to perform optimizations for other structures of Zr-Nb-X where X is any metal of interest such as Co and Sn, etc. Table 4.1 summarizes the equilibrium parameters of pure and binary

systems. The predicted lattice parameters for Zr ( $a = 3.231 \text{ \AA}$  and  $c = 5.171 \text{ \AA}$ ) compares well to the experimental values ( $a = 3.231 \text{ \AA}$  and  $c = 5.147 \text{ \AA}$ ) [92] while that of  $\text{Zr}_{50}\text{Nb}_{50}$  ( $a = 3.041 \text{ \AA}$  and  $c = 5.092 \text{ \AA}$ ) and  $\text{Zr}_{78}\text{Nb}_{22}$  ( $a = 3.151 \text{ \AA}$  and  $c = 5.099 \text{ \AA}$ ) were found to be reasonable. It is noted that Nb gave lattice parameters in good agreement with the experiment to within 1%. Moreover, the addition of Nb in  $\alpha$ -Zr has been shown to affect the volume slightly since Nb has a smaller radius compared to Zr.

**Table 4.1. Show the equilibrium lattice parameters and volume for  $\alpha$ -Zr, Nb,  $\text{Zr}_{50}\text{Nb}_{50}$  and  $\text{Zr}_{78}\text{Nb}_{22}$  structures.**

Structure	Lattice constants (calc.)			Lattice constants (theoretical)		
	a $\text{\AA}$	c $\text{\AA}$	V $(\text{\AA}^3)$	a $\text{\AA}$	c $\text{\AA}$	V $(\text{\AA}^3)$
Zr	3.231	5.171	53.98	3.231	5.148	53.74
Nb	3.306	-	35.96	3.300	-	35.94
$\text{Zr}_{50}\text{Nb}_{50}$	3.041	5.092	47.09			
$\text{Zr}_{78}\text{Nb}_{22}$	3.151	5.099	50.63			

#### 4.3.1. Zr-Nb system

In this section, we focus on the Zr-Nb alloys of different concentrations considered to study the binary alloy additions in this work. A wide range of concentrations was explored to understand the influence of Nb addition on the  $\alpha$ -Zr. Furthermore, these systems will be used to develop the ternary alloys by the addition of either Co or Sn.

Some of the calculations are performed using the trial and error method, which in this case will be taken as a prediction to guide experiments. The binary alloys of  $Zr_{99}Nb_{1.0}$ ,  $Zr_{98.8}Nb_{1.2}$ ,  $Zr_{98.1}Nb_{1.9}$ ,  $Zr_{97.5}Nb_{2.5}$ ,  $Zr_{97}Nb_3$ ,  $Zr_{78}Nb_{22}$ ,  $Zr_{78}Nb_{22}$  and  $Zr_{50}Nb_{50}$  were evaluated to study the effect of alloying with small and large concentration. This is performed to enhance the properties of  $\alpha$ -Zr for applications in nuclear and other industrial environments.

Table 4.2 shows the predicted lattice parameters of the binary Zr-Nb alloys. The predicted results show that as we increase the Nb content in the  $\alpha$ -Zr system the “a” and “c” parameters decrease hence the volume. Kharchenko et.al. have reported that there is a good quantitative correspondence with experimental results for small values of Nb concentration. A reduced volume contributes to the stiffness of the structures hence the structures are ascribed to better stability especially for low Nb concentrations [103]. As such, we have considered this set of ( $Zr_{99}Nb_{1.0}$ ,  $Zr_{98.8}Nb_{1.2}$ ,  $Zr_{98.1}Nb_{1.9}$ ,  $Zr_{97.5}Nb_{2.5}$ ,  $Zr_{97}Nb_3$ ,  $Zr_{78}Nb_{22}$ ,  $Zr_{78}Nb_{22}$  and  $Zr_{50}Nb_{50}$ ) binary alloys for investigations at smaller and larger Nb contents.

#### 4.3.2. Heats of formation for Zr-Nb alloys

The thermodynamic stability was performed for the Zr-Nb alloys as deduced from the heats of formation. The heat of formation was calculated as:

$$\Delta H_f = E_c - \sum_i x_i E_i, \quad 4.1$$

where  $E_c$  is the calculated total energy of the compound,  $x_i$  is the atomic percentage of element  $i$  in the compound and  $E_i$  is the calculated total energy of element  $i$  in the compound.

The predicted heats of formation results for ( $Zr_{99}Nb_{1.0}$ ,  $Zr_{98.8}Nb_{1.2}$ ,  $Zr_{98.1}Nb_{1.9}$ ,  $Zr_{97.5}Nb_{2.5}$ ,  $Zr_{97}Nb_3$ ,  $Zr_{78}Nb_{22}$ ,  $Zr_{78}Nb_{22}$  and  $Zr_{50}Nb_{50}$ ) binary systems are listed in

table 4.2. We consider the effect of Nb addition on  $\alpha$ -Zr to predict the thermodynamic stability at different concentrations. The calculated heats of formation ( $\Delta H_f$ ) are dependent on Nb content, it is seen that  $\Delta H_f$  increase with increasing Nb concentration. A negative value ( $\Delta H_f < 0$ ) is considered thermodynamically stable otherwise unstable. Interestingly, the  $\alpha$ -Zr becomes more negative as the Nb content increases which could stabilise the system.

**Table 4.2. The lattice parameters, volume and heat of formation for  $Zr_{99}Nb_{1.0}$ ,  $Zr_{98.8}Nb_{1.2}$ ,  $Zr_{98.1}Nb_{1.9}$ ,  $Zr_{97.5}Nb_{2.5}$ ,  $Zr_{97}Nb_3$ ,  $Zr_{78}Nb_{22}$ ,  $Zr_{78}Nb_{22}$  and  $Zr_{50}Nb_{50}$  systems.**

Structure	Lattice parameter and Volume			$\Delta H_f$ (eV/atom)
	a (Å)	c (Å)	V (Å <sup>3</sup> )	
Zr	3.231	5.171	53.98	-
$Zr_{99}Nb_{1.0}$	3.270	5.119	54.73	-0.561
$Zr_{98.8}Nb_{1.2}$	3.270	5.120	54.74	-0.662
$Zr_{98.1}Nb_{1.9}$	3.268	5.115	54.62	-1.023
$Zr_{97.5}Nb_{2.5}$	3.266	5.112	54.52	-1.324
$Zr_{97}Nb_3$	3.264	5.110	54.44	-1.571
$Zr_{78}Nb_{22}$	3.151	5.103	50.67	-7.602
$Zr_{50}Nb_{50}$	3.041	5.092	47.09	-8.653

#### 4.4. Effect of Co addition on binary Zr-Nb systems

In this section, we focus on the effect of Co addition on the binary  $Zr_xNb_x$  alloy with different concentrations. Note that the calculations were performed using VCA on the  $Zr_xNb_x$  structure (as discussed in section 4.1). We discuss the DFT results particularly the lattice constants and heats of formation. The lattice constants give information about the structural change concerning lattice parameter and volume whereas the heats of formation describe the thermodynamic stability. Thus, geometry optimization calculations were performed for the  $Zr_{99}Nb_{1.0-x}Co_x$ ,  $Zr_{98.8}Nb_{1.2-x}Co_x$ ,  $Zr_{98.1}Nb_{1.9-x}Co_x$ ,  $Zr_{97.5}Nb_{2.5-x}Co_x$ ,  $Zr_{97}Nb_{3-x}Co_x$  and  $Zr_{78}Nb_{22-x}Co_x$  alloy systems by allowing both atomic positions and volume to relax until a ground state energy was achieved. A detailed discussion of the effect of Co addition will be discussed in the following sub-sections.

#### **4.4.1. Co addition on $Zr_{99}Nb_{1.0}$ alloy**

Table 4.3 shows the lattice constants (a, c and V) as well as the heats of formation for Zr and  $Zr_{99}Nb_{1.0-x}Co_x$  systems. Note that the Zr concentration is kept unchanged/constant and we only vary the Nb concentration. We chose three compositions that are limited by Nb content since more compositions did not show any significant difference.

**Table 4.3. Structure, lattice constants and heats of formation for Zr<sub>99</sub>Nb<sub>1.0</sub> system.**

	Lattice constants			$\Delta H_f$ (eV/atom)
	a (Å)	c (Å)	V (Å <sup>3</sup> )	
Zr	3.231	5.171	53.98	-
Zr <sub>99</sub> Nb <sub>1.0</sub>	3.270	5.119	54.73	-0.562
Zr <sub>99</sub> Nb <sub>0.8</sub> Co <sub>0.2</sub>	3.260	5.120	54.41	0.391
Zr <sub>99</sub> Nb <sub>0.2</sub> Co <sub>0.8</sub>	3.221	5.141	53.33	2.662

The 0.2 and 0.8 at. % Co addition to the system reduces the “a” parameter hence the volume reduces, this is due to the small atomic radius of Co compared to Nb (Zr > Nb > Co in atomic radius) which points to the stability of the systems. The heats of formation become positive (condition of instability) with Co addition, the structures are considered thermodynamically unstable ( $\Delta H_f > 0$ ).

#### 4.4.2. Co addition on Zr<sub>98.8</sub>Nb<sub>1.2</sub> alloy

The lattice parameter for a = 3.270 Å and c = 5.120 Å and  $\Delta H_f$  of -0.66 eV/atom for Zr<sub>98.8</sub>Nb<sub>1.2</sub> alloy were noted before ternary alloying or addition of Nb. There was a slight increase in lattice parameter “a” whereas a slight decrease occurred in lattice parameter “c” upon alloying. As the Co content is increased the volume is reduced. Most notably the heat of formation increases and gives a positive value ( $\Delta H_f > 0$ ) which implies that the structure becomes unstable.

**Table 4.4. Structural parameter and heats of formation for  $Zr_{98.8}Nb_{1.2-x}Co_x$  system (effect of Co addition).**

Structure	Lattice constants			$\Delta H_f$ (eV/atom)
	a (Å)	c (Å)	V (Å <sup>3</sup> )	
Zr	3.231	5.171	53.98	
$Zr_{98.8}Nb_{1.2}$	3.270	5.120	54.75	-0.662
$Zr_{98.8}Nb_{0.8}Co_{0.4}$	3.249	5.122	54.07	1.161
$Zr_{98.8}Nb_{0.2}Co_{1.0}$	3.194	5.213	53.18	3.024

#### 4.4.3. Co addition on Zr<sub>98.1</sub>Nb<sub>1.9</sub> alloy

The lattice parameters for the Zr<sub>98.1</sub>Nb<sub>1.9</sub> alloy system were predicted to be  $a = 3.268$  Å and  $c = 5.115$  Å (see Table 4.5). Moreover, the lattice parameters decrease as the Nb content is increased, the volume slightly decreases due to this effect. It is observed that the  $\Delta H_f$  increases as Co content is introduced, similar to the previous cases. An increase in  $\Delta H_f$  suggests that the structure becomes unstable. This is observed for  $\Delta H_f$  of -1.024 eV/atom where the addition of Co gave 0.801 and 2.472 eV/atom, respectively, thus thermodynamically unstable.

**Table 4.5. Structure, lattice parameter and heats of formation for Zr<sub>98.1</sub>Nb<sub>1.9-x</sub>Co<sub>x</sub> system (effect of Co addition).**

Structure	Lattice constants			$\Delta H_f$ (eV/atom)
	a (Å)	c (Å)	V (Å <sup>3</sup> )	
Zr	3.231	5.171	53.98	
Zr <sub>98.1</sub> Nb <sub>1.9</sub>	3.268	5.115	54.62	-1.024
Zr <sub>98.1</sub> Nb <sub>1.5</sub> Co <sub>0.4</sub>	3.246	5.121	53.96	0.801
Zr <sub>98.1</sub> Nb <sub>1.0</sub> Co <sub>0.9</sub>	3.211	5.164	53.24	2.472

#### 4.4.4. Co addition on Zr<sub>97.5</sub>Nb<sub>2.5</sub> alloy

We now consider the structural parameter and heats of formation for Zr<sub>97.5</sub>Nb<sub>2.0-x</sub>Co<sub>x</sub> systems based on the effect of Co addition. The lattice parameter “a” for Zr<sub>97.5</sub>Nb<sub>2.5</sub> shows a slight decrease with a slight volume change for 0.5 to 1.0 at. % Co then a sudden decrease is observed for 1.2 to 2 at. % Co as well as the volume decrease



except for 2 at. % Co addition as shown in table 4.6. The heats of formation increase up to 1.2 at. % Co then decreases to  $\Delta H_f$  of 0.13 eV/atom. The downward trend for lattice constants and  $\Delta H_f$  could suggest that a further Co addition could yield a thermodynamically stable structure, in this case, it was limited by the Nb content.

**Table 4.6. Structural parameter and heats of formation for  $Zr_{97.5}Nb_{2.5-x}Co_x$  systems (effect of ternary Co addition).**

Structure	Lattice constants			$\Delta H_f$ (eV/atom)
	A (Å)	c (Å)	V (Å <sup>3</sup> )	
Zr	3.231	5.171	53.98	
$Zr_{97.5}Nb_{2.5}$	3.266	5.112	54.53	-1.321
$Zr_{97.5}Nb_{2.0}Co_{0.5}$	3.239	5.121	53.72	0.912
$Zr_{97.5}Nb_{1.7}Co_{0.8}$	3.223	5.135	53.34	1.933
$Zr_{97.5}Nb_{1.5}Co_{1.0}$	3.195	5.197	53.05	2.414
$Zr_{97.5}Nb_{1.3}Co_{1.2}$	2.953	5.983	51.97	2.664
$Zr_{97.5}Nb_1Co_{1.5}$	2.911	6.133	51.97	2.473
$Zr_{97.5}Nb_{0.7}Co_{1.8}$	2.796	6.440	50.34	1.262
$Zr_{97.5}Nb_{0.5}Co_2$	3.395	4.789	55.19	0.131

#### 4.4.5. Effect of Co addition on $Zr_{97}Nb_3$ alloy

The  $Zr_{97}Nb_{3-x}Co_x$  systems are investigated based on lattice constant and heats of formation to further understand the effect of the Co content at various concentrations. Now, in Table 4.9 it is indicated that the increase in Co content

shows an effect on the lattice constants, volume and  $\Delta H_f$  as we already demonstrated in the previous sections. However, we observed that at a concentration of less than 0.2 at. % Co the structure is unstable ( $\Delta H_f > 0$ ), while above this concentration, the structure becomes stable ( $\Delta H_f < 0$ ). The  $\Delta H_f$  is more negative with 2.5 at. % Co addition (thermodynamically stable).

**Table 4.7. Structure, lattice parameter and heats of formation for  $Zr_{97}Nb_{2.5-x}Co_x$  systems (the effect of Co addition).**

Structure	Lattice constants			$\Delta H_f$ (eV/atom)
	a (Å)	c (Å)	V (Å <sup>3</sup> )	
Zr	3.231	5.171	53.98	
$Zr_{97}Nb_3$	3.264	5.110	54.44	-1.571
$Zr_{97}Nb_{2.5}Co_{0.5}$	3.237	5.120	53.64	0.661
$Zr_{97}Nb_{2.0}Co_{1.0}$	3.194	5.192	52.97	2.183
$Zr_{97}Nb_{1.5}Co_{1.5}$	2.920	6.149	52.43	2.283
$Zr_{97}Nb_{1.0}Co_{2.0}$	3.508	5.196	63.94	0.032
$Zr_{97}Nb_{0.5}Co_{2.5}$	4.184	8.058	141.06	-4.71

#### 4.4.6. Effect of Co addition on $Zr_{78}Nb_{22}$ alloy

We investigate the  $Zr_{78}Nb_{22-x}Co_x$  system to further understand the effect of Co addition with larger concentrations as shown in Table 4.8. When the Co content is added to the  $Zr_{78}Nb_{22}$  system, the lattice parameters slightly decrease for 1 at. % Co, thereby destabilising the system. Notably, at 1 and 2 at. % Co addition the structure gave reasonable energies ( $\Delta H_f < 0$ ). However, as Co is increased, the structure gave

more negative values which are unreasonable because the higher energies could be misleading (unstable) as such the stability is enhanced from 0 to 2 at. % Co. This could imply that only a sizeable amount of Co up to 3 at. % is reasonable for industrial applications. Further that the VCA fails to make predictions for high Co content.

**Table 4.8. Structure, lattice parameter and heats of formation for  $Zr_{78}Nb_{22-x}Co_x$  (effect of Co addition)**

Structure	Lattice constants			$\Delta H_f$ (eV/atom)
	a (Å)	c (Å)	V (Å <sup>3</sup> )	
Zr	3.231	5.171	53.98	
$Zr_{78}Nb_{22}$	3.151	5.103	50.67	-7.601
$Zr_{78}Nb_{21}Co_1$	3.121	5.154	50.20	-3.442
$Zr_{78}Nb_{20}Co_2$	3.851	3.815	56.57	-3.993
$Zr_{78}Nb_{19}Co_3$	3.050	4.833	44.96	-16.343
$Zr_{78}Nb_{18}Co_4$	3.270	5.158	55.15	-49.912
$Zr_{78}Nb_{17}Co_5$	3.460	4.799	57.45	-59.111
$Zr_{78}Nb_{16}Co_6$	3.517	4.652	57.54	-157.612
$Zr_{78}Nb_{15}Co_7$	3.145	5.503	54.43	-199.412
$Zr_{78}Nb_{14}Co_8$	3.199	5.263	53.86	-248.212
$Zr_{78}Nb_{13}Co_9$	3.222	5.203	54.01	-284.513

#### 4.4.7. Overview of the investigated systems

Heats of formation for the Zr-Nb system at numerous at. % Co addition for (A)  $Zr_{99}Nb_{1-x}Co_x$ , (B)  $Zr_{98.8}Nb_{1.2-x}Co_x$ , (C)  $Zr_{98.1}Nb_{1.9-x}Co_x$ , (D)  $Zr_{97.5}Nb_{2.5-x}Co_x$ , (E)  $Zr_{97}Nb_{3-x}Co_x$  and (F)  $Zr_{78}Nb_{22-x}Co_x$  systems are shown in Figure 4.5. The figures are used to show the thermodynamic stability of the systems graphically by extrapolating linearly with the x-axis and the y-axis. Most of the systems are thermodynamically stable at lower Co content. We have extrapolated linearly from the graph of the  $Zr_{99}Nb_{1-x}Co_x$  (Figure 4.5 A) system which indicated that a  $Zr_{99}Nb_{0.9}Co_{0.1}$  alloy system is thermodynamically stable. This provided a prediction that a smaller addition up to 0.1 at. % Co is favourable, and above this concentration, the structure is unstable ( $\Delta H_f > 0$ ).

Again, from the graph of the  $Zr_{98.8}Nb_{1.2-x}Co_x$  alloy system (Figure 4.5 B), it is observed that the  $Zr_{98.8}Nb_{0.9}Co_{0.1}$  is thermodynamically stable with 0.1 at. % Co being favourable. Furthermore, the  $Zr_{98.1}Nb_{1.7}Co_{0.2}$  (Figure 4.5 C) system is thermodynamically stable up to 0.2 at. % Co addition. Interestingly, Figure 4.5 D and E, show a parabolic trend, with stability ( $\Delta H < 0$ ) being observed at lower and higher compositions for both systems and the structures are unfavourable midway at composition range of  $(0.3 \leq x \leq 2)$ . It is observed that  $Zr_{97.5}Nb_{2.5-x}Co_x$  system (Figure 4.5 D) is favourable (below 0.35 at. % Co and above 2 at. % Co); while  $Zr_{97}Nb_{3-x}Co_x$  system (Figure 4.5 E) is stable (below 0.4 at. % Co and above 2 at. % Co)

Lastly, Figure 4.5 F reveals that from 1 to 2 at. % Co additions, the structure yielded lower energies, suggesting thermodynamic stability. However, as Co was increased, the structure gave more negative values (thermodynamically stable) as shown in Figure 4.5 F [104].

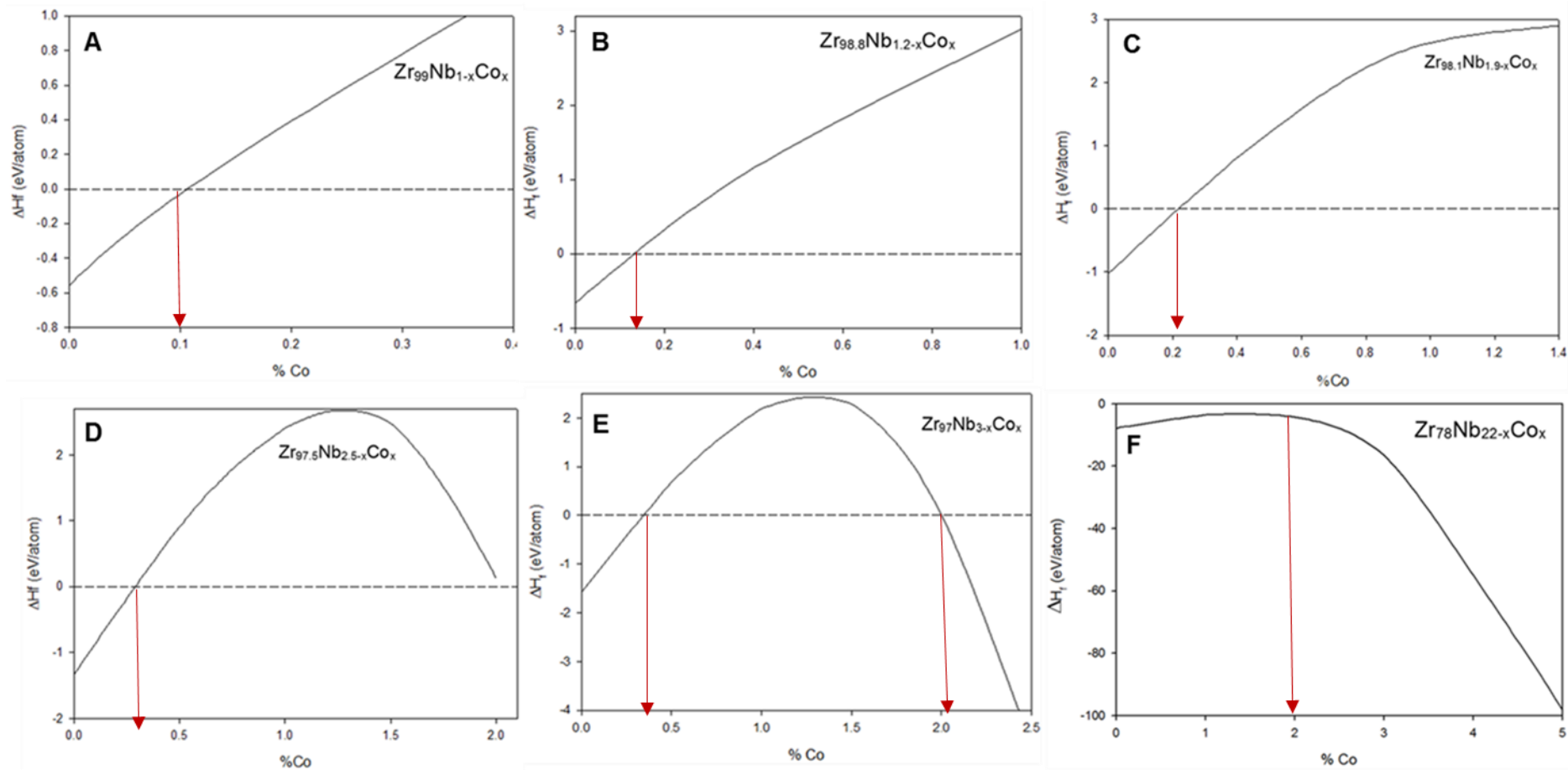


Figure 4.5. Heats of formation for the Zr-Nb system at numerous at. % Co addition for (A)  $Zr_{99}Nb_{1-x}Co_x$ , (B)  $Zr_{98.8}Nb_{1.2-x}Co_x$ , (C)  $Zr_{98.1}Nb_{1.9-x}Co_x$ , (D)  $Zr_{97.5}Nb_{2.5-x}Co_x$ , (E)  $Zr_{97}Nb_{3-x}Co_x$  and (F)  $Zr_{78}Nb_{22-x}Co_x$  systems. The figures are used to estimate thermodynamically stable systems graphically by extrapolating linearly with the x-axis and the y-axis.

# CHAPTER 5

## 5. Mechanical and Electronic Properties

In this chapter, we discuss the electronic and mechanical properties of Zr-Nb and Zr-Nb-Co alloys. Their mechanical stability will be deduced from the elastic constants ( $C_{11}$ ,  $C_{12}$ ,  $C_{44}$  and  $C'$ ) and the ratio of bulk over shear moduli plots with increased Co concentration. Moreover, the electronic stability will be analysed from the density of states plots by analysing the trends near Fermi energy with regard to the effect of Co addition.

### 5.1. Overview of elastic properties.

The elastic constants ( $C_{ij}$ ) determine the response of the crystal to external forces, as characterized by the bulk modulus, shear modulus, Young's modulus and Poisson's ratio and so play an important role in determining the strength of material system [105].

In general, most material systems are elastic to some degree, thus the knowledge of elasticity, deformation or strength is crucial to understand their behaviour. Also, the elastic constants can be used to check the phase stability of material at different concentrations [106, 107]. Since metals and alloys have the regular ordering of atoms/ions that extends through the material, then looking at the elastic constants we can predict the strength of the investigated structures in the  $\alpha$ -Zr, binary Zr-Nb and ternary Zr-Nb-Co alloys.

### 5.2. Elastic properties

In this section, we discuss the elastic properties of Zr, Zr-Nb and Zr-Nb-Co systems to determine their mechanical stabilities. This is done by investigating the effect of

small Co additions on various Zr-Nb-X structures. The Pugh's [108] ratio was also calculated to characterize the ductility and brittleness of the Zr-Nb-Co structures. According to the brittle or ductility criterion, if the B/G ratio is greater or less than the critical value of 1.75 the structure is considered to be ductile or brittle, respectively. We give a detailed discussion on the findings of the investigated structures in the following sections.

### 5.3. Mechanical stability

A smaller addition of Co content is crucial for the development of Zr-Nb alloys for improved industrial applications. In this section we evaluated the elastic stability for both binary and ternary compounds at selected concentrations: binary systems  $Zr_{99}Nb_1$ ,  $Zr_{98.8}Nb_{1.2}$ ,  $Zr_{98.1}Nb_{1.9}$ ,  $Zr_{97.5}Nb_{1.5}$ ,  $Zr_{97}Nb_3$  and  $Zr_{78}Nb_{22}$  while ternary systems are  $Zr_{99}Nb_{1-x}Co_x$ ,  $Zr_{98.8}Nb_{1.2-x}Co_x$ ,  $Zr_{98.1}Nb_{1.9-x}Co_x$ ,  $Zr_{97.5}Nb_{1.5-x}Co_x$  and  $Zr_{78}Nb_{22-x}Co_x$ . These compositions have been reported to have good properties for nuclear and industrial applications.

Note that, the elastic constants depend on the type of lattice *i.e.* for cubic, tetragonal, orthorhombic and monoclinic crystals, there are three ( $C_{11}$ ,  $C_{12}$ ,  $C_{44}$ ), six ( $C_{11}$ ,  $C_{12}$ ,  $C_{13}$ ,  $C_{33}$ ,  $C_{44}$ ,  $C_{66}$ ), nine ( $C_{11}$ ,  $C_{22}$ ,  $C_{33}$ ,  $C_{12}$ ,  $C_{13}$ ,  $C_{23}$ ,  $C_{44}$ ,  $C_{55}$ ,  $C_{66}$ ) and thirteen ( $C_{11}$ ,  $C_{22}$ ,  $C_{33}$ ,  $C_{12}$ ,  $C_{13}$ ,  $C_{23}$ ,  $C_{44}$ ,  $C_{55}$ ,  $C_{66}$ ,  $C_{15}$ ,  $C_{25}$ ,  $C_{35}$ ,  $C_{46}$ ) independent elastic constants, respectively [109]. To evaluate the stability systematically, the symmetry of the structures is unchanged from binary to ternary. We consider mainly the three independent elastic constants ( $C_{11}$ ,  $C_{12}$  and  $C_{44}$ ) and the shear moduli to describe the mechanical stability for the cubic system. The mechanical stability criteria of a cubic lattice as described elsewhere [109] is given as:

$$C_{44} > 0, \tag{5.1}$$

$$C_{11} > |C_{12}|, \quad (5.2)$$

$$C_{11} + 2C_{12} > 0, \quad (5.3)$$

and those for hexagonal crystals are:

$$C_{44} > 0, C_{66} > 0, C_{11} > |C_{12}| \text{ and } C_{11} + C_{12} - \frac{2C_{13}}{C_{33}} > 0. \quad (5.4)$$

The positive shear moduli ( $C' > 0$ ) indicates the mechanical stability of the crystal, otherwise, it is unstable. If all independent elastic constants are positive then our structure is said to be mechanically stable.

The literature findings indicate that using the elastic constants of a single crystal we can calculate the isotropic elastic moduli of polycrystal using the Voight [110], Reuss [111] and Hill [112] approximations. The Voight approximation gives the upper bound of elastic moduli, while the Reuss approximation gives the lower bound. The Hill approximation is the arithmetic average of the upper and lower bound.

Now for hexagonal polycrystal, in our case  $\alpha$ -Zr, the bulk modulus  $B$  and shear modulus  $G$  are given by Voight, Reuss and Hill approximations thus:

$$B_V = \frac{2(C_{11} + C_{12}) + 4C_{13} + C_{33}}{9}, \quad (5.5)$$

$$G_V = \frac{1}{30}(C_{11} + C_{12} + 2C_{33} - 4C_{13} + 12C_{44} + 12C_{66}), \quad (5.6)$$

$$B_R = \frac{C_{33}(C_{11} + C_{12}) - 2C_{13}^2}{C_{11} + C_{12} + 2C_{33} - 4C_{13}}, \quad (5.7)$$

$$G_R = \frac{5}{2} \frac{C_{44} C_{66} [C_{33}(C_{11} + C_{12}) - 2C_{13}^2]}{3B_V C_{44} C_{66} + (C_{44} + C_{66})[C_{33}(C_{11} + C_{12}) - 2C_{13}^2]}, \quad (5.8)$$

$$B_H = \frac{B_V + B_R}{2}, \quad (5.9)$$



$$G_H = \frac{G_V + G_R}{2}, \quad (5.10)$$

Using the bulk and shear moduli, Young's modulus  $E$  and Poisson's ratio  $\nu$  can be obtained by:

$$E = \frac{9BG}{3B+G}, \quad (5.11)$$

and

$$\nu = \frac{3B-2G}{2(3B+G)}. \quad (5.12)$$

### 5.3.1. Zr<sub>99</sub>Nb<sub>1-x</sub>Co<sub>x</sub>

Now, we evaluate the effect of Co addition at different composition range for binary and ternary systems, guided by previous work. Firstly, the effect of small Co additions ( $0 \leq x \leq 1$ ) on the elastic constants ( $C_{11}$ ,  $C_{12}$ ,  $C_{44}$  and  $C'$ ) for the Zr<sub>99</sub>Nb<sub>1.0-x</sub>Co<sub>x</sub> system are evaluated and the results are plotted in Figure 5.1 (A) and summarised in Table 5.1. The Zr<sub>99</sub>Nb<sub>1.0-x</sub>Co<sub>x</sub> system is mechanically stable since all elastic moduli are positive within this concentration range. This is observed for Zr<sub>99</sub>Nb<sub>0.8</sub>Co<sub>0.2</sub> and Zr<sub>99</sub>Nb<sub>0.2</sub>Co<sub>0.8</sub> structures as shown in Table 5.1, which implies that the atomic percent Co additions in this concentration range ( $0 \leq x \leq 1$ ) enhances the stability of Zr<sub>99</sub>Nb<sub>1</sub> system.

We further observe that from Figure 5.1 (B), the Zr<sub>99</sub>Nb<sub>1.0-x</sub>Co<sub>x</sub> system is found to be ductile with  $B/G > 1.75$ . Moreover, a gentle slope is noticed which means that the Zr<sub>99</sub>Nb<sub>1-x</sub>Co<sub>x</sub> system becomes highly ductile as the Co concentration increases in the system.

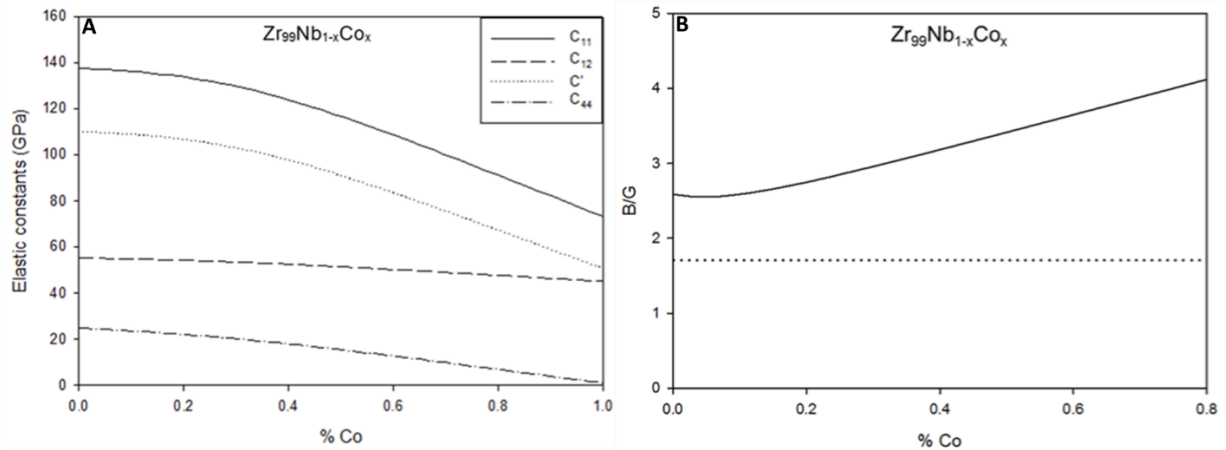


**Figure 5.1.** The elastic constants against alloying element content (% Co) in A and B/G against alloying element content (% Co) in B for the  $Zr_{99}Nb_{1-x}Co_x$  system.

**Table 5.1.** Lattice parameters and the elastic constants for the  $Zr_{99}Nb_{1.0-x}Co_x$  system.

$Zr_{99}Nb_{1.0-x}Co_x$ system	a (Å)	c (Å)	$C_{11}$ (GPa)	$C_{12}$ (GPa)	$C_{44}$ (GPa)	$C'$ (GPa)
$Zr_{99}Nb_{1.0}$	3.270	5.119	137.9	55.23	24.73	110.3
$Zr_{99}Nb_{0.8}Co_{0.2}$	3.260	5.120	131.8	53.95	21.44	104.9
$Zr_{99}Nb_{0.2}Co_{0.8}$	3.226	5.141	92.97	47.07	8.064	69.43

### 5.3.2. $Zr_{98.8}Nb_{1.2-x}Co_x$

We further investigate a slight increase in the atomic percentage of Nb for the  $Zr_{98.8}Nb_{1.2-x}Co_x$  system, to evaluate the effect of Co additions on the Zr-Nb system with decreasing Zr content and increasing Nb content. The effect of adding Co at this stage is done at a concentration range of ( $0 \leq x \leq 1.2$ ). The findings are shown in Figure 5.2 (A) and Table 5.2, we established that all elastic moduli are positive which shows a strong condition for mechanical stability. Thus, we have observed that the additions of Co in this concentration range ( $0 \leq x \leq 1.2$ ) gave mechanically stable  $Zr_{98.8}Nb_{1.2-x}Co_x$  systems.

The brittleness or ductility of the structure discussed above was determined, this is shown in figure 5.2 (B) where the system is found to be ductile since B/G ratio is greater than 1.75. An increasing graph is observed for  $Zr_{98.8}Nb_{1.2-x}Co_x$ , indicating that ductility is enhanced and this is due to increasing Co content.

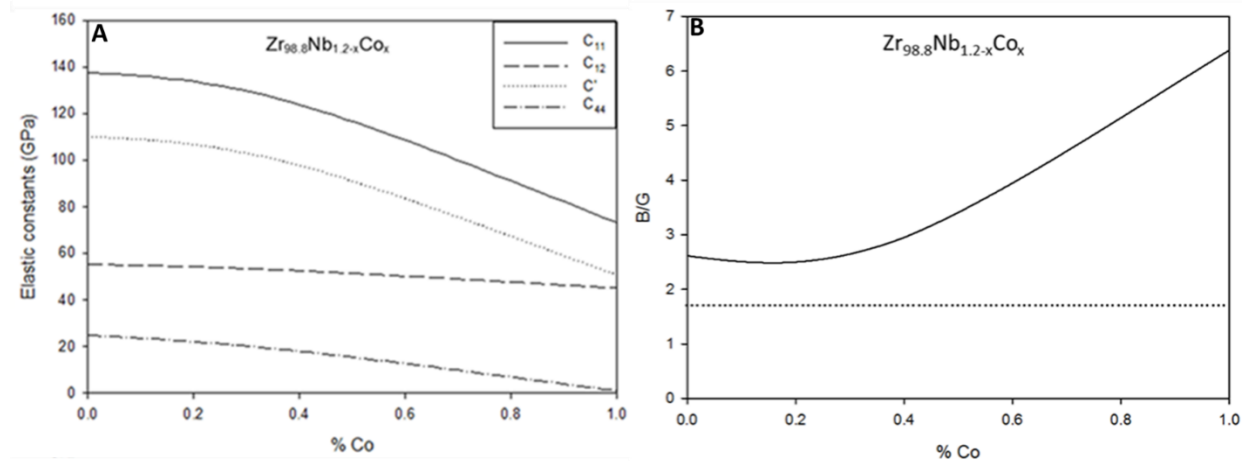


Figure 5.2. The elastic constants against alloying element content (% Co) in A and B/G against alloying element content (% Co) in B for the  $Zr_{98.8}Nb_{1.2-x}Co_x$  system.

Table 5.2. Lattice parameters and the elastic constants for the  $Zr_{98.8}Nb_{1.2-x}Co_x$  system.

$Zr_{98.8}Nb_{1.2-x}Co_x$ system	a (Å)	c (Å)	$C_{11}$ (GPa)	$C_{12}$ (GPa)	$C_{44}$ (GPa)	$C'$ (GPa)
$Zr_{98.8}Nb_{1.2}$	3.270	5.120	137.7	55.19	24.73	110.1
$Zr_{98.8}Nb_{0.8}Co_{0.4}$	3.249	5.123	123.9	52.45	17.89	97.71
$Zr_{98.8}Nb_{0.2}Co_{1.0}$	3.194	5.213	73.12	45.06	0.888	50.59

### 5.3.3. $Zr_{98.1}Nb_{1.9-x}Co_x$

Furthermore, we observed a similar trend for the  $Zr_{98.1}Nb_{1.9-x}Co_x$  structure which is mechanically stable since all the elastic moduli are positive. The  $Zr_{98.1}Nb_{1.9-x}Co_x$  structure is found to be mechanically stable in the range ( $0 \leq x \leq 1.9$ ) as shown in Figure 5.3 (A) and Table 5.3.

Again we observed that the  $Zr_{98.1}Nb_{1.9-x}Co_x$  system is ductile up to 1.1 at. % Co with B/G greater than 1.75 and above 1.1 at. % Co the system becomes brittle with B/G being less than 1.75 which is shown in Figure 5.2 (B). These findings limit the alloying element concentration to within 1.0 at. % Co at this composition.

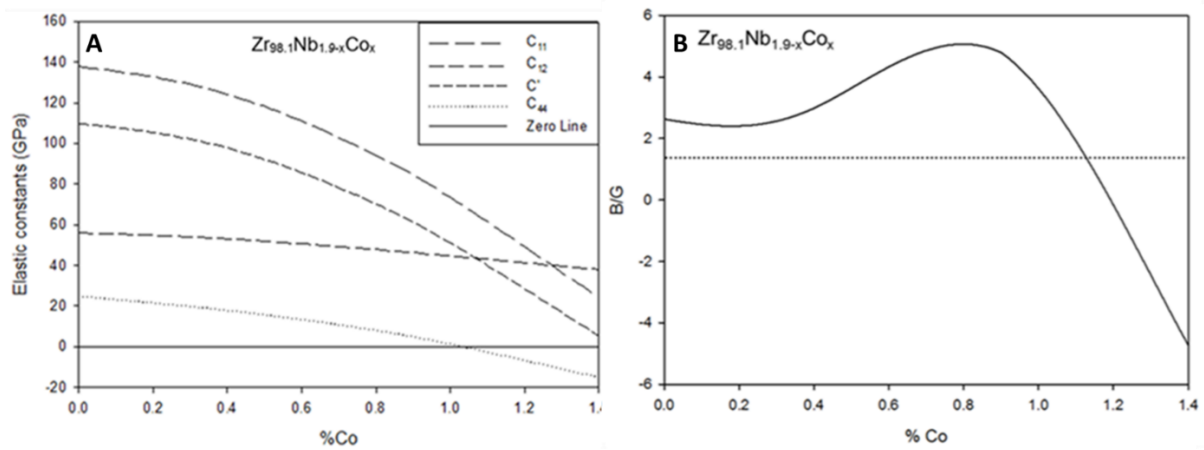


Figure 5.3. The elastic constants against alloying element content (% Co) in A and B/G against alloying element content (% Co) in B for the  $Zr_{98.1}Nb_{1.9-x}Co_x$  system.

Table 5.3. Lattice parameters and the elastic constants for the  $Zr_{98.1}Nb_{1.9-x}Co_x$  system.

$Zr_{98.1}Nb_{1.9-x}Co_x$ system	a (Å)	c (Å)	$C_{11}$ (GPa)	$C_{12}$ (GPa)	$C_{44}$ (GPa)	$C'$ (GPa)
$Zr_{98.1}Nb_{1.9}$	3.268	5.115	137.6	55.88	24.75	109.8
$Zr_{98.1}Nb_{1.5}Co_{0.4}$	3.246	5.121	124.2	52.96	17.74	97.72
$Zr_{98.1}Nb_{1.0}Co_{0.9}$	3.211	5.164	84.31	46.22	4.831	61.20
$Zr_{98.1}Nb_{0.5}Co_{1.4}$	2.918	6.147	24.05	37.85	-15.25	5.123

#### 5.3.4. $Zr_{97.5}Nb_{2.5-x}Co_x$

Now, we consider the  $Zr_{97.5}Nb_{2.5-x}Co_x$  system, in particular at 0.5 at. % Co (as shown in Figure 5.4 (A)), all elastic moduli are negative. However, when Co content is increased further all the elastic moduli becomes positive at about 1.0 at. % which suggests that  $Zr_{97.5}Nb_{1.7}Co_{0.8}$  and  $Zr_{97.5}Nb_{1.5}Co_{1.0}$  systems are mechanically stable. We further observed a condition of mechanical instability at around 1.2 at. % Co with

$C_{44}$  becoming negative while at about 2.5 at. % Co we see that all elastic moduli are more negative. The  $C_{ij}$  decreases drastically below 0.5 at. % Co (an instability is observed), however above this concentration an increasing trend is observed the resulting structure is stable at about 0.7 at. % Co. The  $C'$ , however, remains negative from 1 at. % Co (condition of instability).

The ductility of the  $Zr_{97.5}Nb_{2.5-x}Co_x$  system is predicted to be within ( $0 \leq x \leq 0.9$ ) and ( $1.0 \leq x \leq 1.5$ ) atomic percentages of Co with B/G values being greater than 1.75 (see Figure 5.4 (B)). The structure indicates good ductility between 1.3 and 1.4 at. % Co content then a sudden drop is observed as the concentration is increased above 1.5 Co content. Then the structure becomes brittle above 1.5 at. % Co and shows fluctuation from being ductile to brittle which limits the alloying element and the concentration above 1.5 to be unreliable.

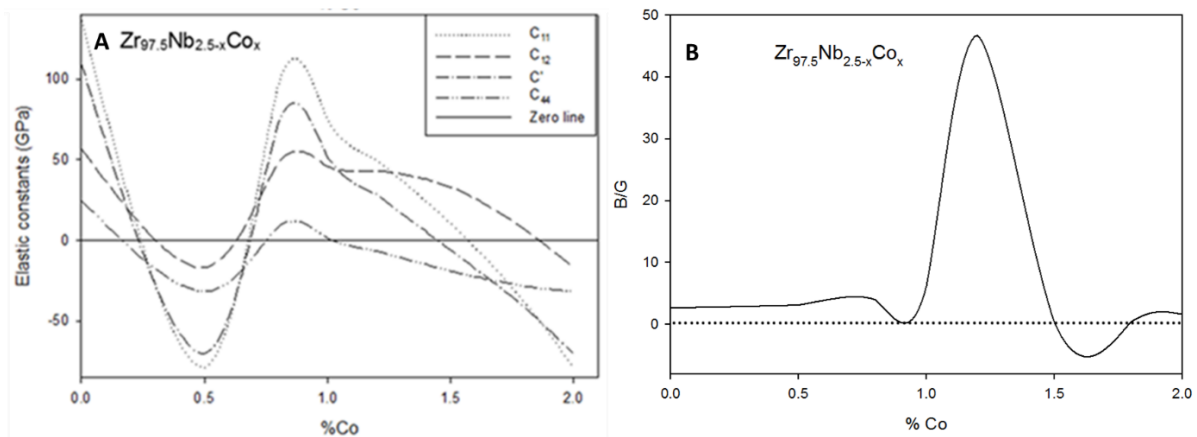


**Figure 5.4.** The elastic constants against alloying element content (% Co) in A and B/G against alloying element content (% Co) in B for  $Zr_{97.5}Nb_{2.5-x}Co_x$  system.

**Table 5.4. Lattice parameters and the elastic constants for  $Zr_{97.5}Nb_{2.5-x}Co_x$  system.**

<b><math>Zr_{97.5}Nb_{2.5-x}Co_x</math> system</b>	<b>a</b> <b>(Å)</b>	<b>c</b> <b>(Å)</b>	<b><math>C_{11}</math></b> <b>(GPa)</b>	<b><math>C_{12}</math></b> <b>(GPa)</b>	<b><math>C_{44}</math></b> <b>(GPa)</b>	<b><math>C'</math></b> <b>(GPa)</b>
$Zr_{97.5}Nb_{2.5}$	3.267	5.112	138.5	57.12	24.80	110.0
$Zr_{97.5}Nb_{2.0}Co_{0.5}$	3.239	5.121	-78.97	-17.03	-31.88	-70.45
$Zr_{97.5}Nb_{1.7}Co_{0.8}$	3.223	5.135	96.08	47.69	8.331	72.24
$Zr_{97.5}Nb_{1.5}Co_{1.0}$	3.195	5.197	74.56	45.55	1.232	51.79
$Zr_{97.5}Nb_{1.3}Co_{1.2}$	2.953	5.983	49.79	43.09	-6.820	28.24
$Zr_{97.5}Nb_{1.0}Co_{1.5}$	2.911	6.133	10.47	33.02	-19.15	-6.034
$Zr_{97.5}Nb_{0.7}Co_{1.8}$	2.796	6.440	-38.34	6.688	-28.43	-41.68
$Zr_{97.5}Nb_{0.5}Co_{2.0}$	3.395	4.789	-78.97	-17.03	-31.88	-70.45

### 5.3.5. $Zr_{97}Nb_{3-x}Co_x$

We further analyse the mechanical stability behaviour of the  $Zr_{97}Nb_{3-x}Co_x$  structure, as depicted in Figure 5.5 (A) and data is listed in table 5.5. We have observed that all elastic moduli:  $C_{11}$ ,  $C_{12}$ ,  $C_{44}$  and  $C'$  are positive up to 1.0 atomic percent Co, this finding suggests that the  $Zr_{97}Nb_{3-x}Co_x$  structure is mechanically stable at about 1.0 at. % Co. Interestingly, we observed that  $C_{44}$  becomes softer above 1.0 atomic percent followed by  $C'$ ,  $C_{11}$  and  $C_{12}$ , this implies that the structure becomes mechanically unstable above 1.0 atomic percent Co. The softening of  $C'$ ,  $C_{11}$  and  $C_{12}$  is due to  $C_{44}$  becoming more negative above 1.0 atomic percent Co.

Moreover, the  $Zr_{97}Nb_{3-x}Co_x$  system is found to be ductile in this concentration ranges ( $0 < x < 1.25$ ) and ( $2.0 < x < 2.5$ ) since the B/G ratio is greater than 1.75. It is again observed to be less than 1.75 at  $1.25 < x < 2.0$  composition range which shows brittleness (least ductile), this trend is shown in Figure 5.5 (B).

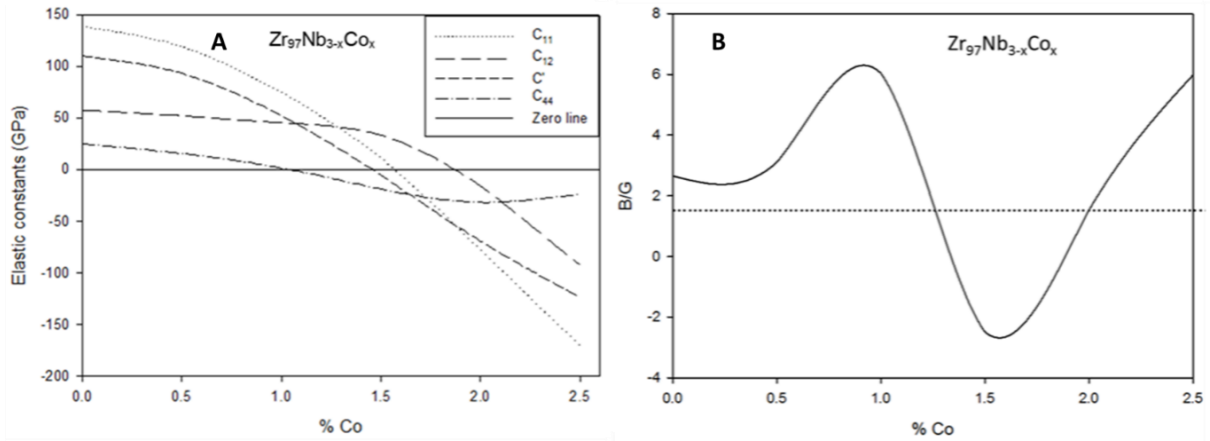


**Figure 5.5.** The elastic constants against alloying element content (% Co) in A and B/G against alloying element content (% Co) in B for the  $Zr_{97.5}Nb_{2.5-x}Co_x$  system.

**Table 5.5.** Lattice parameters and the elastic constants for the  $Zr_{97}Nb_{3-x}Co_x$  system.

$Zr_{97}Nb_{3-x}Co_x$ system	a (Å)	c (Å)	$C_{11}$ (GPa)	$C_{12}$ (GPa)	$C_{44}$ (GPa)	$C'$ (GPa)
$Zr_{97}Nb_3$	3.264	5.110	138.6	57.57	24.84	109.84
$Zr_{97}Nb_{2.5}Co_{0.5}$	3.237	5.120	119.3	52.22	15.54	93.16
$Zr_{97}Nb_{2.0}Co_{1.0}$	3.195	5.192	74.94	45.60	1.344	52.14
$Zr_{97}Nb_{1.5}Co_{1.5}$	2.920	6.150	11.18	33.41	-19.05	-5.527
$Zr_{97}Nb_{1.0}Co_{2.0}$	3.508	5.196	-77.50	-16.20	-31.89	-69.45
$Zr_{97}Nb_{0.5}Co_{2.5}$	4.812	8.058	-170.4	-92.61	-23.99	-124.05

### 5.3.6. $Zr_{78}Nb_{22-x}Co_x$

Lastly, the  $Zr_{78}Nb_{22-x}Co_x$  system is discussed. The system is elastically stable at very low Co contents (less than 1 atomic percent) since all elastic moduli are positive. An interesting trend is observed for 1 – 2 atomic percent Co, where the structure is stable ( $C_{ij}$  positive) to  $C'$ , with  $C_{44}$  being slightly negative up to 3 at. % Co (condition of instability). However, the  $C'$  becomes softer (highly unstable) above 2 to 3 atomic percent Co. This is due to the  $C_{11}$  becoming more negative, which implies that the alloy is mechanically stable from 0 to 2 atomic percent Co. These findings are shown in Figure 5.6 (A) and Table 5.6.

Now, from Figure 5.6 (B) we note that the ratio B/G gave values less than 1.75 at 2 – 3 atomic percent Co, thus indicating brittleness, whereas values above 1.75 were found at concentrations below 2 atomic percent Co (condition of ductility). Furthermore, the structure is again predicted to be ductile at concentrations above 3 atomic percent Co. This suggests that a good alloy system with the desired application may be possible at a concentration below 2 at. % Co, for the  $Zr_{78}Nb_{22-x}Co_x$  system.

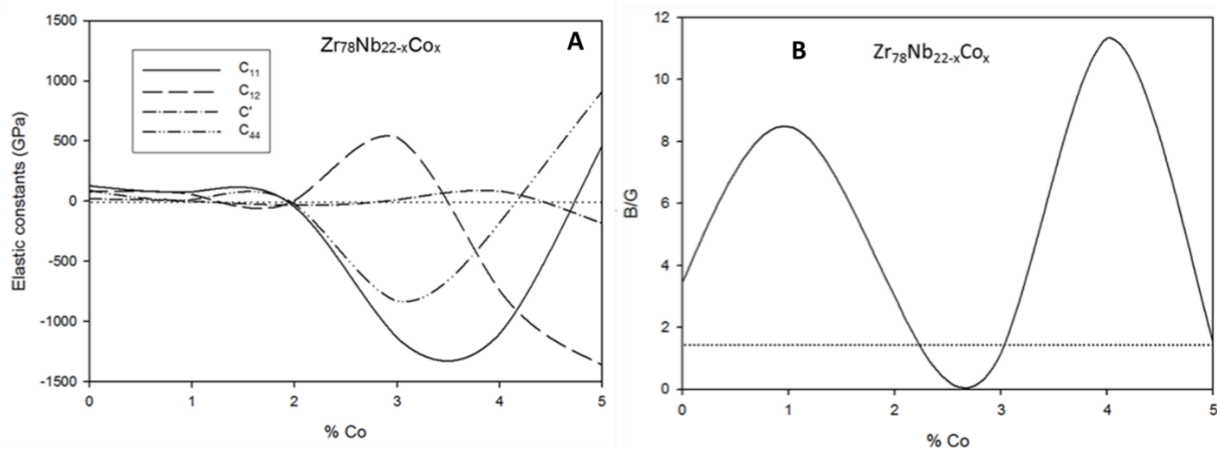


**Figure 5.6.** The elastic constants against alloying element content (% Co) in A and B/G against alloying element content (% Co) in B for the  $Zr_{78}Nb_{22-x}Co_x$  system.

**Table 5.6.** Lattice parameters and elastic constants for the  $Zr_{78}Nb_{22-x}Co_x$  system (effect of Co addition).

$Zr_{78}Nb_{22-x}Co_x$ system	a (Å)	c (Å)	$C_{11}$ (GPa)	$C_{12}$ (GPa)	$C_{44}$ (GPa)	$C'$ (GPa)
$Zr_{78}Nb_{22}$	3.151	5.103	127.3	78.08	17.95	0.600
$Zr_{78}Nb_{21}Co_1$	3.121	5.154	77.08	56.48	-2.843	-1.017
$Zr_{78}Nb_{20}Co_2$	3.851	3.815	-45.98	3.962	-33.91	0.018
$Zr_{78}Nb_{19}Co_3$	3.050	4.833	-1136.1	530.1	11.70	-0.892
$Zr_{78}Nb_{18}Co_4$	3.270	5.158	-1103.8	-742.9	82.85	-0.944
$Zr_{78}Nb_{17}Co_5$	3.460	4.799	459.6	-1362.7	-185.3	-0.670



### 5.3.7. Overview of the elastic properties

Figure 5.7 (A, B, C, D, E and F) compares the trends on the effect of Co addition on investigated systems (see section 5.3.1-5.3.6). Now, Figure 5.7 (A) shows that for the  $Zr_{99}Nb_{1-x}Co_x$  system the elastic constants ( $C_{11}$ ,  $C_{12}$ ,  $C_{44}$  and  $C'$ ) are all positive within the  $0 < x < 1$  at. % Co region, thus they are mechanically favourable. The  $Zr_{98.8}Nb_{1.2-x}Co_x$  system is also investigated, a slight increase in Co content is introduced in Figure 5.7 (B), it is seen that the  $C_{44}$  approaches negative faster than the  $C_{11}$ ,  $C_{12}$  and  $C'$ , this indicates that the structure becomes unstable. Furthermore, the Co content is increased to investigate its effect on  $Zr_{98.1}Nb_{1.9-x}Co_x$  system (see figure 5.7 C), a trend observed in Figure 5.7 (B) continues because the  $C_{44}$  is negative above 1.0 at. % Co content. Moreover,  $C_{11}$  and  $C_{12}$  show a rapid decrease towards the zero line which indicates the structure becomes mechanically unstable above 1.0 at. % Co content.

Interestingly, in Figure 5.7 (D) for  $Zr_{97.5}Nb_{2.5-x}Co_x$  system, with additions in the range  $0 \leq x \leq 2.0$  at. % Co content, the elastic moduli becomes negative above 0.3 at. % Co content (system becomes unstable) then becomes positive at 1.0 at. % Co content then remains negative (unstable). On the other hand, the structure stabilizes at 0.3 and 1.0 at. % Co content. The  $Zr_{97}Nb_{3-x}Co_x$  system as shown in figure 5.7 (E) indicates stability in between  $0 \leq x \leq 1.0$  at. % Co addition with all the elastic moduli being positive and they become negative above 1.0 at. % Co content. Lastly, in figure 5.7 (F) the  $Zr_{78}Nb_{22-x}Co_x$  system is mechanically stable to within 2 at. % Co addition. Now, at around 1.2 at. % Co content, the  $C_{12}$  becomes negative hence the structure becomes unstable.

Similarly, in Figure 5.8 (A, B, C, D, E and F) we observe a pattern for the B/G ratio as the Co content is increased. Figure 5.8 (A) shows the  $Zr_{99}Nb_{1-x}Co_x$  structure is ductile within  $0 \leq x \leq 1.0$  at. % Co addition. Now the  $Zr_{98.8}Nb_{1.2-x}Co_x$  structure indicates good ductility within  $0 \leq x \leq 1.2$  at. % Co content (see Figure 5.8 (B)). Moreover, for the  $Zr_{98.1}Nb_{1.9-x}Co_x$  system, it becomes ductile below 1.1 at. % Co content otherwise brittle. Furthermore, the  $Zr_{97.5}Nb_{2.5-x}Co_x$  system shows poor ductility between  $0 \leq x \leq 1.0$  at. % Co content and good ductility at 1.25 at. % Co addition and becomes brittle above 1.5 at. % Co addition in figure 5.8 (D).

The  $Zr_{97}Nb_{3-x}Co_x$  system becomes ductile within  $0 \leq x \leq 1.0$  at. % Co content (see Figure 5.8 E) and brittle above 1.25 at. % Co content. Lastly, the  $Zr_{78}Nb_{22-x}Co_x$  system indicates that above 1.0 at. % Co content the ductility reduces around 2 at. % Co content, the structure becomes brittle to within  $2 \leq x \leq 3$  at. % Co content (see figure 5.8 F).

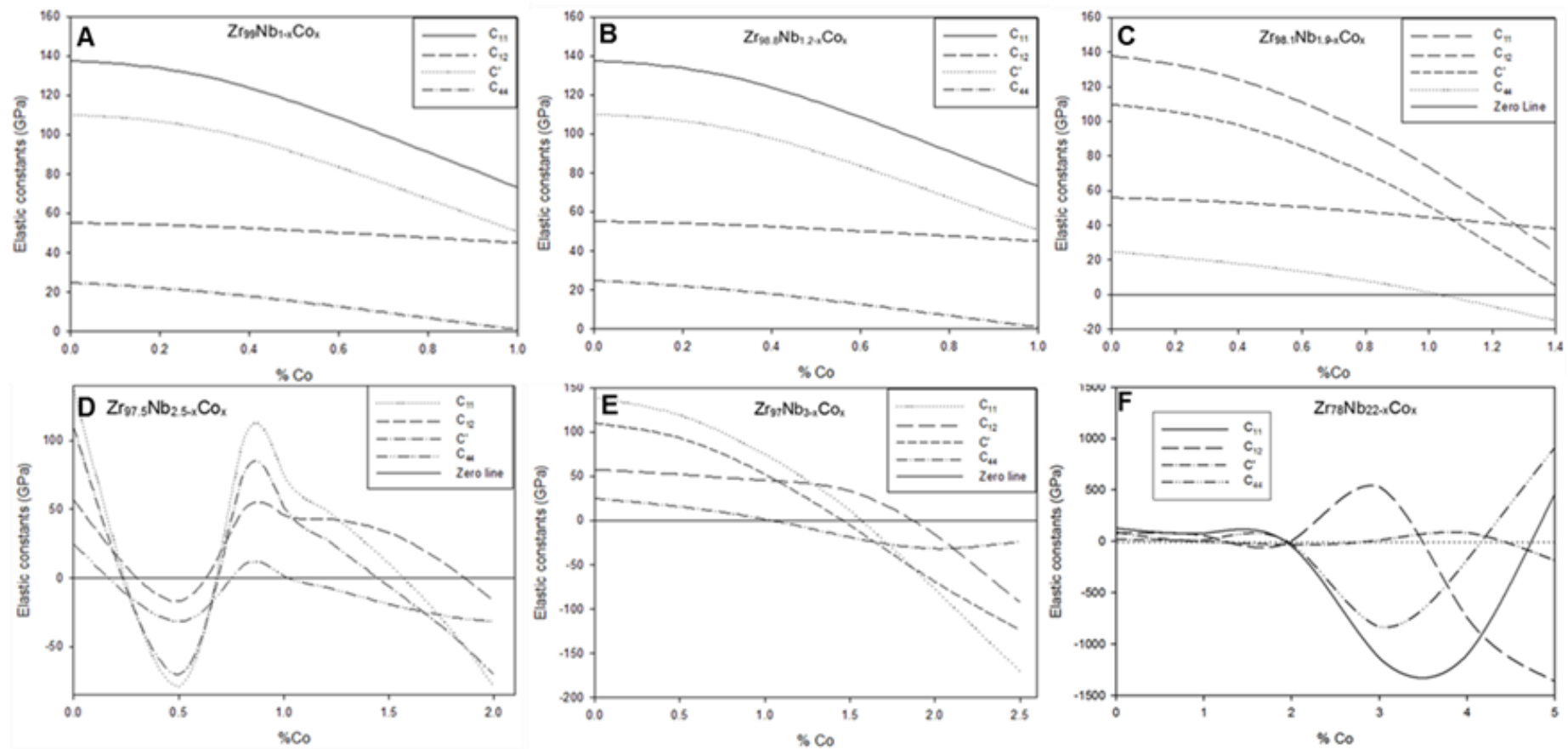


Figure 5.7. Elastic constants versus atomic percentage cobalt in the A) Zr<sub>99</sub>Nb<sub>1-x</sub>Co<sub>x</sub>, (B) Zr<sub>98.8</sub>Nb<sub>1.2-x</sub>Co<sub>x</sub>, (C) Zr<sub>98.1</sub>Nb<sub>1.9-x</sub>Co<sub>x</sub>, (D) Zr<sub>97.5</sub>Nb<sub>2.5-x</sub>Co<sub>x</sub>, (E) Zr<sub>97</sub>Nb<sub>3-x</sub>Co<sub>x</sub> and (F) Zr<sub>78</sub>Nb<sub>22-x</sub>Co<sub>x</sub> systems at various concentrations.

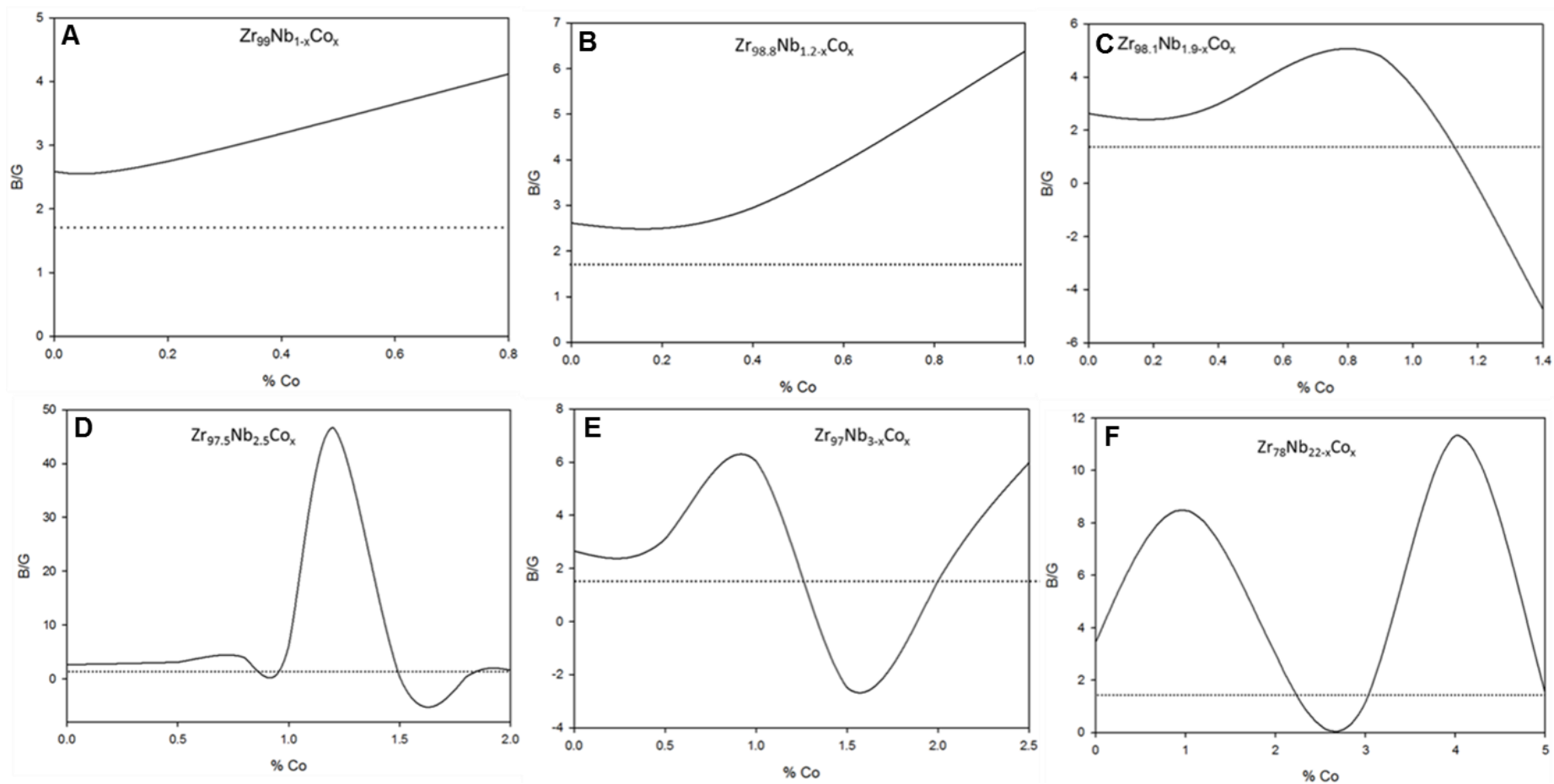


Figure 5.8. Ratio of bulk and shear modulus against percentage cobalt in the competing phases of A)  $Zr_{99}Nb_{1-x}Co_x$ , (B)  $Zr_{98.8}Nb_{1.2-x}Co_x$ , (C)  $Zr_{98.1}Nb_{1.9-x}Co_x$ , (D)  $Zr_{97.5}Nb_{2.5-x}Co_x$ , (E)  $Zr_{97}Nb_{3-x}Co_x$  and (F)  $Zr_{78}Nb_{22-x}Co_x$  systems. The dotted line indicates the  $B/G = 1.75$  reference as a visual guide. A  $B/G$  ratio greater or less than 1.75 is indicative of ductility or brittleness respectively

#### **5.4. Overview of the density of states**

The electronic density of states (DOS) of a system describes the number of states at each energy level that is available to be filled. A high DOS at a specific energy level means there are many states available for occupation. A DOS of zero signifies there are no states available for occupation at that given energy level [113]. In this section, the idea is to find an electronically stable structure by judging the one with the lowest number of DOS at the Fermi level and also determines how the states are affected by alloying with Co. This analysis has been used elsewhere [114].

#### **5.5. The density of states for Zr-Nb and Zr-Nb-Co alloy**

We consider the electronic density of states (DOS) for binary Zr-Nb and ternary Zr-Nb-Co systems. The ternaries for the Zr-Nb-Co system were determined by varying the concentration of cobalt in the Zr-Nb alloys. Structures with the highest and lowest DOS at the Fermi energy ( $E_f$ ) are considered to be the least and most stable respectively. Thus will be viewed with regard to the other competing phases of the Zr-Nb-Co alloy similar argument has been used previously [115, 114].

##### **5.5.1. Electronic stability**

The density of states was calculated to determine the electronic stability of the Zr-Nb-Co systems. This is achieved by evaluating the effect of Co addition with respect to the trend and behaviour of the density of states plots near the  $E_f$ . We observe the trend of the density of states near the Fermi level ( $E - E_f = 0$ ) to establish the electronic stability of the following systems;  $Zr_{99}Nb_{1-x}Co_x$ ,  $Zr_{98.8}Nb_{1.9-x}Co_x$ ,  $Zr_{97.5}Nb_{2.5-x}Co_x$ ,  $Zr_{97}Nb_{3-x}Co_x$  and  $Zr_{78}Nb_{22-x}Co_x$ .

Firstly, in Figure 5.3 (A) we show the DOS plots for the  $Zr_{99}Nb_{1-x}Co_x$  system. Recall that the Zr concentration is kept constant while Nb is reduced with an increase in the Co concentration, (i.e. the substitution of Co for Nb atoms). This substitution results in an increase in tDOS, because Co increases the total number of states. The peaks follow a similar pattern to that of the  $Zr_{99}Nb_1$  system after the Co addition. However, when Co is introduced, the  $Zr_{99}Nb_{0.8}Co_{0.2}$  structure is the most electronically stable as compared to the  $Zr_{99}Nb_{0.2}Co_{0.8}$  structure because the states are slightly lowered at the Fermi energy.

The DOS plots for the  $Zr_{98}Nb_{1.2-x}Co_x$  structure at different concentrations are shown in Figure 5.3 (B). As the concentration of Co is increased the total DOS are observed to increase at both 0.4 and 1 at. % Co. Furthermore, we observed a pseudogap near the Fermi energy for all the systems. The  $Zr_{98.8}Nb_{0.8}Co_{0.4}$  system shows a deep pseudogap (on the left of the fermi level) near the Fermi energy as compared to the  $Zr_{98.8}Nb_{0.2}Co_1$  system thus electronically favourable. It is clear that the states at lowered at the  $E_f$  as the Co content is increased to 1 at. %.

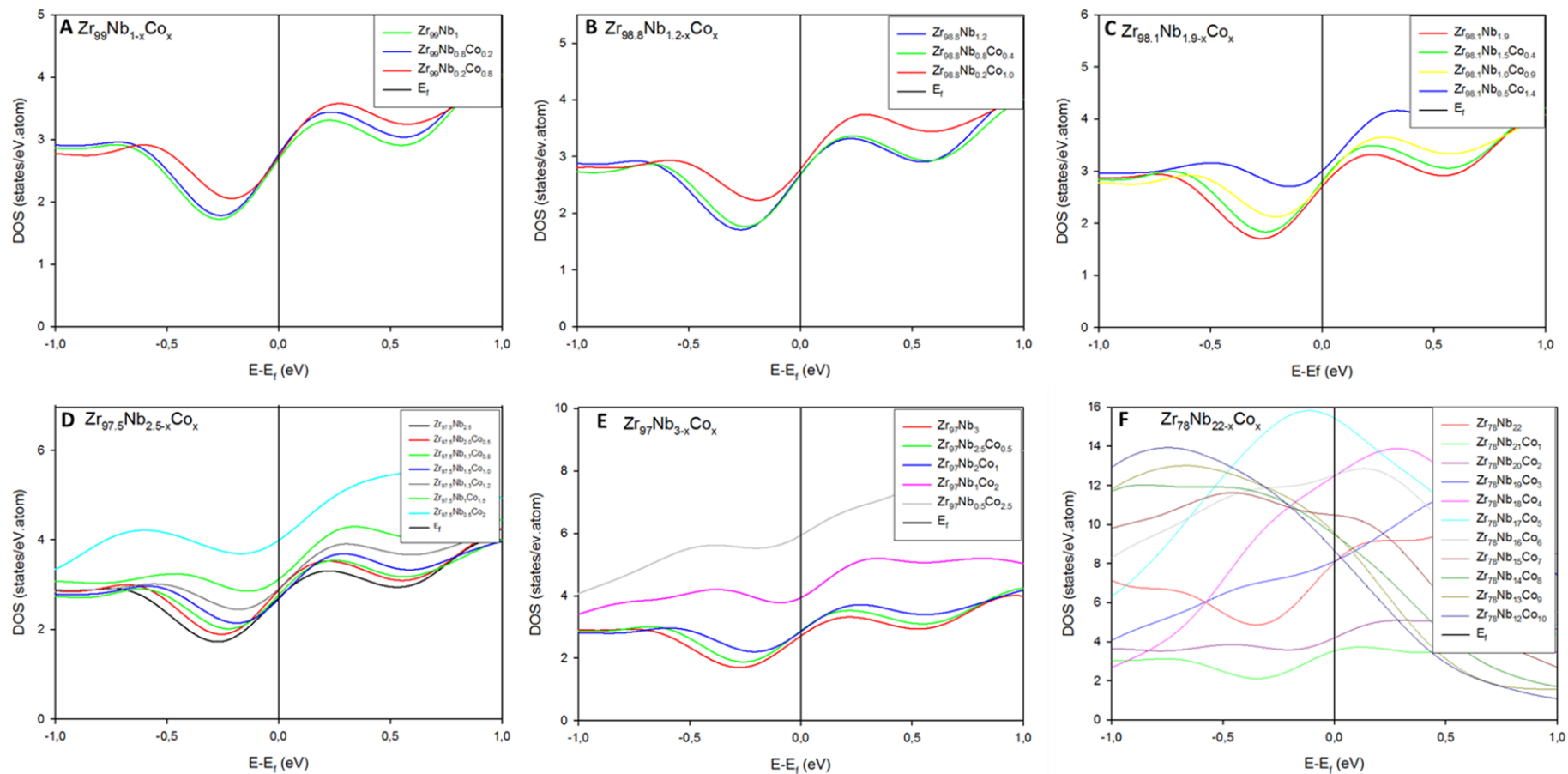
In Figure 5.3 (C), we consider the  $Zr_{98.1}Nb_{1.9-x}Co_x$  system with various Co content addition. Similarly, we observe the pseudogap at about 0.2 eV (left of the Fermi level) a pseudogap with lowered states near the Fermi energy is observed for the  $Zr_{98.1}Nb_{1.5}Co_{0.4}$  system. This analysis suggests that the  $Zr_{98.1}Nb_{1.5}Co_{0.4}$  system is electronically stable as compared to  $Zr_{98.1}Nb_{1.0}Co_{0.9}$  and  $Zr_{98.1}Nb_{0.5}Co_{0.4}$  structures since it displays lower states at  $E_f$ .

Figure 5.3 (D) shows the DOS plot for the  $Zr_{97.5}Nb_{2.5-x}Co_x$  system, we observed that an increase in Co content increase the number of states for the systems near the Fermi energy. The  $Zr_{97.5}Nb_{2.5}$  system shows lowered states near  $E_f$  followed by

$Zr_{97.5}Nb_{2.0}Co_{0.5}$ ,  $Zr_{97.5}Nb_{1.7}Co_{0.8}$ ,  $Zr_{97.5}Nb_{1.5}Co_{1.0}$ ,  $Zr_{97.5}Nb_{1.3}Co_{1.2}$ ,  $Zr_{97.5}Nb_1Co_{1.5}$  and  $Zr_{97}Nb_{0.5}Co_2$  systems respectively. This indicates that a 0.5 at. % Co addition could be considered electronically stable ever since its states are lowered compared to other compositions near the Fermi energy.

In our current discussion, it is clear that the behaviour of DOS depends on the concentration of Zr, Nb and Co. We investigated the  $Zr_{97}Nb_{3-x}Co_x$  system in Figure 5.3 (E) to establish the influence of Co concentration. The Fermi level cuts slightly on the left through the pseudogap which makes the  $Zr_{97}Nb_1Co_2$  structure to be electronically more favourable which is in line with the predicted heats of formation (discussed above). The  $Zr_{97}Nb_{2.5}Co_{0.5}$ ,  $Zr_{97}Nb_2Co_1$ ,  $Zr_{97}Nb_3$  structures appear to be less stable as compared to  $Zr_{97}Nb_1Co_2$  system since they display high DOS at the Fermi energy. The states for the  $Zr_{97}Nb_{2.5}Co_{0.5}$  system are very high as compared to the other systems hence highly unstable. This finding suggests a 2 at. % Co addition is favourable for enhancing the electronic stability of the  $Zr_{97}Nb_{3-x}Co_x$  system.

Lastly, we consider the  $Zr_{78}Nb_{22-x}Co_x$  structure with various Co concentrations (Figure 5.9 F). A deep pseudogap is observed for the  $Zr_{78}Nb_{22}$  structure closer to the Fermi level which guides Co doping. Interestingly, the  $Zr_{78}Nb_{21}Co_1$  and  $Zr_{78}Nb_{20}Co_2$  systems are characterized by a pseudogap (left of  $E_f$ ) and with lower states near Fermi energy at low concentrations. The 1 and 2 at. % Co additions are favourable (electronically stable). These concentrations are found to enhance the stability of the  $Zr_{78}Nb_{22}$  structure. The other systems with high Co concentrations are not favourable judging by the size of peaks near the Fermi energy thus making them highly unstable.



**Figure 5.9.** Comparison of the total density of states (tDOS) for the (A)  $\text{Zr}_{99}\text{Nb}_{1-x}\text{Co}_x$ , (B)  $\text{Zr}_{98.8}\text{Nb}_{1.2-x}\text{Co}_x$ , (C)  $\text{Zr}_{98.1}\text{Nb}_{1.9-x}\text{Co}_x$ , (D)  $\text{Zr}_{97.5}\text{Nb}_{2.5-x}\text{Co}_x$ , (E)  $\text{Zr}_{97}\text{Nb}_{3-x}\text{Co}_x$  and (F)  $\text{Zr}_{78}\text{Nb}_{22-x}\text{Co}_x$  systems. The fermi energy is taken as the energy zero ( $E-E_f = 0$ ).



# Chapter 6

## 6. Molecular dynamics

In this chapter, we discuss the molecular dynamics results for both the binary and ternary systems. In particular, the effect of Co and Sn addition on the Zr-Nb structure. The choice of Sn is based on its ability to enhance the cladding properties for nuclear applications [24]. The Co is also preferred for its large thermal neutron cross-section and its capability for supporting and protecting fissionable material in high-temperature fast reactors [28]. Thus the binding energies, elastic constants and DOS have been calculated at various temperatures to establish an understanding of the effect of Co and Sn ternary alloying.

The study model various atomic concentrations for both Co and Sn; this will allow more precise predictions and understanding of the thermodynamic behaviour of the Zr-Nb-Co and Zr-Nb-Sn systems at various temperature conditions up to 2400K, above the experimental melting temperature of Zr [116].

Recall, the model is represented in Chapter 4, Figure 4.2, showing possible doping mechanism of metals on  $\alpha$ -Zr structure; firstly Nb was introduced to form Zr-Nb solid solution, and then Co or Sn was doped on the Nb sublattice to form Zr-Nb<sub>x-1</sub>-Co<sub>x</sub> or Zr-Nb<sub>x-1</sub>-Sn<sub>x</sub> systems.

### 6.1. Binding energy

In this section, the binding energy is considered to establish at what temperature is the system able to withstand and maintain its symmetry or configuration, i.e. deduce the stability at a certain temperature range. The binding energy was calculated.

The binding energy is determined by the following expression:

$$E_b = E_C - \sum_i x_i E_i, \quad (6.1)$$

where  $E_C$  is the calculated total energy of the compound and  $E_i$  is the calculated total energy of the element in the compound. Note that negative binding energy indicates an energetically favourable system otherwise unstable.

Theoretically, the binding energy is used to check how atoms are bonded to each other in the system, and conventionally to evaluate the stability of a given system. The stability, in this case, is dependent on the temperature and composition of the system [118]. Note that a high binding energy value (more positive) corresponds to the unstable system while a lower value (more negative) corresponds to a stable compound.

Note that, the calculations were performed employing Dmol<sup>3</sup> [117] code. The NVT ensemble was chosen to evaluate the systems at different temperatures. We observe the structural behaviour at any given binding energy and temperature.

In the next section, we examine the dependence of ternary alloying at varied temperatures and different compositions for both Co and Sn doped systems ( $0 \leq x \leq 3$ ).

### 6.1.1. Co and Sn elements at 0 K

Now, we investigate the effect of alloying for 22 at. % Nb and 50 at. % Nb composition, i.e. Zr<sub>78</sub>Nb<sub>22</sub> and Zr<sub>50</sub>Nb<sub>50</sub> systems. In particular, their stability concerning binding energy was evaluated at 0 K. Firstly, the 22 at. % Nb composition gave  $E_b$  of -6.87 eV/atom whereas 50 at. % Nb structure predicted  $E_b$  of -6.78 eV/atom (Table 1). This suggests that increasing the Nb content from 22 to 50 at. % increases the binding energy or reduces the stability of the system (destabilizing).

**Table 6.1** The binding energy [ $E_b$ ] of Co and Sn addition at 0K for  $Zr_{78}Nb_{22-x}X_x$  and  $Zr_{50}Nb_{50-x}X_x$  systems. The result of the binary system is also shown for reference.

Composition (at. %)	$[E_b]$ (eV/atom)		$[E_b]$ (eV/atom)	
	$Zr_{78}Nb_{22-x}X_x$		$Zr_{50}Nb_{50-x}X_x$	
	Sn	Co	Sn	Co
0	-6.87		-6.78	
1	-6.85	-6.86	-6.74	-6.75
2	-6.82	-6.84	-6.69	-6.70
3	-6.78	-6.80	-6.59	-6.65

Secondly, in Table 6.1 the binding energies at 0 K for composition range  $0 \leq x \leq 3$  are reflected. We observed an increase (more negative to less negative) in  $E_b$  with increasing concentration for both Sn and Co. This is confirmed in Figures 6.1 A and B, which show similar increasing trends. It can be noted that the differences in binding energies, depend or are informed by the effect of Nb content in the structure. The results analysis in Table 6.1 and Figure 6.1 shows a slight increase in binding energy as the concentration increases at 0 K. This is observed for both Sn and Co addition in the  $Zr_{78}Nb_{22-x}X_x$  and  $Zr_{50}Nb_{50-x}X_x$  systems. Lower binding energy values were observed for Co addition as compared to Sn. It can be seen that the binding energy decreases more for Sn as compared to Co addition, with Co being more favourable in this composition range. We have noted that doping on the  $Zr_{78}Nb_{22-x}X_x$  system with either Sn or Co is more energetically favourable compared to the  $Zr_{50}Nb_{50-x}X_x$  system. Furthermore, it was observed that the energy difference with Co and Sn doping is on average 0.02 eV/atom.

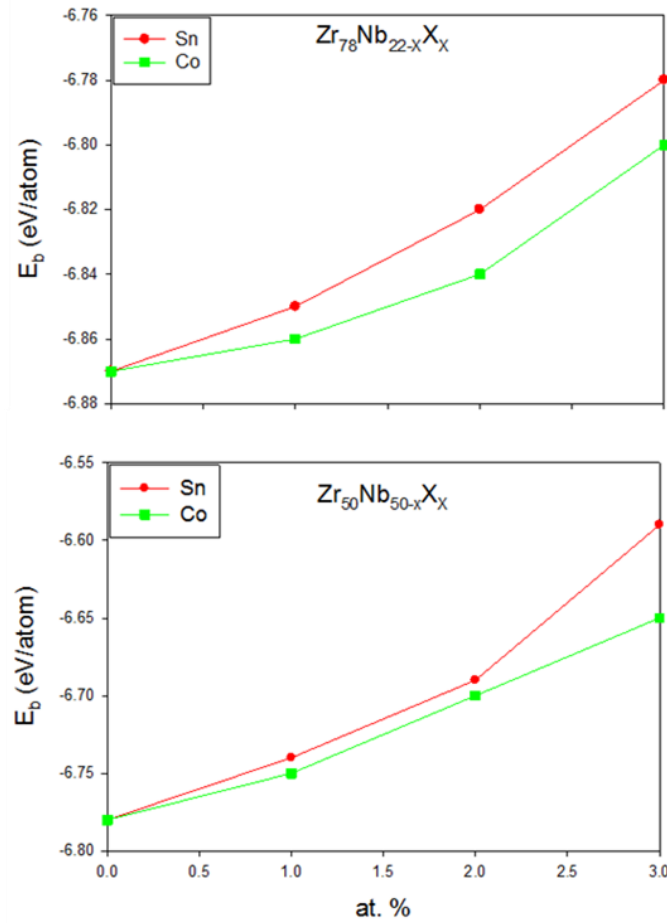


**Figure 6.1. Binding energy against the composition of  $Zr_{78}Nb_{22-x}X_x$  and  $Zr_{50}Nb_{50-x}X_x$  ( $x = Co, Sn$ ) at 0K.**

### 6.1.2. Co and Sn at varied temperature

We evaluated the effect of Co and Sn addition at varied temperatures (Figure 6.2). In Figure 6.2 A, we established the effect of Sn addition on the  $Zr_{50}Nb_{50}$  system. The 1 at. % Sn addition compares better with the pure Zr system and the  $Zr_{50}Nb_{50}$  systems. Furthermore, as the Sn content is increased to 2 and 3 at. %, the binding energy increases which make the structures to be energetically unfavourable (less stable). Furthermore, these observations suggest a small amount of Sn addition could be suitable for enhancing the stability of the  $Zr_{50}Nb_{50-x}X_x$  system.

Now, the dependence of binding energy for the  $Zr_{78}Nb_{22-x}Sn_x$  system in Figure 6.2 C is discussed. The Zr and  $Zr_{78}Nb_{22}$  systems show exactly similar trends as the

temperature is increased, this pattern is also observed for  $Zr_{78}Nb_{20}Sn_2$  and  $Zr_{78}Nb_{19}Sn_3$  systems. The  $Zr_{78}Nb_{20}Sn_2$  and  $Zr_{78}Nb_{19}Sn_3$  structures showed lower energies as temperature increase thus making them energetically unfavourable compared to the Zr system, while the binding energy for  $Zr_{78}Nb_{21}Sn_1$  system slightly increases (less negative) as compared to the  $Zr_{78}Nb_{22}$  and Zr systems.

The 2 and 3 at. % Sn additions show a poor binding ability at 1200 K, a sudden increase is observed at 1500 K, this may inform about the structure transforming (phase change), then no transformation is observed for  $Zr_{78}Nb_{22}$  and the Zr systems at 1200 K because there is no actual difference in their energies as the temperature is increased. The 1 at. % Sn addition does not display any physical change which suggests the suitability of this concentration for high-temperature applications up to 2400 K. The Sn addition, on the other hand, showed to enhance the binding energy of Zr and  $Zr_{78}Nb_{22}$  systems. These findings suggest that the  $Zr_{78}Nb_{21}Sn_1$  system showed a preferred trial over the  $Zr_{78}Nb_{20}Sn_2$  and  $Zr_{78}Nb_{19}Sn_3$  systems since it displayed the least energy at 400 – 2400 K temperature range.

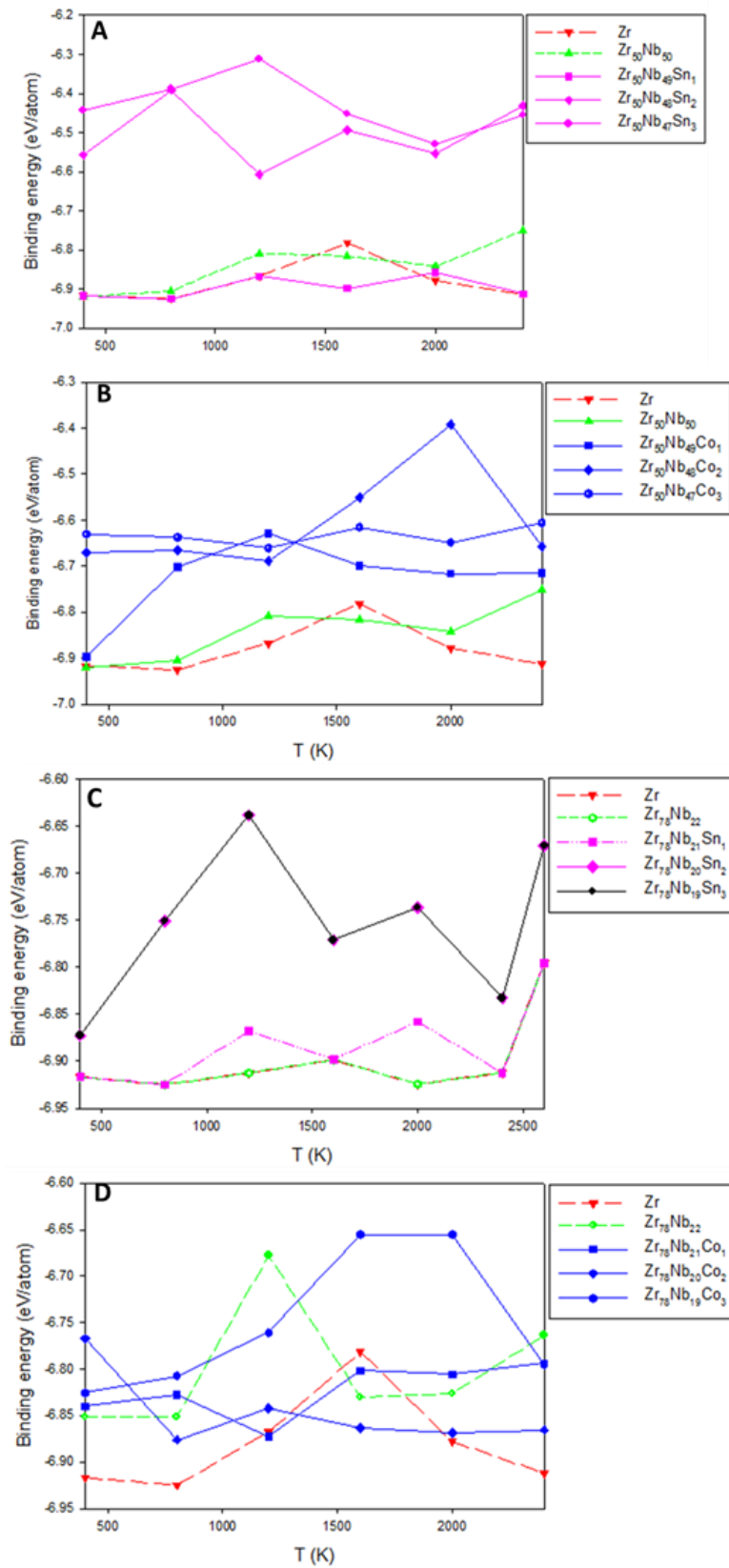


**Figure 6.2. Binding energy against temperature for  $\alpha$ -Zr,  $Zr_{78}Nb_{22}$ ,  $Zr_{50}Nb_{50}$  systems and ternary solid solutions of  $Zr_{78}Nb_{22-x}Sn_x$ ,  $Zr_{50}Nb_{50-x}Sn_x$ ,  $Zr_{78}Nb_{22-x}Co_x$  and  $Zr_{50}Nb_{50-x}Co_x$  alloy systems.**

The effect of Co addition on  $Zr_{50}Nb_{50}$  and  $Zr_{78}Nb_{22}$  systems is also investigated as shown in Figure 6.2 B and D, respectively. Now, for the  $Zr_{50}Nb_{50}$  system, we observe that the addition of Co content tends to slightly increase the binding energies of the pure Zr and 50 at. % Nb-doped systems. The undoped system is more energetically favourable as compared to the doped system. The introduction of 50 at. % Nb content has been shown to increase the binding energy slightly, which generates a somewhat comparably stabilized  $Zr_{50}Nb_{50}$  system (agrees with the undoped system). Additionally, the introduction of Co content shows that the structure binds less as concentration is increased to 2 and 3 at. % in  $Zr_{50}Nb_{50-x}Co_x$  system (see Figure 6.2 B). It is also shown that the 1 at. % Co content tends to bind well since there is no significant difference in the binding energies as the temperature increases up to 2400 K. This also correlates well with the elastic constants against increasing temperatures for  $Zr_{50}Nb_{48}Co_2$  system. Moreover, the 1 and 2 at. % Co content could be considered favourable additions and may be recommended for the advancement of higher temperature Zr alloy applications.

The  $Zr_{78}Nb_{21}Co_2$  system has slightly increased compared to the binary and undoped system especially above 1500 K, this suggests that the 2 at. % Co addition could also be suitable for use at higher temperatures (see Figure 6.2 D). Moreover, the undoped and the doped systems i.e. for Zr,  $Zr_{78}Nb_{22}$  and  $Zr_{78}Nb_{22-x}Co_x$  systems, tend to show transforming behaviours at 800 K because the binding energy shows an insignificant pattern (the pattern changes immediately). The structures are maintained afterward since they do not display an uncharacteristic binding energy difference above 800 K. The  $Zr_{78}Nb_{19}Co_3$  system is less energetic because the binding energy has largely increased compared to the undoped system. The

$Zr_{78}Nb_{20}Co_2$  and  $Zr_{78}Nb_{21}Co_1$  systems could be favourable since there is less difference in their binding energies as the temperature is increased up to 2400 K.

## 6.2. Density of states

In this section, we examine the influence of Co and Sn additions on the electronic density of states for  $1 < x < 3$  at 0 K, the small ternary addition was reported to affect the properties of the Zr-based alloys [26]. Figure 6.3 compares the total density of state for the  $Zr_{50}Nb_{50-x}X_x$  system (in Figure 6.3 A, B and C) and  $Zr_{78}Nb_{22-x}X_x$  system (in Figure 6.3 D, E and F). We observed the trend of the density of states near the Fermi level to establish the electronic stability of these systems. A similar analysis has been used to confirm the electronic stability of compounds previously [114].

We note that at 1 at. % composition,  $Zr_{50}Nb_{49}X_1$  system, where  $X = (Co \text{ or } Sn)$ , the states are similar at  $E_f$  for both Co and Sn addition with those for pure (undoped) Zr lowest. However, as the composition is increased, we observed states shifting at  $E_f$ , with the  $Zr_{50}Nb_{49}Sn_1$  system's DOS shifting upwards (higher) while for the  $Zr_{50}Nb_{49}Co_1$  system they shifted lower energy. A further increase to 3 at. % composition showed a significant difference, the Co doped DOS lies lower at  $E_f$  while those for Sn doped formed a broader peak at  $E_f$  (DOS peak shifted towards the valence band). The  $Zr_{50}Nb_{47}Co_3$  system is found to be electronically stable because the number of DOS is lowered at the fermi energy ( $E-E_f = 0$ ) as compared to that of Sn.

The case of the  $Zr_{78}Nb_{22-x}X_x$  structure can be characterised by the shifting of states with respect to the  $E_f$  and a possible pseudogap. At 1 at. % composition, the pseudogap lies slightly on the valence band (similar to the  $Zr_{50}Nb_{50-x}X_x$  system). The DOS for Co doped system is the highest and lowest for Sn doped. It can be seen



that as the composition is increased to 2 and 3 at. %, the Co doped DOS increases (states are higher at  $E_f$ ), this may suggest that the structure is becoming unstable at high Co content.

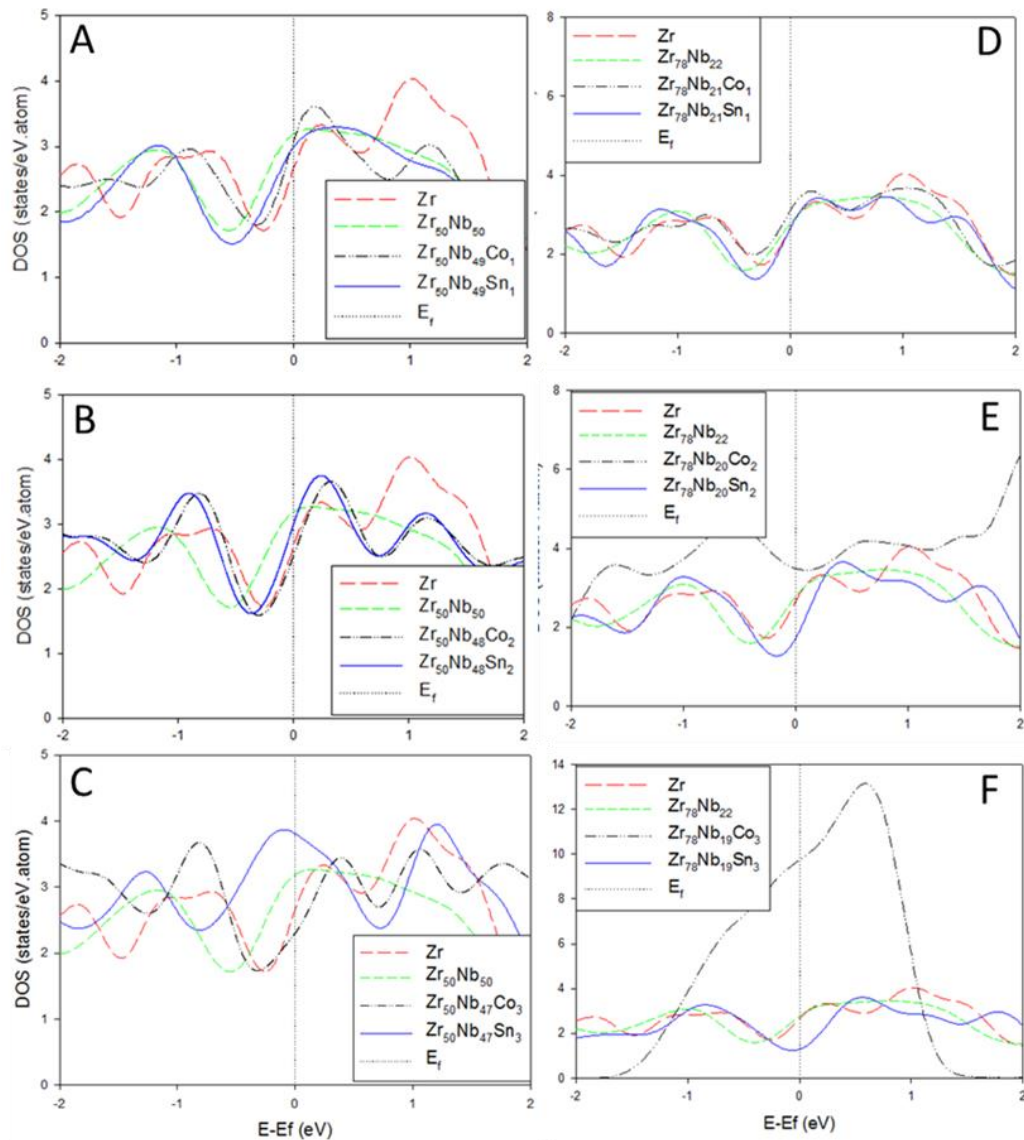


**Figure 6.3. Comparison of the DOS for the  $Zr_{78}Nb_{22-x}X_x$  and  $Zr_{50}Nb_{50-x}X_x$  systems. The Fermi energy is taken as the energy zero ( $E-E_f = 0$ ).**

More interestingly, the DOS for Sn doped showed stability as the composition is increased. We see that at 3 at. % Sn, the Fermi level fall in the pseudogap (states been shifted towards the conduction band). This lowering of states at  $E_f$  may be attributed to the stability of the  $Zr_{78}Nb_{19}Sn_3$  structure. Concentration plays an

important role in these systems since different percentages are required for addition in different structures.

### 6.3. Elastic properties

In this section, we evaluate the effect of temperature on the elastic constants of Zr,  $Zr_{50}Nb_{50}$ ,  $Zr_{78}Nb_{22}$ ,  $Zr_{78}Nb_{22-x}X_x$  and  $Zr_{50}Nb_{50-x}X_x$  systems where X is chosen as either Co or Sn at. % additions. The structures are considered to predict their mechanical stability under heat treatment or varying temperatures. Now, in Figure 6.4 (A), we show the elastic constants of the  $\alpha$ -Zr system. The  $C_{12}$  parameter is found to be greater than the  $C_{11}$  parameter at temperatures above 500 K up to 1500 K, this led to the  $C'$  becoming negative. All elastic moduli are found to be positive above 2000 K since the  $C_{11}$  is greater than  $C_{12}$ . The  $C_{44}$  is positive throughout the temperature range considered, suggesting that the system is trigonal/tetragonal stable. The undoped system is mechanically unstable with temperature treatment (400 – 2400 K) since  $C'$  is negative ( $C' < 0$ ) except for 2000 K.

In Figure 6.4 B, we evaluated the effect of 50 at. % Nb addition on the  $\alpha$ -Zr. The additions of Nb content have been shown to improve the  $C_{11}$  parameter which becomes greater than the  $C_{12}$  giving rise to a positive  $C'$  value (condition of stability). The  $C_{44}$  is also positive satisfying the stability criterion. All elastic moduli are positive suggesting that the  $Zr_{50}Nb_{50}$  system is mechanically stable with temperature treatment or increasing temperature up to 2400 K.

In Figure 6.4 (C, D and E), we investigate the effect of Sn addition in the  $1 \leq x \leq 3$  atomic percent range. The 1 at. % Sn addition was found to slightly decrease the elastic constant values in the entire temperature range but remains positive (as a result the  $Zr_{50}Nb_{49}Sn_1$  structure is mechanically stable). We further investigate the

Zr<sub>50</sub>Nb<sub>48</sub>Sn<sub>2</sub> and Zr<sub>50</sub>Nb<sub>47</sub>Sn<sub>3</sub> plots (Figure 6.4 D and E) to study the effect of Sn addition of 2 and 3 atomic percent, respectively. We found that the 2 and 3 at. % Sn content is favourable since all elastic moduli remain positive at temperatures up to 2400 K.

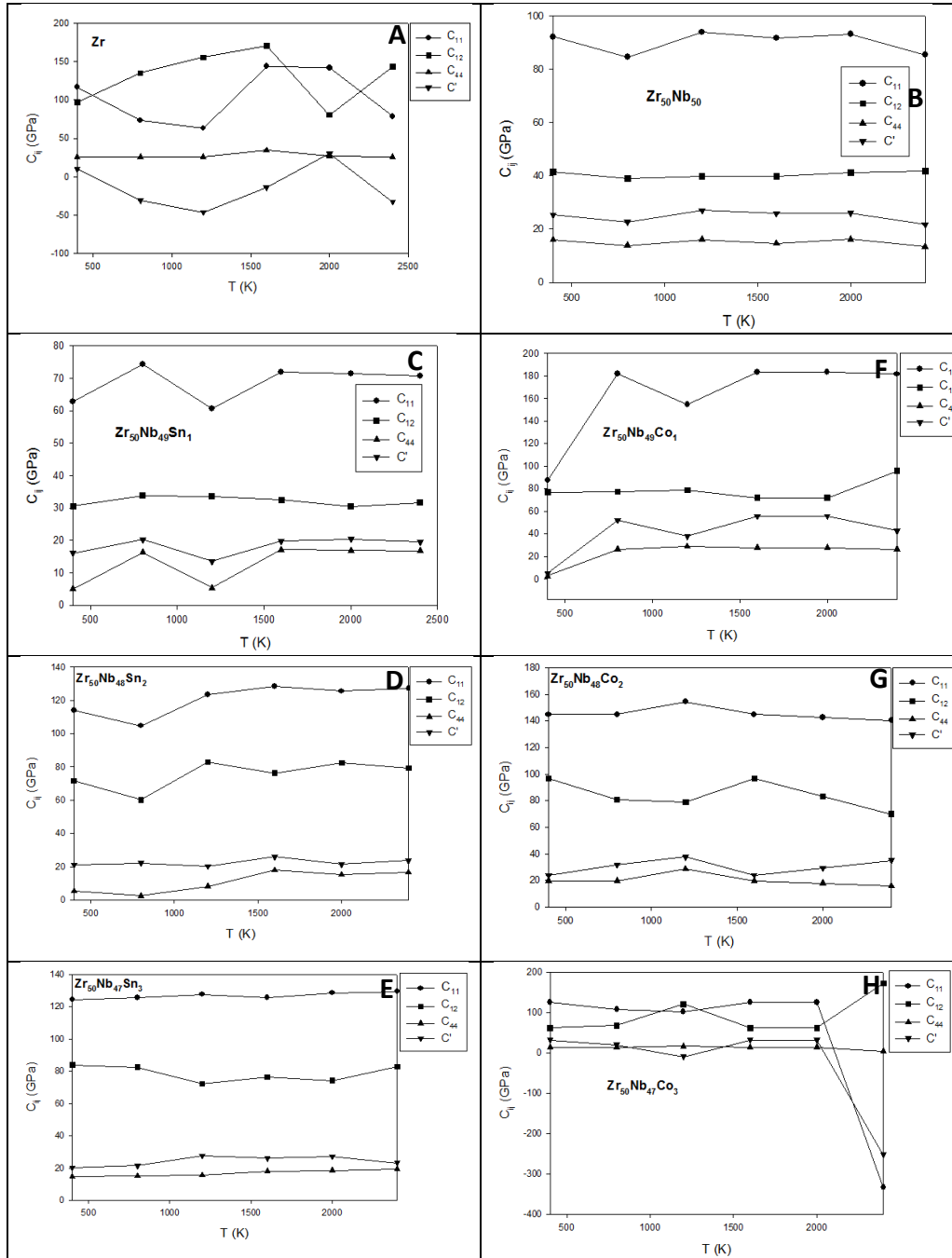


Figure 6.4. Elastic constants for (A)  $\alpha$ -Zr, (B) Zr<sub>50</sub>Nb<sub>50</sub>, (C) Zr<sub>50</sub>Nb<sub>49</sub>Sn<sub>1</sub>, (D) Zr<sub>50</sub>Nb<sub>48</sub>Sn<sub>2</sub>, (E) Zr<sub>50</sub>Nb<sub>47</sub>Sn<sub>3</sub>, (F) Zr<sub>50</sub>Nb<sub>49</sub>Co<sub>1</sub>, (G) Zr<sub>50</sub>Nb<sub>48</sub>Co<sub>2</sub> and (H) Zr<sub>50</sub>Nb<sub>47</sub>Co<sub>3</sub> systems versus temperature to investigate their mechanical stability.

We now focus on the effect of Co addition on the  $Zr_{50}Nb_{50}$  system in Figure 6.4 F, G and H. Recall that the 50 at. % Nb addition has been shown to improve the mechanical stability of pure Zr as discussed above. It is seen that the effect of Co addition on the  $Zr_{50}Nb_{50}$  system (substituting the Nb sublattice) is also favourable at increasing temperature conditions. All elastic moduli are positive for 1 at. % Co addition which means the structure is mechanically stable with that Co content as shown in Figure 6.5 A. It is also noted that at this concentration (1 at. % Co) the values of  $C_{11}$  and  $C_{12}$  are high or increased. As a result,  $C_{44}$  and  $C'$  values have increased.

Now, considering the case of increased Co concentration. We investigate the 2 and 3 at. % Co addition to further understand the effect of increasing the Co concentration on the  $Zr_{50}Nb_{50}$  system for various temperatures (see Figure 6.4 F and G). As the Co content is increased to 2 at. % the elastic moduli reduce closer to zero at lower temperature especially for  $C_{44}$  and  $C'$  but remain positive which suggests that the structure is mechanically stable. However, for 3 at. % Co addition, we note that at 2400 K the  $Zr_{50}Nb_{57}Co_3$  structure is mechanically unstable with the  $C'$  being negative. This is due to the  $C_{11}$  reducing more than the  $C_{12}$ . Thus the Co addition is favourable for up to 2 at. % since all elastic moduli are positive for the entire temperature range considered.

In Figure 6.5, we investigate the mechanical stability of the  $Zr_{78}Nb_{22-x}Co_x$  system under heated conditions or increasing temperature as in the case of the  $Zr_{50}Nb_{50}$  system. The behaviour of Zr has already been established. We now focus on the binary  $Zr_{78}Nb_{22}$  system in Figure 6.5 (B). It is clear that at a temperature below 1600 K, the  $C'$  is negative, this is due to the  $C_{11}$  reducing more than the  $C_{12}$ . The  $C_{44}$  is positive at the temperature range. However, above 1600 K, we observe the shift or

contrast behaviour with the  $C_{44}$  becoming negative and the  $C'$  also becoming positive, and vice versa. This behaviour may suggest that the structure is unstable above 1600 K.

The addition of between 1 and 3 at. % Sn has been shown to improve the mechanic stability of the  $Zr_{78}Nb_{22}$  system since the  $C'$  and  $C_{44}$  are positive for all temperature range (see Figure 6.5 C, D and E). Sn tends to be a better alloying element for the  $Zr_{78}Nb_{22}$  system at varying temperatures because of its additions up to 3 at. % are favourable and this could be suitable for the enhancement of advanced high-temperature cladding materials. Similar behaviour is observed for Co addition in Figure 6.5 (F, G and H). The effect of Co addition on the  $Zr_{78}Nb_{22}$  system at increasing temperature revealed stability of the system with  $C'$  values greater than  $C_{44}$  for some temperature range. For example, 1 at. % Co gave close values for  $C'$  and  $C_{44}$  for 1600 K and it is different for 2 and 3 at. % Co addition. Where a coupling of  $C_{44}$  and  $C'$  is observed at 900 K (1 at. %), and 600 K and 2300 K for 3 at. % Co which implies that zero stress is imposed there thus it is considered stable. We see that for this case of ternary alloying with either Sn or Co, the structure is mechanically stable since all stability conditions of the system are satisfied.

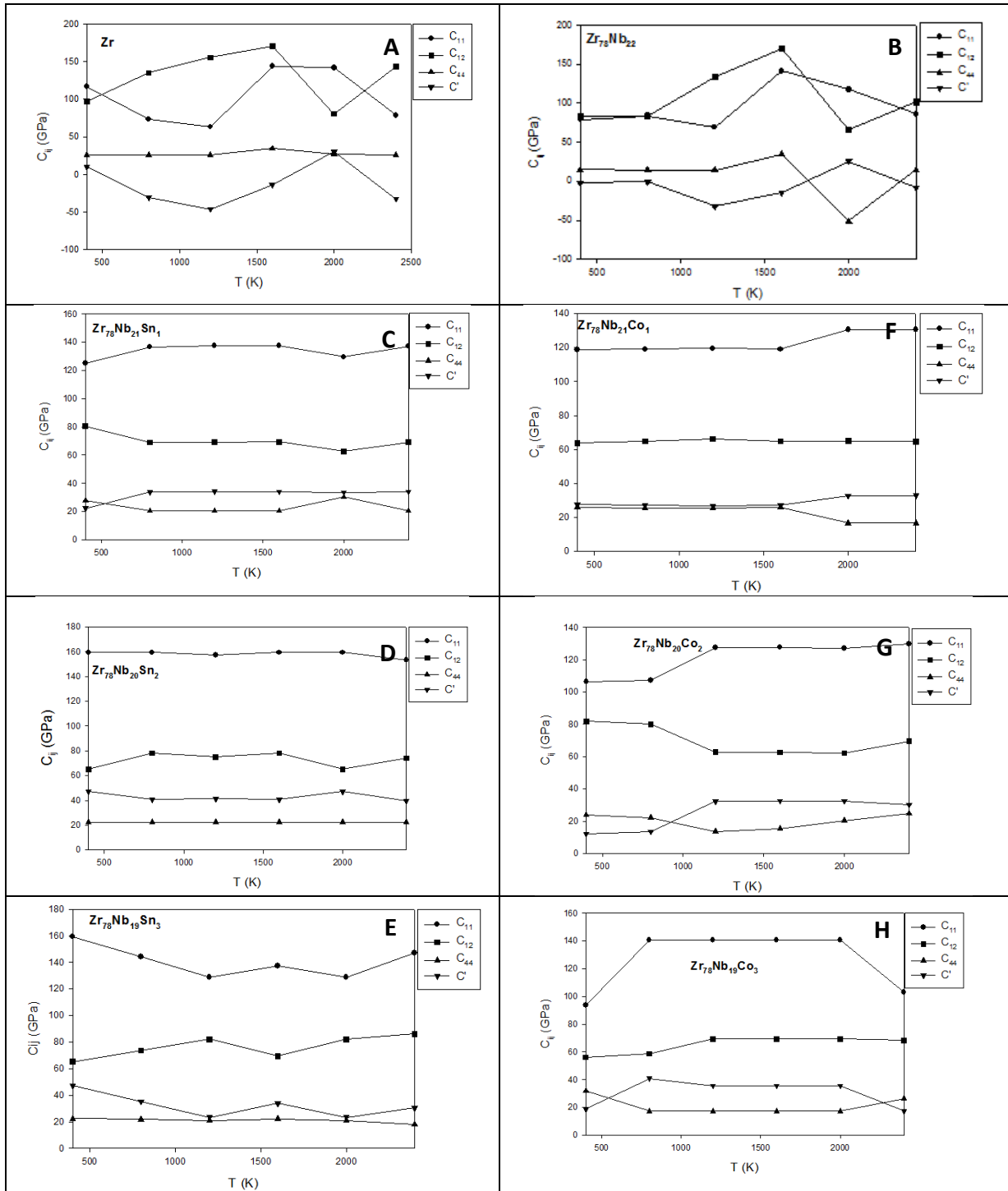
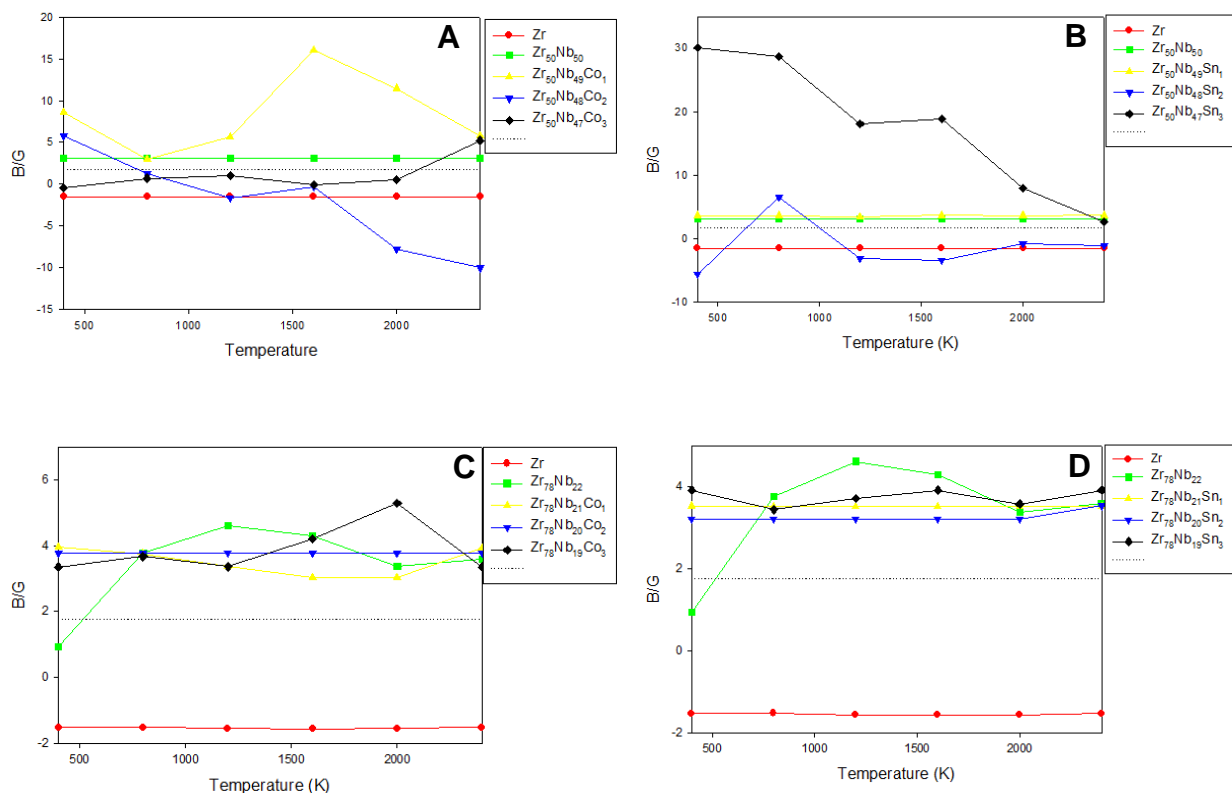


Figure 6.5. Elastic constants of (A)  $\alpha$ -Zr, (B)  $Zr_{78}Nb_{22}$ , (C)  $Zr_{78}Nb_{21}Sn_1$ , (D)  $Zr_{78}Nb_{20}Sn_2$ , (E)  $Zr_{78}Nb_{19}Sn_3$ , (F)  $Zr_{78}Nb_{21}Co_1$ , (G)  $Zr_{78}Nb_{20}Co_2$  and (H)  $Zr_{78}Nb_{19}Co_3$  systems versus temperature to investigate their mechanical stability at increasing temperature.

## 6.4. Bulk over shear modulus (Pugh's ratio)

In this section, the bulk (B) over shear modulus (G) at increasing temperature to verify the strength and applicability of the Zr-Nb-X systems is evaluated. Note that the G represents the resistance to plastic deformation, while the B represents the resistance to fracture [119]. A high B/G ratio is associated with ductility whereas a low value corresponds to brittle nature. The critical value which separates ductile and brittle materials is 1.75 that is if  $B/G > 1.75$  the material behaves in a ductile manner, otherwise, the material behaves in a brittle manner according to Pugh's brittleness/ductility criterion [108, 120].



**Figure 6.6.** The B/G ratio against temperature for Zr-Nb-X systems in the left column (A, C)  $Zr_{50}Nb_{50-x}Co_x$  and  $Zr_{78}Nb_{22-x}Co_x$  while right column (B, D)  $Zr_{50}Nb_{50-x}Sn_x$  and  $Zr_{78}Nb_{22-x}Sn_x$ . The dotted line represents  $B/G = 1.75$ .

The pure Zr is observed to be brittle since the B/G ratio is less than 1.75 as shown in Figure 6.6 (A). However, the addition of 50 at. % Nb has shown to improve the

brittleness of Zr since the  $Zr_{50}Nb_{50}$  system shows ductile behaviour ( $B/G > 1.75$ ). Furthermore, the 1 at. % Co addition also follows a similar trend with the  $Zr_{50}Nb_{50}$  system which makes the  $Zr_{50}Nb_{49}Co_1$  system to be ductile for the entire concentration range considered ( $B/G > 1.75$ ). As on the 2 and 3 at. % additions, the systems appear to be brittle ( $B/G$  ratios of less than 1.75) this is shown in Figure 6.6 (A). In the case of the  $Zr_{78}Nb_{22}$  system, it is clear that both binary and ternary systems with the addition of Co gives a high  $B/G$  ratio ( $B/G > 1.75$ ), implying that the structure is ductile (Figure 6.6 C).

A different trend is observed for Sn addition ( $Zr_{50}Nb_{50-x}Sn_x$ ), it is seen that the 1 at. % Sn addition is ductile while the 2 at. % is brittle. Moreover, we observed that for the case of 3 at. % Sn, the structure show ductility (see Figure 6.6 B) as the temperature increase. Now, Figure 6.6 (D) displays the additions of Sn for  $Zr_{78}Nb_{22-x}Sn_x$  systems. It is observed that the 22 at. % Nb system favours Sn additions quite well because they appear to be ductile with increasing temperature as their  $B/G$  ratios are above 1.75.

## 6.5. Young's Modulus

We now evaluate the dependency of Young's modulus on temperature for Zr-based systems under study. The Young's modulus is used to measure the stiffness of a solid material [121]. A higher value of Young's modulus confirms that the material is highly rigid (strong stiffness) while a lower value confirms a weaker stiffness.

Figures 6.7. (A, B, C and D) presents the dependency of Young's Modulus on temperature for various systems under investigation that is Zr,  $Zr_{50}Nb_{50}$ ,  $Zr_{78}Nb_{22}$ ,  $Zr_{50}Nb_{50-x}X_x$  and  $Zr_{78}Nb_{22-x}X_x$  systems, where X is either Co or Sn. Now, a lower value of Young's Modulus is observed for pure Zr, thus it is considered flexible (low



stiffness). The 50 at. % Nb addition showed enhanced flexibility such that the  $Zr_{50}Nb_{50}$  system becomes stiffer since it has a higher value of Young's modulus. We further analyse the effect of adding Co in the system for smaller concentrations of 1, 2 and 3 at. %. It is seen that the stiffness is maintained for 1 and 2 at. % with increasing temperature since their graphs show lie close to each other. We observe that the 3 at. % show low stiffness at a lower temperature below 1200 K, and high stiffness at about 1600 K. The stiffness is reduced for 2 at. % Co at this temperature. Similarly, the case of 1 to 3 at. % Sn addition has been shown to maintain the stiffness as shown in Figures 6.7 (A and B). Moreover, a weaker stiffness is observed at 2000 K for the  $Zr_{50}Nb_{48}Sn_2$  system.

The 22 at. % Nb addition was also evaluated, it is shown that the values of Young's modulus have increased for pure Zr when Nb is added. The 1 to 3 at % Co addition has improved the stiffness of  $Zr_{78}Nb_{22}$  system as the temperature increases and this is plotted in Figure 6.7 (C). A similar trend is also observed for Sn addition within the 1, 2 and 3 at. % (Figure 6.7 D), thus the ternary additions of Co and Sn are favourable (enhance the stiffness of the system).

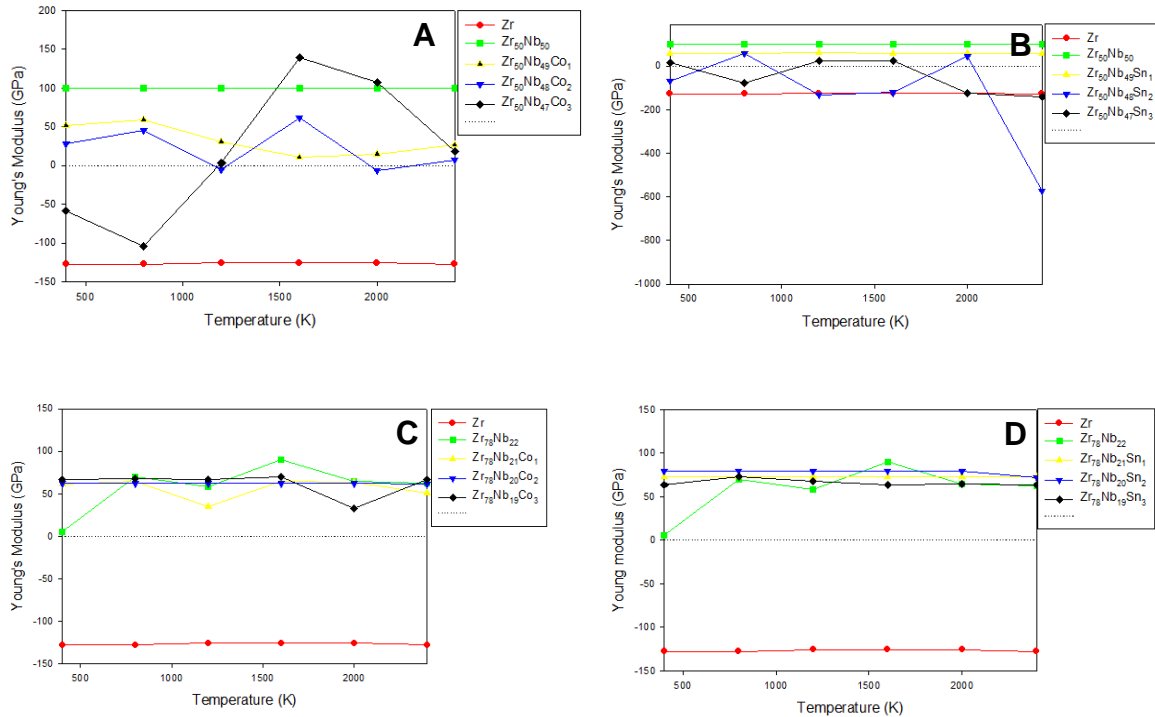


**Figure 6.7.** Displaying Young's modulus versus temperature for  $Zr_{50}Nb_{50-x}Co_x$  and  $Zr_{78}Nb_{22-x}Co_x$  systems (A, C) while (B, D) displays for  $Zr_{50}Nb_{50-x}Sn_x$  and  $Zr_{78}Nb_{22-x}Sn_x$  systems respectively.

## 6.6. Poisson's ratio

To confirm the strength of the Zr-based systems, we evaluate Poisson's ratio ( $\sigma$ ) at varying temperatures for pure Zr,  $Zr_{50}Nb_{50}$ ,  $Zr_{78}Nb_{22}$ ,  $Zr_{50}Nb_{50-x}X_x$  and  $Zr_{78}Nb_{22-x}X_x$  systems where X is Co or Sn. This is done for small compositions as above. Note that the structure is considered ductile when the value of  $\sigma$  is greater than 0.26 otherwise brittle. Furthermore, isotropic materials require that  $\sigma$  varies in the range  $-1 \leq \sigma \leq 0.5$ . In isotropic material, the properties are the same in all directions whereas in anisotropic the properties of a material are direction-dependent [122].

Figures 6.8 (A and B) present the  $\sigma$  for pure Zr,  $Zr_{50}Nb_{50}$  and  $Zr_{50}Nb_{49-x}X_x$  systems. The Zr system appears to be anisotropic since it is above the upper isotropic limit of 0.5 yet ductile because the  $\sigma$  value is above 0.26. Now, we discuss the addition of 50 at. % Nb on Zr ( $Zr_{50}Nb_{50}$  system). As can be seen from Figures (A and B) the  $\sigma$

value has been reduced to 0.35, this finding suggests that the  $Zr_{50}Nb_{50}$  system is isotropic and ductile within the temperature range.

The addition of 1, 2 and 3 at. % Co is shown in Figure 6.8 A, it is seen that the 1 at. % Co is favourable with a high  $\sigma$  value as the temperature is increased, the  $\sigma$  values are found in the range between 0.34-0.46. A consistent trend producing a linear graph is observed for 2 at. % Co with the  $\sigma$  in the range of (0.18-0.55) where. The  $Zr_{50}Nb_{48}Co_2$  system appears to be brittle (least ductile) at 800 K with  $\sigma$  being less than 0.26 and hence anisotropic. The case of the 3 at. % Co, however, appears to be isotropic and show ductility at about 1200 K with  $\sigma$  values of 0.47, and ductility is reduced beyond this temperature. These findings suggest that the  $Zr_{50}Nb_{50}$ ,  $Zr_{50}Nb_{49}Co_1$  and  $Zr_{50}Nb_{48}Co_2$  systems could be favourable for applications at a higher temperature because they are ductile and isotropic. This may also suggest that properties such as tensile strength, electrical resistance and thermal expansion are of equal magnitude in any direction through the material.

Figure 6.8 (C) illustrates the effect of adding at. % Co to the  $Zr_{78}Nb_{22}$  system for ( $1 \leq x \leq 3$ ). The 22 at. % Nb addition has been seen to improve the ductility and isotropic properties of the Zr system since it has been shown to reduce the  $\sigma$  value from 0.94 to 0.38 which falls within the isotropic limit of  $-1 \leq \sigma \leq 0.5$ . The Co additions appear to render the system ductile since the  $\sigma$  values are above 0.26 at all temperature range. Furthermore, the  $Zr_{78}Nb_{22-x}Co_x$  systems are seen to be isotropic because they fall within the isotropic range ( $-1 \leq \sigma \leq 0.5$ ). This addition is found to be favourable at the temperature range of (400 K - 2400 K). This may imply that 1 and 2 at. % Co additions are more preferred than the 3 at. % Co at higher temperatures.

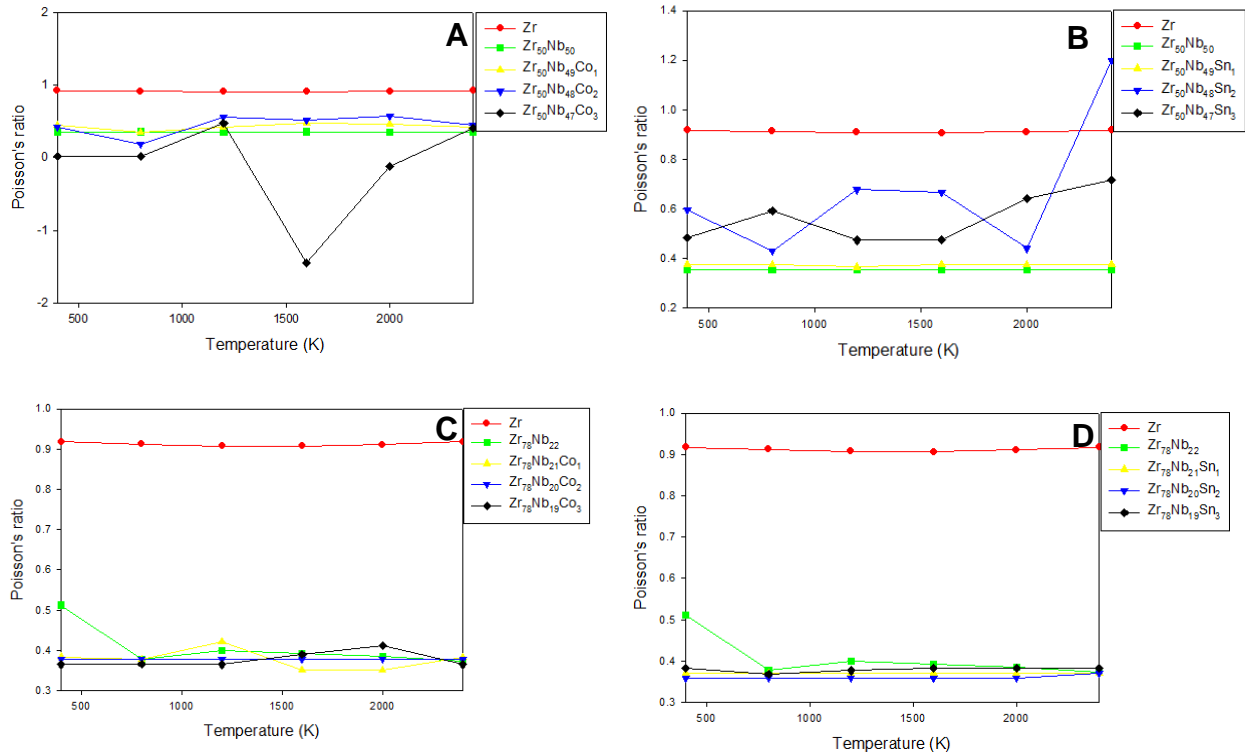


**Figure 6.8.** Indicative Poisson's ratio against temperature for Zr<sub>50</sub>Nb<sub>50-x</sub>Co<sub>x</sub> and Zr<sub>78</sub>Nb<sub>22-x</sub>Co<sub>x</sub> systems (A, C) while (B, D) displays for Zr<sub>50</sub>Nb<sub>50-x</sub>Sn<sub>x</sub> and Zr<sub>78</sub>Nb<sub>22-x</sub>Sn<sub>x</sub> systems respectively.

The addition of Sn within a similar composition (1, 2 and 3 at. %) is also discussed to observe the strength of the Zr<sub>78</sub>Nb<sub>22</sub> system as the temperature is increased. It is observed in Figure 6.8 (D) that a similar trend as for the (1 ≤ x ≤ 3 at. % Co addition on Zr<sub>78</sub>Nb<sub>22-x</sub>Co<sub>x</sub>) occurs. The  $\sigma$  of above 0.26 is observed for all percentage content of Sn. We found that the Zr<sub>78</sub>Nb<sub>22-x</sub>Sn<sub>x</sub> system is ductile with  $\sigma > 0.26$  for all concentration range. Moreover, the structure appears to be isotropic because the system satisfies the isotropic limits.

# Chapter 7

## 7.1. Summary and Conclusion

In this study, the equilibrium lattice parameters of Zr, Nb,  $Zr_{50}Nb_{50}$ ,  $Zr_{78}Nb_{22}$  and ternary alloying with Co and Sn systems were performed within the generalized gradient approximation (GGA) using the first principles *ab initio* and molecular dynamics calculations. The Zr-based systems are applicable for the development of fuel cladding materials, basically on the mechanical components of the nuclear fuel assemblies such as control rods, fuel rods and in-core instrumentation. The predicted lattice parameters of Zr and Nb compare well with the experimental values to within 1% while those for  $Zr_{50}Nb_{50}$  and  $Zr_{78}Nb_{22}$  systems were found to be reasonable. The lattice parameters also reduce with the introduction of the third element such as Co and Sn. The decrease in lattice parameter (consequently decrease in volume) is attributed to the difference in the size of the atomic radius of Co, Sn and Nb.

The thermodynamic stability was evaluated by calculating the heat of formation. It was found that the heats of formation increased as the Nb content is increased for binary systems. A positive heat of formation values were observed for various ternary systems such as  $Zr_{99}Nb_{1-x}Co_x$ ,  $Zr_{98.8}Nb_{1.2-x}Co_x$ ,  $Zr_{98.1}Nb_{1.9-x}Co_x$ ,  $Zr_{97.5}Nb_{2.5-x}Co_x$ ,  $Zr_{97}Nb_{3-x}Co_x$  and  $Zr_{78}Nb_{22-x}Co_x$ . The systems were found to be thermodynamically unstable above 2 at. % addition. Only smaller amounts were required for the systems to be thermodynamically stable.

We have also performed the elastic and electronic properties of the Zr-Nb and Zr-Nb-Co and Zr-Nb-Sn systems. The mechanical stability was deduced from elastic constants ( $C_{11}$ ,  $C_{12}$ ,  $C_{44}$  and  $C'$ ) which were considered vital since the other

constants were insignificant. The elastic stability for binary systems ( $Zr_{99}Nb_1$ ,  $Zr_{98.8}Nb_{1.2}$ ,  $Zr_{98.1}Nb_{1.9}$ ,  $Zr_{97.5}Nb_{1.5}$ ,  $Zr_{97}Nb_3$  and  $Zr_{78}Nb_{22}$ ), while for ternary systems ( $Zr_{99}Nb_{1-x}Co_x$ ,  $Zr_{98.8}Nb_{1.2-x}Co_x$ ,  $Zr_{98.1}Nb_{1.9}$ ,  $Zr_{97.5}Nb_{1.5-x}Co_x$ ,  $Zr_{97}Nb_{3-x}Co_x$  and  $Zr_{78}Nb_{22-x}Co_x$ ) were determined. This also includes the Sn addition ( $Zr_{50}Nb_{50-x}Sn_x$  and  $Zr_{78}Nb_{22-x}Sn_x$ ). The bulk to shear quotient (Pugh's ratio) has indicated that they are ductile ( $B/G > 1.75$ ). The addition of smaller Co contents (ternary alloy) was found to be ductile particularly for 1 at. % Sn and Co (both  $Zr_{50}Nb_{50-x}X$  and  $Zr_{78}Nb_{22-x}X_x$  where X is either Co or Sn) and otherwise, they were brittle ( $B/G < 1.75$ ) that is for 2 and 3 at. % Co and Sn addition in both ternary systems. The systems were found to be isotropic and ductile at lower concentrations to within 1 and 2 at. % for either Sn or Co addition at increasing temperature.

The electronic stabilities of the systems were evaluated and the characterization of their trends was depicted using the DOS plots. The states with the lowest peak at the Fermi energy are considered the most stable and the order of stability was found from low to high Co concentration. It was also found that the  $\alpha$ -Zr and the binary systems:  $Zr_{99}Nb_1$ ,  $Zr_{98.8}Nb_{1.2}$ ,  $Zr_{98.1}Nb_{1.9}$ ,  $Zr_{97.5}Nb_{1.5}$ ,  $Zr_{97}Nb_3$  and  $Zr_{78}Nb_{22}$ , are electronically stable, consistent with their  $\Delta H_f$  calculations. Now, the effect of Co addition to the binary systems has indicated electronic stability within smaller concentrations of 1 atomic percent. The findings suggested that a smaller Co content (1 at. % Co) addition is favourable. More importantly, we found a good agreement between the electronic stability and the heat of formation.

The molecular dynamics calculations were used to determine the mechanical, thermodynamic and electronic stability of  $Zr_{50}Nb_{50-x}X_x$  and  $Zr_{78}Nb_{22-x}X_x$  systems at increased temperatures using the DMol<sup>3</sup> code. This to understand the effect on the possible applications of these systems in various environments such as in the

nuclear and medical industries. Now, the binding energies at 0 K tend to increase slightly with an increase in Nb content. A smaller addition in the range  $1 \leq x \leq 3$  where x represents the concentration of either Co or Sn had been found as suitable additions because they showed an enhanced effect on the properties (structural, electronic and mechanical properties). The Co addition to the systems ( $Zr_{50}Nb_{50-x}X_x$  and  $Zr_{78}Nb_{22-x}X_x$ ) appears to be favourable over the Sn addition. This is observed with the binding energies for Co being more negative than for Sn additions at 0 K.

The binding energies at a varied temperature from 400 – 2400 K which is guided by the experimental and theoretical melting temperature of Zr were evaluated. It was found that the binding energies also increased slightly as the 50 at. % Nb and 22 at. % Nb content is added to the Zr system to form ( $Zr_{50}Nb_{50}$  and  $Zr_{78}Nb_{22}$ ). These systems could be useful for future Zr-based alloy applications. Moreover, the electronic stability indicated that the pure system (Zr), binary ( $Zr_xNb_x$ ) and the preceded ternaries ( $Zr_{50}Nb_{50-x}X_x$  and  $Zr_{78}Nb_{22-x}X_x$ ) systems were electronically stable. In the case of the ternaries, the electronic stability was allowable for smaller additions of Co or Sn ( $Zr_{50}Nb_{49}Co_1$ ,  $Zr_{50}Nb_{49}Sn_1$ ,  $Zr_{78}Nb_{21}Co_1$  and  $Zr_{78}Nb_{21}Sn_1$ ). The Sn addition was found to be favoured for the  $Zr_{78}Nb_{22-x}Sn_x$  system while the Co addition was favourable for the  $Zr_{50}Nb_{50-x}Co_x$  system.

The mechanical stability was evaluated at an increased temperature. All independent elastic constants were found to be positive for the investigated systems (condition of mechanical stability). Their ductility and stiffness were determined from the B/G ratio, Young's Modulus and Poisson's ratio. These compounds ( $Zr_{50}Nb_{49}Co_1$ ,  $Zr_{50}Nb_{48}Co_2$ ,  $Zr_{50}Nb_{49}Sn_1$ ,  $Zr_{50}Nb_{48}Sn_2$ ,  $Zr_{78}Nb_{21}Co_1$ ,  $Zr_{78}Nb_{20}Co_2$ ,  $Zr_{78}Nb_{21}Sn_1$  and  $Zr_{78}Nb_{20}Sn_2$ ) appear stable within the temperature range of 400- 2400K) in terms of B/G, Y and  $\sigma$  are considered. These findings suggest that the ternary addition of either Co or Sn

for the  $Zr_{78}Nb_{22}$  system is a preferable choice over additions of similar elements for the  $Zr_{50}Nb_{50}$  system. The smaller amounts of Sn and Co concentrations (that is at 1 at. %) were found to enhance the stability of the  $Zr_{50}Nb_{50-x}X_x$  and  $Zr_{78}Nb_{22-x}X_x$  systems at increasing temperature. Thus it could be recommended for the advancement of high-temperature alloy applications, where Zr is of critical importance.

## 7.2. RECOMMENDATIONS AND FUTURE WORK

In light of the findings of this dissertation, several recommendations for future research are listed below:

- The current study has focused more on the Zr-Nb system with  $Zr_{50}Nb_{50}$  and  $Zr_{78}Nb_{22}$  ratio with Zr treated as the parent structure.
- Explore more concentrations such as  $Zr_{75}Nb_{25}$ ,  $Zr_{70}Nb_{30}$  systems, etc.
- Effect of other elements such as Mo, Fe, Cr, Ni and Sn(O)
- Expand to other approaches – supercell, and solid-disorder (SOD).
- Cluster expansions and phase diagram predictions to determine the composition and prediction of new alloys.
- Explore the effect of pressure on the structural, thermodynamic and elastic properties of the Zr-Nb-X alloys.



## REFERENCES

- [1] D.O. Northwood, "The development and applications of zirconium alloys," *Mater. Des.*, vol. 6, pp. 58-70, 1958.
- [2] S. Zhang, X. Zhang, Y. Zhu, S. Zhang, L. Qi and R. Liu, "First principle investigations on elastic and thermodynamic properties of zirconium under pressure," *Comput. Mater. Sci.*, vol. 61, pp. 42-49, 2012.
- [3] V.O. Kharchenko and D.O. Kharchenko, "Ab-initio calculations for structural properties of Zr-Nb alloys," *Condens. Matter Phys.*, vol. 16, pp. 1-8, 2013.
- [4] M.H. Chuma, P.E. Ngoepe and H.R. Chauke, "Computational modelling of Zr-Nb alloys," *Proc. S. A. Institute of Physics*, vol. 56, pp. 62-67, 2012.
- [5] D. Orlander and A. Motta, "Light water reactor materials," in *Zirconium alloys*, American Nuclear Society, Scientific publishers, 2011, pp. 1-3.
- [6] M. Christensen, W. Wolf, C.M. Freeman, E. Wimmera, R.B. Adamson and L. Hallstadius, "Effect of alloying elements on the properties of Zr and the Zr-H system," *J. Nucl. Mater.*, vol. 445, pp. 241-250, 2014.
- [7] R. Adamson, M. Griffiths and C. Patterson, "Irradiation growth of zirconium alloys (A Review)," *Adv. Nucl. Tech. Int.*, vol. 4041, pp. 5-7, 2017.
- [8] A.T. Motta, A. Couet and R.J. Comstock, "Corrosion of zirconium alloys used

- for nuclear fuel cladding,” *Annu. Rev. Mater. Sci.*, vol. 45, pp. 11-43, 2015.
- [9] A. Yilmazbayhan, A.T. Motta, R.J. Comstock, G.P. Sabol B. Lai, Z. Cai, “The role of hydrogen in zirconium alloy corrosion,” *J. Nucl. Mater.*, vol. 324, pp. 6-22, 2004.
- [10] V.O. Kharchenko and D. O. Kharchenko, “Ab-Initio calculations for structural properties of Zr-Nb alloys,” *Condens. Matter Phys.*, vol. 16, pp. 1-8, 2013.
- [11] J. Emseley, in *Nature’s building blocks: An A-Z guide to the elements*, Oxford University press, 2001, pp. 506-510.
- [12] A. Froideval, C Degueidre, C.U. Segre, M.A. Pouchon and G.D. Corros, “The influence of experimental conditions on the morphology and phase composition of Nb-doped ZrO<sub>2</sub> films prepared by spark anodization,” *Corros. Sci.*, vol. 173, pp. 99-105, 2013.
- [13] H.G. Kim, S.Y. Park and M.H. Lee, “Understanding corrosion and hydrogen pickup of Zr nuclear fuel cladding alloys - the role of oxide microstructure, porosity, suboxide and SPPs,” *J. Nucl. Mater.*, vol. 373, pp. 421-429, 2008.
- [14] C. Ramos, C. Saragovi and M.S. Granovsky, “Some new experimental results on the Zr-Nb-Fe system,” *J. Nucl. Mater.*, vol. 40, pp. 505-510, 2007.
- [15] P. Barberis, D. Charquet and V. Rebeyrolle, “Ternary Zr-Nb-Fe(O) system: phase diagram at 853K and corrosion behaviour in the domain Nb<0.8%,” *J. Nucl. Mater.*, vol. 326, pp. 163-174, 2004.
- [16] J. Wei, P. Frankel, E. Polatidis, M. Blat, A. Ambard, R.J. Comstock, L.

- Hallstadius, D. Hudson, G.P.W. Smith, C.R.M. Grovenor, M. Klaus, R.A. Cottis, S. Lyon and M. Preuss., "The effect of Sn on autoclave corrosion performance and corrosion mechanisms in Zr-Sn-Nb alloys," *Acta Mater.*, vol. 61, pp. 4200-4214, 2013.
- [17] R.S. Qiu, B.F. Luan, L.J. Chai, X.Y. Zhang and Q. Liu, "Effects of heating rates and alloying elements (Sn, Cu and Cr) on the alpha-alpha+beta phase transformation of Zr-Sn-Nb-Fe (Cu,Cr) alloys.," *J. Nucl. Mater.*, vol. 453, pp. 269-274, 2014.
- [18] D. de Fontaine, "Cluster approach to order-disorder transformations in alloys," *Sol. state. phys.*, vol. 47, pp. 33-176, 1994.
- [19] M. Cottura and E. Clouet, "Solubility in ZrNb alloys from first principles," *Acta Mater.*, vol. 144, pp. 21-30, 2018.
- [20] S.J. Yang and B. Wei, "Molecular dynamics simulation of liquid structure for undercooled Zr-Nb alloys assisted with electrostatic levitation experiments," *Chem. Phys. Lett.*, vol. 701, pp. 109-114, 2018.
- [21] A.T. Motta and J. Y. Park, "Zirconium alloys for supercritical water reactor application: challenges and possibilities," *J. Nucl. Mater.*, vol. 371, pp. 61-75, 2007.
- [22] I. Charit and K.L. Murty, "Creep behavior of niobium-modified zirconium alloys," *J. Nucl. Mater.*, vol. 374, pp. 354-363, 2008.
- [23] L. Hallstadius, S. Johnson and Ed Lahoda, "Cladding for high performance fuel,"

*Prog. Nucl. Energy*, vol. 57, pp. 71-76, 2012.

- [24] A. Zielinski and S. Sobieszczyk, "Hydrogen-enhanced degradation and oxide effects in zirconium alloys for nuclear applications," *Int. J. Hydrogen Energy*, vol. 36, pp. 8619-8629, 2011.
- [25] K.L. Murty and I. Charit, "Texture development and anisotropic deformation of zircalloys," *Prog. Nucl. Ener.*, vol. 48, pp. 325-359, 2006.
- [26] G.P. Sabol, P. Rudling and B. Kammenzind, "Zirconium in the nuclear industry," *14th Int. Symp. ASTM Int.*, vol. 2, pp. 3-24, 2005.
- [27] G. Choppin, J. O. Liljenzin, J. Rydberg and C. Ekberg, "Radiochemistry and nuclear chemistry," in *Nuclear power reactors*, Elsevier, 2013, pp. 658-668.
- [28] A.H. Fleitman, R.B. Herchenroeder and J.G.Y. Chow, "Cobalt-base alloys for use in nuclear reactors," *Nucl. Eng. Des.*, vol. 15, pp. 346-362, 1971.
- [29] W. Kohn and L.J. Sham, "Self-consistent equations including exchange and correlation effects," *Phys. Rev. A*, vol. 140, pp. 1133-1138, 1965.
- [30] P. Hohenberg and W. Kohn, "Inhomogeneous electron gas," *Phys. Rev. B*, vol. 136, pp. 867-871, 1964.
- [31] L. Bellaiche and D. Vanderbilt, "The virtual crystal approximation revisited: application to dielectric and piezoelectric properties of perovskites," *Cond. Matter Mater. Sci.*, vol. 1, pp. 1-7, 1999.
- [32] B. Delley, "DMol, a standard tool for density functional calculations: review and

- advances," *Theor. Comput. Chem.*, vol. 2, pp. 221-254, 1995.
- [33] H.R. Vega-Carrillo, I.R. Esparza-Garcia and A. Sanchez, "Features of a subcritical nuclear reactor," *Ann. Nucl. Ener.*, vol. 75, pp. 101-106, 2015.
- [34] IEE, "Nuclear Reactor Types," *An Environment & Energy FactFile*, pp. 1-13, November 2005.
- [35] B.D.C. Bell, S.T. Murphy, P.A. Burr, R.J. Comstock, J.M. Partezana, R.W. Grimes and M.R. Wenman, "The influence of alloying elements on the corrosion of Zr alloys," *Corros. Sci.*, vol. 1, pp. 1-21, 2016.
- [36] S. C. Lumley, S. T. Murphy, P. A. Burr, R. W. Grimes, P. R. Chard-Tuckey and M. R. Wenman, "The stability of alloying additions in zirconium," *J. Nucl. Mater.*, vol. 437, pp. 122-129, 2013.
- [37] A.S. Zaimovskii, "Zirconium alloys in nuclear power," *React. Mater. Sci. Conf.*, vol. 45, pp. 1165-1168, 1978.
- [38] S. Cai, M.R. Daymond and R.A. Holt, "Deformation of high  $\beta$ -phase fraction Zr–Nb alloys at room temperature," *Acta Mater.*, vol. 60, pp. 3354-3369, 2012.
- [39] Y. H. Joeng, K. O. Lee and H. G. Kim, "Correlation between the tensile strength and corrosion behaviour of heat treated Zr-1.0Nb," *J. Nucl. Mater.*, vol. 40, pp. 505-508, 2008.
- [40] Z. W. Wang, Y. Li, Z. Wang, C. Ma, H. X. Yang, H. F. Tian, H. L. Shi, L. Jia, F. Zhang and J. Q. Li, "Effects of ordered structure on superconductivity," *Eur. Phys. Lett.*, vol. 97, pp. 1-2, 2012.

- [41] A.S. Gornakova, B.B. Straumal, A.L. Petelin and A.B. Straumal, "Solid-phase wetting at grain boundaries in the Zr-Nb system," *Bull. Russ. Aca. Sci. Phys.*, vol. 76, pp. 102-105, 2012.
- [42] J. Emsely, in *Nature's building blocks*, Oxford University Press, 2001, pp. 506-511.
- [43] N.M. Beskorovainyi, B.A. Kalin, P.A. Platonov and I.I. Chernov, *Structural materials for nuclear reactors*, Moscow: Energoatomizdat publishers, 1995.
- [44] C. Toffolon-Masclat, P. Barberis, J.C. Brachet, J.P. Mardon and L. Legras, "Study of Nb and Fe precipitation in alpha- phase temperature range (673-832 K) in Zr-Nb-(Fe-Sn) alloys," in *Zirconium in the nuclear industry: Fourteenth international symposium*, ASTM international, 2001.
- [45] F. Onimus and J.L. Bechade, "Radiation effects in zirconium alloys," in *Comprehensive Nuclear Materials*, vol. 4, Elsevier, 2012, pp. 1-31.
- [46] N. Nomura, Y. Tanaka, Suyalatu, R. Kondo, H. Doi, Y. Tsutsumi and T. Hanawa, "Effects of phase constitution of Zr-Nb alloys on their magnetic susceptibilities," *Mater. Trans.*, vol. 50, pp. 2466-2472, 2009.
- [47] Y. Du, J. Wang, Y. F. Ouyang, L. J. Zhang, Z. H. Yuan, S. H. Liu and P. Nash, "An approach to determine enthalpies of formation for ternary compounds," *J. Min. Metall.*, vol. 46, pp. 1-9, 2010.
- [48] A. Guillermet, "Thermodynamic analysis of the stable phases in the ZrNb system and calculation of the phase diagram," *Z. Metallkd*, vol. 82, pp. 478-

487, 1991.

- [49] H. Okamoto, "Nb-Zr (niobium zirconium)," *J. Phase Equilib.*, vol. 13, pp. 577-577, 1992.
- [50] "Study on microstructure and wear resistance of Zr-17Nb alloy irradiated by high current pulsed electron beam," *Rev. Mater. Sci.*, vol. 59, pp. 514-522, 2020.
- [51] Y. Zhao, H. Li and Y. Huang, "The structure, mechanical, electronic and thermodynamic properties of bcc ZrNb alloy - A first principle study.," *J. Alloys Compd*, vol. 1, pp. 1-9, 2020.
- [52] M. Devillers, M. Sirch, S. Bredendiek-Kamper and R.D. Penzhorn, "Characterisation of the Zr-Co hydrogen system in view of its use for tritium storage," *Chem. Mater.*, vol. 2, pp. 255-262, 1990.
- [53] Y. Naik, C.A. Rama Rao and V. Venngopal, "Zirconium-cobalt intermetallic compound for storage and hydrogen recovery," *Intermetal.*, vol. 9, pp. 309-312, 2001.
- [54] R. Kuentzler, A. Amamou, R. Clad and P. Turek, "Electronic structure, superconductivity and magnetism in the Zr-Co system," *J. Phys. F: Met. Phys.*, vol. 17, pp. 459-474, 1987.
- [55] W.J. Gong, H.L. Zhang, C.F. Wu, H. Tian and X.T. Wang, "The role of alloying elements in the initiation of nanoscale porosity in oxide films formed on Zirconium alloys," *Corros. Sci.*, vol. 77, pp. 391-396, 2013.

- [56] W. Lian-Feng, B. Chen, W. Shi-Zhong and Z. Meng-bin, "Low cycle fatigue properties of hydrogenated welding sheets of Zr-Sn-Nb alloy using funnel shaped flat specimens," *Nucl. Eng. Technol*, vol. 52, pp. 1724-1731, 2020.
- [57] C. Toffolon-Masclat, J.C. Brackert, C. Servant, J.M. Joubert, P. Barberis, N. Dupin and P. Zeller, "Contribution of thermodynamic calculations to metallurgical studies of multi component Zirconium based alloys," *J. ASTM Inst.*, vol. 5, pp. 1-21, 2008.
- [58] Z. Han, X. Liu, S. Zhao, Y. Shao, J. Li and K. Yao, "Microstructure, phase stability and mechanical properties of Nb-Ni-Ti-Co-Zr and Nb-Ni-Ti-Co-Zr-Hf high entropy alloys," *Prog. Nat. Sci.*, vol. 25, pp. 365-369, 2015.
- [59] S. J. Clark, M. D. Segall, C. J. Pickard, P. J. Hasnip, M. I. J. Probert, K. Refson and M. C. Payne, "First principles methods using CASTEP," *Z. Kristallogr.*, vol. 220, p. 567–570, 2005.
- [60] D. Abou-Ras, T. Kirchartz and U. Rau, *Advanced characterization techniques for thin film solar cells*, Weinheim: Wiley-VCH, 2016.
- [61] A. E. Mattsson, P. A. Schultz, M. P. Desjarlais, T. R. Mattsson and K. Leung, "Designing a meaningful density functional theory calculations in material science," *Modelling Simul. Mater. Sci. Eng.*, vol. 13, pp. 1-31, 2005.
- [62] J.C. Slater, "A Simplification of the Hartree-Fock method," *Phys. Rev.*, vol. 81, p. 385, 1951.
- [63] V. Monev, "Density Functional Theory Calculations of Molecular



- Hyperpolarizabilities," *Molecular Eng.*, vol. 8, pp. 217-234, 1998.
- [64] P. Hohenberg and W. Kohn, "Inhomogeneous electron gas," *Phys. Rev. B*, vol. 136, pp. 867-871, 1964.
- [65] W. Kohn and L.J. Sham, "Self-consistent equations including exchange and correlation effects," *Phys. Rev. A*, vol. 140, pp. 1133-1138, 1965.
- [66] J.P. Perdew, A. Ruzsinszky, J. Tao, V.N. Staroverov and G.E. Scuseria et al., "Prescription for the design and selection of density functional approximations: More constraint satisfaction with fewer fits," *J. Chem. Phys.*, vol. 123, pp. 1-8 (062201), 2005.
- [67] L.H. Thomas 542 (1926), "Theory with correlation correction," *Proc. Camb. Phil. Soc.*, vol. 23, pp. 542-544, 1926.
- [68] E. Fermi, "Theory for atomic systems," *Z. Phys.*, vol. 48, pp. 73-79, 1928.
- [69] D.R. Hartree, "Advances in quantum chemistry," *Proc. Camb. Phil. Soc.*, vol. 24, pp. 89-111, 1928.
- [70] V. Fock, "Theory of condensed matter," *Z. Phys.*, vol. 62, pp. 795-796, 1930.
- [71] J.C. Slater, "Quantum theory of molecules and solids," in *The self-consistent field for molecules and solids*, McGraw-Hill, Francis group, 1974, pp. 133-134.
- [72] J.C. Slater, "A simplification of the Hatree-Fock method," *Phys. Rev.*, vol. 81, pp. 385-390, 1951.
- [73] L. Hedin and B.I. Lundqvist,, "Explicit local exchange-correlation potentials," *J.*

- Phys.*, vol. 4, pp. 2064-2082, 1971.
- [74] L. Hedin and S. Lundqvist, "Explicit local exchange-correlation potentials," *J. Phys.*, vol. 24, pp. 495-502, 1972.
- [75] D.M. Ceperley and B.J. Alder, "Calculated electron affinities of the elements," *Phys. Rev. Lett.*, vol. 45, pp. 566-569, 1980.
- [76] J.P. Perdew, "Generalized gradient approximation made simple," *Phys. Rev.*, vol. 33, pp. 8822-8824, 1986.
- [77] A. D. Becke, "Generalized gradient approximation made simple," *Phys. Rev.*, vol. 38, pp. 3098-3100, 1988.
- [78] J.P. Perdew and Y. Wang, "Generalized gradient approximation made simple," *Phys. Rev.*, vol. 45, pp. 13244-13249, 1992.
- [79] J.P. Perdew, K. Burke and M. Ernzerhof, "Generalized gradient approximation made simple," *Phys. Rev. Lett.*, vol. 77, pp. 3865-3868, 1996.
- [80] J. Andzelm and E. Wimmer, "Advances in density functional theory," *J. Chem. Phys.*, vol. 33, pp. 186-188, 1992.
- [81] G.S. Louie, S. Froyen and M.L. Cohen, "Nonlinear ionic pseudopotentials in spin-density-functional calculations," *Phys. Rev. B*, vol. 26, pp. 1738-1742, 1982.
- [82] L.C. Reis, J.M. Pacheco and J.L. José, "First-principles norm-conserving pseudopotential with explicit incorporation of semicore states," *Phys. Rev. B*,

vol. 68, p. 155111, 2003.

- [83] J. C. Philips , “Energy band interpolation scheme based on a pseudopotential,” *Phys. Rev.* , vol. 112, pp. 685-689, 1958.
- [84] M. L. Cohen and V. Heine, “The fitting of pseudopotentials to experimental data and their subsequent application,” *Solid State Phys.*, vol. 24, pp. 37-248, 1970.
- [85] M.T. Yin and M.L. Cohen, “Theory of ab initio pseudopotential calculations,” *Phys. Rev. B*, vol. 8, pp. 5747-5753, 1973.
- [86] D. J. Chadi and M. L. Cohen, “Special points in the brillouin zone intergrations,” *Phys. Rev. B*, vol. 13, pp. 5188-5192, 1976.
- [87] J. C. Phillips, “Energy-band interpolation scheme based on pseudopotential.,” *Phys. Rev.*, vol. 112, pp. 686-695, 1958.
- [88] P. Kratzer and J. Neugebauer, “The basis of electronic structure theory for periodic systems,” *Front. Chem*, vol. 7, pp. 80-106, 2019.
- [89] P.E. Blochl, “Projector augmented-wave method,” *Phys. Rev. B*, vol. 50, pp. 17953-17979, 1996.
- [90] D. L. Chadi and M. L. Cohen, “Special points in the brillouin zone,” *Phys. Rev. B* , vol. 8, pp. 5747-5743, 1973.
- [91] H.J. Monkhorst and J.D. Pack, “Special points for Brillouin zone interactions,” *Phys. Rev. B*, vol. 13, pp. 5188-5192, 1976.
- [92] J. Goldak, L.T. Lloyd and C.S. Barret, “lattice parameters, thermal expansions

- and Gruneisen coefficient of Zirconium,” *Phys. Rev.*, vol. 144, pp. 478-484, 1966.
- [93] L. Nordheim, “To the electron theory of metals,” *Ann. Phys.*, vol. 401, pp. 607-640, 1931.
- [94] L. Bellaiche and D. Vanderbilt, “Ab-initio calculation of complex processes in materials,” *Phys. Rev. B*, vol. 61, pp. 7877-7882, 2000.
- [95] S. de Gironcoli, P. Giannozzi and S. Baroni, “Structure and thermodynamics of  $\text{Si}_x\text{Ge}_{1-x}$  alloys from ab initio monte carlo simulations,” *Phys. Rev. Lett.*, vol. 66, pp. 2116-2119, 1991.
- [96] N. Marzari, S. de Gironcoli and S. Baroni, “Structure and phase stability of  $\text{Ga}_x\text{In}_{1-x}\text{P}$  solid solutions from computational alchemy,” *Phys. Rev. Lett.*, vol. 72, pp. 4001-4004, 1994.
- [97] N.J. Ramer and A.M. Rappe, “Application of a new virtual crystal approach for the study of disordered perovskites,” *J. Phys. Chem. Solids*, vol. 61, pp. 315-320, 2000.
- [98] H. Yoshida, “Construction of higher order symplectic intergrators,” *Phys. Lett. A*, vol. 150, p. 262, 1990.
- [99] M. Suzuki, “J. Math. Phys.,” *General theory of fractal path intergrals with applications to many-body theories and statistical physics*, vol. 32, p. 400, 1991.
- [100] B. Dely, E. A. Freeman, E. Baerends And D. Post, “Binding energy and

- electronic structure of small copper particles," *Phys. Rev. B*, vol. 27, pp. 2132-2144, 1983.
- [101] D.Y. Lin, S.S. Wang, D.L. Peng M. Li and X.D. Hui, "An n-body potential for Zr-Nb system based on the embedded-atom method," *J. Phys.: Cond. Matt.*, vol. 25, pp. 1-14, 2013.
- [102] G Gresse and J Furthmuller, "Efficiency of ab-initio total energy calculations for metals and semiconductors using a plane-wave basis set," *Comp. Mat. Sci.*, vol. 6, pp. 15-50, 1996.
- [103] J Tian, Y. Zhao, H. Hou and B. Wang, "The effect of alloying elements on the structural stability, mechanical properties, and Debye temperature of Al<sub>3</sub>Li: A First-Principles study," *Mater. Bas.*, vol. 11, pp. 1465-1471, 2018.
- [104] M. M. Malebati, P. E. Ngoepe and H.R. Chauke, "Thermodynamic and mechanical stability studies of ZrNb(Co) alloys," *SAIMM*, vol. 5, pp. 65-69, 2015.
- [105] M.J. Mehl, B.M. Klein and D.A. Papaconstantopoulos, "Structural properties of ordered high temperature intermetallic alloys from first principles total energy calculations," *Phys. Rev. B*, vol. 41, pp. 10311-10323, 1990.
- [106] A. Zaoui, S. Kacimi, A. Boukortt and B. Bouhafs, "Ab initio studies of structural, elastic and electronic properties of Zr<sub>x</sub>Nb<sub>1-x</sub>C," *Physica B*, vol. 405, pp. 153-157, 2010.
- [107] M. J. Mehl, B. M. Klein and D. A. Papaconstantopoulos, "First principles

- calculations of elastic properties of materials," *Inter. Comp.*, vol. 4, pp. 1-26, 1993.
- [108] S.F. Pugh, "Relations between the elastic moduli and the plastic properties of polycrystalline pure metals," in *Philosophical Magazine Series 7: Series 7*, Taylor and Francis, 1954, pp. 823-843.
- [109] M. J. Mehl and B. M. Klein, "Basics of Thermodynamics and Phase Transitions in Complex Intermetallics," *Inter. Comp.*, vol. 1, pp. 1-219, 1994.
- [110] W. Voight, *Lehrbuch der Kristallphysik*, Leipzig: Teubner, 1928.
- [111] A. Reuss, "A calculation of the bulk modulus of polycrystalline materials," *Z. Angew. Mech.*, vol. 9, pp. 49-58, 1929.
- [112] R. Hill, "The elastic behaviour of a crystalline aggregate," *Proc. Phys. Soc.*, vol. 65, pp. 349-354, 1952.
- [113] W. A. Harrison, in *Electronic structure and properties of solids*, New York, Dover publications, 1989, pp. 103-105.
- [114] R. Mahlangu, M.J. Phasha, H.R. Chauke and P.E. Ngoepe, "Structural, elastic and electronic properties of equiatomic PtTi as a potential high-temperature shape memory alloy," *Inter. Comp.*, vol. 33, pp. 27-32, 2013.
- [115] R. Mahlangu, "First principle study of Ti-Al and Pt-Ti alloys," University of Limpopo (Thesis), 2009.
- [116] K. Gunawardana, S.R. Wilson, M.I. Mendeleev and X. Song, "Theoretical

- calculation of the melting curve of Cu-Zr binary alloys,” *Phys. Rev. E*, vol. 90, pp. 1539-3755, 2014.
- [117] A. A. Ridha, in *Binding energy and nuclear models*, Baghdad, Al Mustansiriyah University, 2016, pp. 12-40.
- [118] J. Behler and B. Delly, “A standard tool for Density Functional calculations,” FHI workshop, 2003.
- [119] M.A. Hadi, M.T. Nasir, M. Roknuzzaman, M.A. Rayhon, S.H. Naqib and A.K.M.A. Islam, “First principles prediction of mechanical and bonding characteristics of new T2 superconductor Ta<sub>5</sub>GeB<sub>2</sub>,” *Physica Status Solidi*, vol. 253, pp. 2019-2020, 2016.
- [120] G. Vaitheeswaran, V. Kanchana, R. S. Kumar, A. L. Cornelius, M. F. Nicol, A. Svane, A. Delin and B. Johansson, “High pressure structural, elastic and electronic properties of the scintillator host material, KMgF<sub>3</sub>,” *Condens. Matter*, vol. 2, pp. 6-8, 2018.
- [121] J.Y. Rho, “Young's modulus of trabecular and cortical bone material: ultrasonic and microtensile measurements,” *J. Biomech.*, vol. 26, pp. 111-119, 1993.
- [122] G.N. Greaves, A.L. Greer, R.S. Lakes and T. Rouxel, “Poisson's ratio and modern materials,” *Nat. Mater.*, vol. 10, pp. 823-837, 2011.
- [123] Z. N. Yang, F. C. Zhang, L. Qu, Z. G. Yan, Y. Y. Xiao, R. P. Liu, X. Y. Zhang, “Formation of duplex microstructure in Zr-2.3Nb alloy and its plastic behaviour at various strain rates,” *Int. J. Plast.*, vol. 54, pp. 163-177, 2014.

- [124] R. B. Adamson and P. Rudling, "Properties of zirconium alloys and their applications in light water reactors (LWRs)," in *Materials ageing and degradation in light water reactors*, New Delhi, woodhead publishing, 2013, pp. 151-248.
- [125] O. Murańskya, M.R. Daymond<sup>b</sup>, D. Bhattacharyya<sup>a</sup>, O. Zanellatoc, S.C. Vogeld and L. Edwards, "Load partitioning and evidence of deformation twinning in dual-phase fine-grained Zr–2.5%Nb alloy," *Mater. Sci. Eng.*, vol. 564, pp. 548-558, 2013.
- [126] M. torrent, F. Jollet, F. Bottin, G. Zerah and Xavier Gonze, "Implementation of the projector augmented-wave method in the ABINIT code: Application to the study of iron under pressure," *Comp. Mater. Sci.*, vol. 42, pp. 337-351, 2008.
- [127] P.E. Blochl, O. Jepsen and O.K. Anderson, "Improved tetrahedron methods for Brillouin zone integration," *Phys. Rev. B*, vol. 49, pp. 16223-16233, 1994.
- [128] W. W. Xu, S. L. Shang, B. C. Zhou, Y. Wang, L. J. Chen, C. P. Wang, X. J. Liu and Z. K. Liu, "A first-principles study of the diffusion coefficients of alloying elements in dilute alpha-Ti alloys," *Phys. Chem. Chem. Phys.*, vol. 18, p. 1687, 2016.



## **APPENDIX A**

### **Papers published.**

1. M.M. Malebati, P.E. Ngoepe and H.R. Chauke, "Thermodynamic and mechanical stability studies of ZrNb (Co) alloys" in Proceedings of The South African Institute of Mining and Metallurgy, Advanced Metals Initiative Nuclear Materials Development Network Conference, 2015, pages 65-70.
2. M.M. Malebati, P.E. Ngoepe and H.R. Chauke, "The effect of Co and Sn on Zr-Nb alloys for high-temperature application" MRS advances. 2018 Materials Research Society. DOI: 10.1557/adv.2018.500
3. M.M. Malebati, P.E. Ngoepe and H.R. Chauke, "Structural and thermodynamic properties of Zr-Nb-Co compound" Proceedings of the South African Institute of Physics. 03-07 July 2017.

### **Conferences Participated**

1. M.M. Malebati, P.E. Ngoepe and H.R. Chauke, "Computational modeling studies of  $Ti_{50}Pt_{50-x}Nb_x$  alloys" (Poster Presentation) in The 59<sup>th</sup> annual conference of the South African Institute of Physics hosted by University of Johannesburg. Johannesburg, July 2014
2. M.M. Malebati, P.E. Ngoepe and H.R. Chauke, "Thermodynamic and mechanical stability studies of Zr-Nb (Co) alloys" (Oral Presentation) in the 60<sup>th</sup> Annual Conference of the South African Institute of physics hosted by NMMU and Rhodes University. PE July 2015.

3. M.M. Malebati, P.E. Ngoepe and H.R. Chauke, “ Effects of Co on ZrNb alloy using Density Functional Theory and Virtual Crystal Approximation” (Poster Presentation) in the 61<sup>st</sup> annual conference of the South African Institute of Physics jointly hosted by the Departments of Astronomy and Physics University of Cape Town. July 2016
4. M.M. Malebati, P.E. Ngoepe and H.R. Chauke, “Structural and Thermodynamic properties of Zr-Nb-Co compound.” (Poster Presentation) in the 62<sup>nd</sup> annual conference of the South African Institute of Physics, Stellenbosch University, July 2017.
5. M. M. Malebati, P. E. Ngoepe and H. R. Chauke, “First principle study on the thermodynamic and mechanical stability of Zr-Nb(Co) alloys for nuclear reactor applications” in the 6th Annual Postgraduates Research Day Hosted by the Faculty of Science and Agriculture (FSA) University of Limpopo, October 2015.
6. M. M. Malebati, P. E. Ngoepe and H. R. Chauke, “Effect of cobalt addition on the stability of  $Zr_{97}Nb_{3-x}Co_x$  systems” in the 7th Annual Postgraduates Research Day Hosted by the Faculty of Science and Agriculture (FSA) University of Limpopo. October 2016.
7. M.M. Malebati, P. E. Ngoepe and H.R. Chauke, “Ternary alloying additions on  $Zr_{78}Nb_{22-x}M_x$  (M: Sn, Co and Fe) systems for high temperature cladding purposes” CHPC national conference, December 2019.